5-2015

Aerial Thermography in Archaeological Prospection: Applications & Processing

Autumn Chrysantha Cool
University of Arkansas, Fayetteville

Citation

Cool, A. C. (2015). Aerial Thermography in Archaeological Prospection: Applications & Processing. *Graduate Theses and Dissertations* Retrieved from https://scholarworks.uark.edu/etd/1157

Aerial Thermography in Archaeological Prospection:
Applications & Processing

Aerial Thermography in Archaeological Prospection:
Applications & Processing

A thesis submitted in partial fulfillment
of the requirements for the degree of
Master of Arts in Anthropology

by

Autumn Chrysantha Cool
Lewis & Clark College
Bachelor of Arts in Anthropology and Mathematics, 2007

May 2015
University of Arkansas

This thesis is approved for recommendation to the Graduate Council.

Dr. Jesse Casana
Thesis Director

Dr. Kenneth Kvamme
Committee Member

Dr. Jackson Cothren
Committee Member

Abstract

Aerial thermography is one of the least utilized archaeological prospection methods, yet it has great potential for detecting anthropogenic anomalies. Thermal infrared radiation is absorbed and reemitted at varying rates by all objects on and within the ground depending upon their density, composition, and moisture content. If an area containing archaeological features is recorded at the moment when their thermal signatures most strongly contrast with that of the surrounding matrix, they can be visually identified in thermal images.

Research conducted in the 1960s and 1970s established a few basic rules for conducting thermal survey, but the expense associated with the method deterred most archaeologists from using this technology. Subsequent research was infrequent and almost exclusively appeared in the form of case studies. However, as the current proliferation of unmanned aerial vehicles (UAVs) and compact thermal cameras draws renewed attention to aerial thermography as an attractive and exciting form of survey, it is appropriate and necessary to reevaluate our approach.

In this thesis I have taken a two-pronged approach. First, I built upon the groundwork of earlier researchers and created an experiment to explore the impact that different environmental and climatic conditions have on the success or failure of thermal imaging. I constructed a test site designed to mimic a range of archaeological features and imaged it under a variety of conditions to compare and contrast the results. Second, I explored a new method for processing thermal data that I hope will lead to a means of reducing noise and increasing the clarity of thermal images. This step was done as part of a case study so that the effectiveness of the processing method could be evaluated by comparison with the results of other geophysical surveys.

Acknowledgements

I would like to express my gratitude to my committee, especially my advisor Dr. Jesse Casana, for their support and assistance throughout this project. I also owe special thanks to Stephanie Sullivan and Adam Wiewel, my indispensable teammates during the Collins site research, and to Vaughn Skinner and his colleagues at the Arkansas Agricultural Research and Extension Center for their assistance setting up the experimental plot. Finally, I am very grateful for the support and labor put in by Devin Pettigrew and my laboratory students during construction of the experimental plot and its features.

Table of Contents

1. Introduction

Remote sensing technologies are increasingly ubiquitous in modern archaeological prospection. Researchers rely heavily upon these technologies in many field projects, employing them with a frequency that may even surpass the employment of traditional methods such as pedestrian survey and excavation (e.g. Dockrill et al. 1995; Hodder 2006; Kvamme 2008a). Entire journals dedicated to the exploration and application of these methods include *Archaeological Prospection* and *Archaeometry*.

A primary attraction for many archaeologists is the non-destructive efficiency of remote sensing-based approaches to archaeological investigations (Kvamme 2008b: 66; Neubauer 2004: 160). In projects with limited time, budgets, and labor, remote sensing tools operated by just one or two individuals can gather huge quantities of data over relatively little time. Archaeologists can then analyze and apply this information in a variety of ways, from situating an archaeological site within its larger regional context, to deriving plan-view maps of entire buildings and other major features, to directing attention to specific areas of a site that may be the most promising focal points for further intensive study and excavation.

Remote sensing technologies not only save time, but extend and improve our perception beyond the natural human senses (Buck, Sabol, and Gillespie 2003: 973). They enable archaeologists to discover subtle anthropogenic anomalies by detecting physical characteristics normally imperceptible to humans, such as changes in magnetism (e.g. Gaffney and Gater 2010: 25–54; Kvamme 2003). This reduces error by minimizing human sensory bias.

The variety of remote sensing technologies is as extensive as they are common. Archaeologists routinely employ a combination of tools including aerial and satellite imagery, ground-based geophysical survey, pedestrian survey, and excavation in their research (e.g.

Kvamme 2006). New technologies are constantly being tested, adapted, and added to the toolbox. Aerial thermography is among the most recent innovations.

Thermography, or thermal imaging, is the recording and measurement of heat radiation with specially-designed cameras. Until very recently this technology has seen relatively little use in archaeological contexts. While satellites have been collecting thermal data for several decades, their resolution is extremely low. Even Landsat 8, launched in February of 2013, only has a thermal infrared ground resolution of 100 m, which is entirely unsuitable to most archaeological investigations (Landsat: A Global Land-Imaging Mission 2013). For many years the only alternative was the scanning radiometer. They were expensive, airplane mounted systems which required intensive image correction, georectification, and data coding and processing (e.g. Scollar et al. 1990: 611–618; Périsset and Tabbagh 1981: 170). In addition, many archaeologists were put off by the added layer of difficulty and expense of hiring a pilot and an airplane to conduct aerial survey. A few curious researchers tested thermal applications in the 1970s and 1980s, but in the end most chose not to invest their limited time and money in this untested technology.

Today high-quality, compact thermal cameras are at last reasonably priced. Combined with the current proliferation of Unmanned Aerial Vehicles (UAVs), the deployment of aerial thermography has become a feasible prospecting method for archaeologists. However, the thermal imaging strategies currently being employed by archaeologists are largely based on a limited amount of dated research. While there have been modern site-based case studies (see Casana et al. 2014; Poirier, Hautefeuille, and Calastrenc 2013; Kvamme 2006, 2008), few systematic experiments have been conducted to study the general efficacy of aerial thermography in archaeological contexts (one exception is Buck, Sabol, and Gillespie 2003). Archaeologists are without detailed guidelines describing when, where, and how aerial thermography can and should be applied to ensure the highest probability of collecting productive data.

With this thesis I aim to verify previous assumptions as well as add to our existing knowledge regarding the appropriate application of thermal imaging in archaeological prospecting. I have taken a two-pronged approach: a controlled, experimental study and a site-based case study.

For the experimental portion of this research I constructed a test plot designed to mimic a variety of subsurface archaeological features. I buried a series of simple features common to many archaeological sites beneath two distinct types of soil. I then collected thermal images of this test plot under a variety of environmental conditions to observe at what times and under what climatic conditions the various features are the most identifiable. The experimental site is described in Chapter 4.

The site-based case study was primarily used to test an experimental thermal data processing method designed to reduce vegetation noise in thermal imagery. Following methods for data collection and image processing described by Casana et. al (2014), I collected thermal, near-infrared, and color images of a known archaeological site and combined them in a Geographic Information Systems (GIS) program. I then compared the raw and processed data with the results of previous geophysical surveys conducted at the same site to identify potential archaeological features and assess the performance of the processing technique. This portion of my research is described in Chapter 5.

2. Background

2.1. The Science of Aerial Thermography

The earliest form of remote sensing used in archaeology was aerial imaging (Scollar et al. 1990: 26). The types of aerial data collected today range from black and white photographs to multispectral images that record wavelengths well outside of the visible light spectrum (Leisz 2013:14). Aerial imaging allows quick coverage of extensive areas which would be impractical to thoroughly traverse on foot. It also offers the archaeological surveyor easy access to areas where hostile terrain would make pedestrian survey challenging if not impossible. Furthermore, aerial imaging can be used to detect surface and subterranean features not immediately visible from a ground-level perspective.

O.G.S. Crawford, a pioneer of the method, used aerial photography to discover and map the remains of road and field systems in Wessex and Sussex, England that dated to before the Roman conquest (Crawford 1923: 342). In addition to those features that have left obvious remains on the surface, he noted that buried features may leave discolorations known as soil marks in the topsoil. To the observer on the ground these appear as just a random, “confused tangle,” but when viewed from above “an orderly system is visible” (Crawford 1923: 343). Roads, walls, and other features may be revealed in soil marks as clearly as if they were drawn on a blueprint. Since this early work, aerial imaging has remained among the most commonly employed forms of remote sensing used by archaeologists (see Leisz 2013).

While thermography may sound like an exclusively modern invention, archaeologists have been indirectly taking advantage of thermal data for the last century. Just as discolorations in the soil may indicate the presence of subterranean features, patterns seen in melting frost and snow may also signal the location of an archaeological site (Scollar et al. 1990: 48–49, 591;

Stanjek and Faßbinder 1995: 91). These frost or snow marks are created by the uneven melting of frost and snow over the top of buried archaeological features which retain and reradiate heat at varying rates depending on their physical composition. Like soil marks, they have been known to reveal a vivid birds-eye-view map of the archaeology which could not normally be seen by a person standing on the ground's surface, but which immediately become clear when recorded in simple aerial photographs (e.g. Braasch 1983).

The analysis of frost and snow marks has several major disadvantages. Their appearance relies on precise conditions of climate, weather, and lighting (Stanjek and Faßbinder 1995: 99). They are difficult to predict, never guaranteed, and their transient nature makes thoroughly recording such features challenging on the occasions when they do appear. Thankfully, the physical phenomenon that creates these frost and snow marks, the unequal heating and cooling rates of different materials in the ground, can now be measured directly via thermal cameras.

Thermal cameras record heat, or thermal infrared radiation (TIR). Thermal radiation is a type of electromagnetic wave located within the infrared range of the electromagnetic spectrum (Figure 1). While the wavelengths of visible light range from 0.4 – 0.78 μm, infrared radiation is longer, ranging from 0.78 – 1000 μm (Mehta 2011). The infrared spectrum can be further subdivided into near infrared (NIR 0.78 – 2.5 μm), mid infrared (MIR 2.5 – 10 μm), and far infrared (FIR 10 – 1000 μm) (Mehta 2011). What is commonly referred to as thermal radiation overlaps both mid and far infrared, occupying the range of 8 – 15 μm wavelengths (Science Mission Directorate 2010). This is the range in which ground temperature, in the form of radiant heat, can be measured without interference from the ambient air temperature (Scollar et al. 1990: 610; Science Mission Directorate 2010).

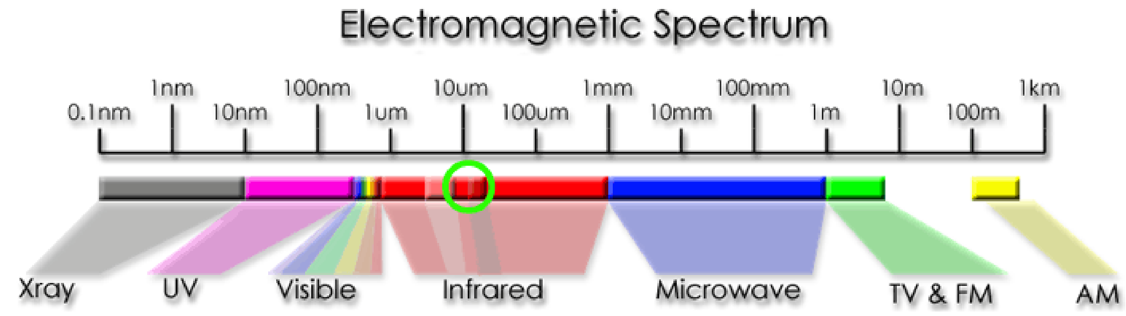

Figure 1: Thermal infrared radiation, circled in green (redIRIS Infrared Inspections 2009)

Surface temperature is not directly equivalent to the amount of thermal infrared radiation emitted from the sun. “Soil temperature depends on solar radiation and exchanges with the atmosphere” (Périsset and Tabbagh 1981: 169). Many electromagnetic waves are reflected back into space by gasses in the Earth’s atmosphere. The radiation that successfully passes through the atmosphere is then absorbed and reflected at different rates by the materials located on and near the Earth’s surface (Abrams and Comer 2013: 59, 61). Finally, absorbed heat is re-emitted at varying rates depending on the physical and chemical characteristics of the material in which it has been stored (Abrams and Comer 2013: 62).

Archaeological sites consist of a mixture of several materials. They may contain stone walls, packed clay floors, organically-enriched middens, or areas where topsoil was removed or added during the construction of earthworks. If these materials’ thermal absorption and emission properties are measurably distinct from the soil matrix in which they are embedded, the resulting variations of thermal radiation across a site may trace the locations of archaeological features (see Kvamme 2008b: 66). When recorded by a thermal camera, these patterns of warm and cool areas can be just as revealing as Crawford’s soil marks.

There are several related characteristics that affect the thermal behavior of materials. Thermal conductivity, heat capacity, thermal inertia, and diffusivity are primary factors. The relationships among these variables and how they may be manifested in archaeological contexts have been researched and described in-depth by Périsset and Tabbagh (1981), Scollar et al. (1990), and Stanjek and Faßbinder (1995), among others. A clear understanding of these factors is helpful in predicting when thermal imaging may be most productive, as well as in interpreting results.

Périsset and Tabbagh conducted a series of controlled experiments from the early 1970s through the 1980s to quantify the thermal behavior of archaeological features (e.g. Périsset 1980; Périsset and Tabbagh 1981; Tabbagh 1977; Tabbagh 1979). They are credited with laying out the initial ground rules for the appropriate application of aerial thermography which archaeologists still refer to today. Most of their work is only available in French at the present time; however, a few summaries of their research have been published in English, including *Interpretation of Thermal Prospection on Bare Soils* (1981). It is a thorough treatise on soil thermodynamics which provides detailed mathematical formulas for several physical properties as well as descriptions of how these abstract equations can be applied to archaeological field research. They also share the results of several controlled experiments and case studies which they used to confirm and improve their analyses, which will be discussed in the following section.

Périsset and Tabbagh (1981) focused on several thermal properties necessary to understand the behavior of heat in soil. The first of these is thermal conductivity, *k*, which describes the ability of a material to transport heat (Périsset and Tabbagh 1981: 170; Stanjek and Faßbinder 1995: 96–97). You are more likely to burn yourself by touching a pan on the stovetop than by hovering your hand directly over the heating element because metals have much higher thermal conductivity than air (Stanjek and Faßbinder 1995: 97). This property is defined as the constant k which relates heat flux $\emptyset$ to temperature gradient $\nabla\theta$ in Fourier’s Law:

$$\emptyset = -k\nabla\theta$$

(Périsset and Tabbagh 1981: 170; Scollar et al. 1990: 594).

The temperature gradient $\nabla\theta$ describes the temperature difference between the material under consideration and its surroundings (Scollar et al. 1990: 594). The heat flux $\emptyset$ is a vector unit which refers to both the rate and direction of travel of heat (Périsset and Tabbagh 1981: 170–171). When the soil is warming, heat is traveling into the ground and we have positive heat flux. When the soil is cooling, heat is traveling into the air and heat flux is negative. The larger the heat flux value (in either the positive or negative direction), the faster the change is occurring.

The second key thermal property is the volumetric specific heat *Cv*, defined by the equation:

$$dQ = Cv\frac{d\theta}{dt}$$

where dQ is the amount of heat stored by unit volume during the time dt (Périsset and Tabbagh 1981: 170). It describes the heat capacity of a material, i.e. the amount of thermal energy that it can retain. This is determined by the physical characteristics of the individual components that make up the material as well as its density (Stanjek and Faßbinder 1995: 97). A useful property which describes the relationship between conductivity and volumetric specific heat is the diffusivity Γ. Diffusivity is the ratio of the conductivity to the volumetric specific heat:

$$\Gamma = \frac{k}{Cv}$$

(Périsset and Tabbagh 1981: 170; Stanjek and Faßbinder 1995: 98). A material with high conductivity and low volumetric specific heat will have high diffusivity, meaning that heat travels through it quickly without being retained. If the material has low conductivity and high volumetric specific heat, it will retain more heat.

The diffusivity Γ is closely related to another frequently referenced property, thermal inertia. Thermal inertia, P, is written:

$$P = \frac{k}{\sqrt{\Gamma}} = \sqrt{kCv}$$

(Périsset and Tabbagh 1981: 170). This describes a material's tendency to resist changes in temperature (Danese et al. 2010: 484). A material with high thermal inertia, like water, is slow to heat up or cool down. Sand, on the other hand, will heat more quickly in the sun and cool just as fast at night due to its lower thermal inertia. Thermal inertia, as shown by the above equation, is another way to describe the complex relationship between thermal conductivity, volumetric specific heat, and diffusivity. It is also an extremely useful value for estimating the potential strength of anomalies in different contexts.

Périsset and Tabbagh (1981) set up several experiments to test how these equations are expressed in the physical world. They designed a software program to analyze the thermal response of two- and three-media models for any combination of flux over time (Périsset and Tabbagh 1981: 169). The two-media model consists of a feature embedded in and covered by a single soil type. The three-media model represents a cylindrical feature embedded in a subsoil layer and covered by a superficial layer (Figure 2).

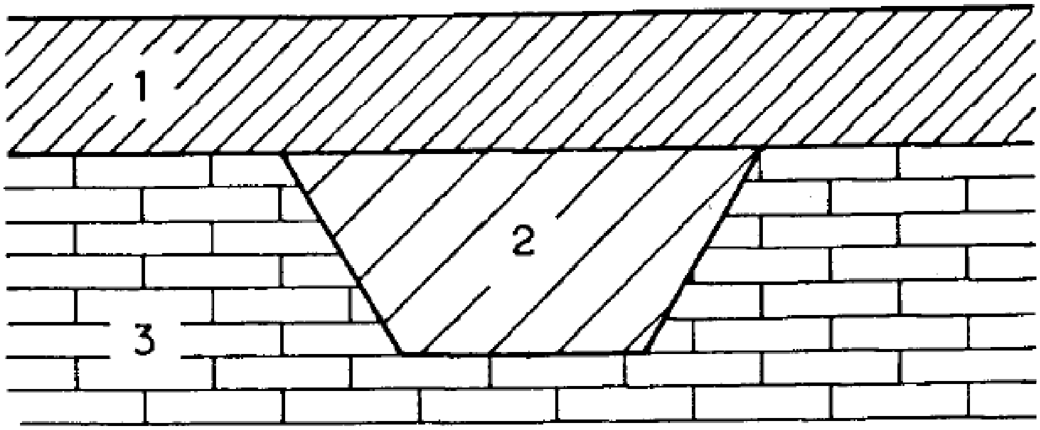

Figure 2: The three-media model. (1) superficial layer (2) feature (3) subsoil (Périsset and Tabbagh 1981: 171).

Périsset and Tabbagh (1981) also constructed several physical models to verify the computer-generated results. They dug a ditch into a limestone subsoil and buried it in topsoil, buried building materials in sand, and buried building materials in gravel, and collected data with an ARIES scanning radiometer (Périsset and Tabbagh 1981: 170–171). From this experimental data they were able to extrapolate rules which describe how the layers of soil overlaying and surrounding an archaeological feature will affect the thermal signature of that feature.

(1) If the superficial layer increases in thickness or conductivity and decreases in diffusivity, the thermal signature of the feature will attenuate.

(2) The superficial layer "has no effect on the sign of the anomaly which only depends on the properties of the features…and of the surrounding soil" (Périsset and Tabbagh 1981: 171).

(3) Features located within low conductivity and low diffusivity subsoil will have a stronger thermal signature on the surface (Périsset and Tabbagh 1981: 171).

The relationship between superficial and subsoil layers can also be expressed through the ratio:

$$\frac{P_2 - P_1}{P_2 + P_1}$$

for a two-layer model where P_1 is the thermal inertia of the superficial layer and P_2 is the thermal inertia of the subsoil (Périsset and Tabbagh 1981: 171). That is, the greater the difference between thermal inertias of the two layers, the more the second layer will affect the thermal signature of the first. If we expand this concept to the three medium model in Figure 2 composed of superficial layer (1), anomaly (2), and subsoil layer (3) (with respective thermal inertias P_1, P_2, and P_3) we can extrapolate a contrast coefficient

$$c = \frac{P_3 - P_2}{P_3 + P_2}$$

(Périsset and Tabbagh 1981: 171). The contrast coefficient c describes the potential strength of the anomaly's thermal signature. It will also have the same sign as c if the flux is positive (soil is warming) or the opposite sign as c if the flux is negative (soil is cooling) (Périsset and Tabbagh 1981: 171). In other words, the potential strength of thermal anomalies depends on the relative thermal inertias of the archaeological feature and the surrounding subsoil in which it is embedded.

Archaeological features are not guaranteed to always display visible thermal signatures simply because they have different thermal properties. While subterranean features will heat and cool at separate rates depending on their thermal inertias, a long stretch of stable weather conditions might allow time for the temperatures of all features and layers to equalize. Thermography must be done while the temperatures of materials are still adjusting and differences are at their maximum.

Périsset and Tabbagh firmly state that diurnal variation of heat flux lacks the penetration depth needed to affect materials below the surface layer (1981: 169). They claim that slow, transient heat flux variation determines when an anthropogenic anomaly will be at its most visible (Périsset and Tabbagh 1981: 169). If, for example, a week of warm weather in which all materials have become thoroughly heated is followed by a week of cold weather, materials with low thermal inertia will cool quickly while those with high thermal inertia will remain relatively warm. The ideal time for thermal imaging is during this period of change, in their experience generally two or three days after a reversal of heat flux, when the temperature difference between features is at its greatest (Périsset and Tabbagh 1981: 172–175).

All of the above analyses are concerned only with the thermal properties of bare soils. As Périsset and Tabbagh point out, “In the presence of vegetation one does not measure the ground surface temperature but that of the plants, which is controlled by plant transpiration” (1981: 169). In other words, plant cover acts as a screen which filters and may even block the thermal response of the soil and features below. Aerial thermography of a vegetated area is only an indirect measurement of soil temperature and will not provide as clear a picture as can be expected of bare soil.

Scollar collaborated with Tabbagh, Herzog, and Hesse to publish the most comprehensive review to date of archaeological thermography as the last chapter in *Archaeological Prospecting and Remote Sensing* (1990: 591–635). Much of the chapter is a clarification of Périsset and Tabbagh’s previous work, but Scollar and the others added in several insightful caveats and clarifications.

Scollar and coauthors began with an overview of thermodynamics as described above. This included perceptive commentary on some of the previous claims regarding diurnal versus transient heat flux. They agreed with Périsset and Tabbagh that slow, transient variations of heat flux are the most productive as they have the best penetration and can expose anomalies linked to archaeological features far below the surface (Scollar et al. 1990: 598). However, they amended Périsset and Tabbagh's previous statement that diurnal heat flux is never strong enough to create useful anomalies. While deeply buried features may not be directly affected by diurnal flux, this flux can still be revealing in the right context "inasmuch as the properties of the surface layer often reflect contrasts which are much deeper" (Scollar et al. 1990: 598). Scollar and coauthors also clarified that yearly seasonal heat flux changes are not useful for archaeological prospection. While seasonal flux does have deep penetration, other surface changes throughout the year caused by vegetation growth, humidity, plowing, and transient heat flux variations create so much noise that anomalies are obscured (Scollar et al. 1990: 597–598). Relying on transient or diurnal heat flux removes many of these complicating variables and provides a clearer picture.

Scollar and coauthors also added in a discussion of microrelief and its expression in thermograms (Scollar et al. 1990: 601). Subterranean features may create minute variations in surface topography, such as tiny dips over filled ditches, which in turn create subtle warm and cool zones depending on their angle of exposure to the sun (Scollar et al. 1990: 601). Easily obscured by temperature noise from shade and shadows, thermal imaging of microrelief is most useful in uniform fields free of vegetation and standing water (Scollar et al. 1990: 601). However, in the right environment surface-level temperatures do have the possibility of providing useful information, as we will see in the next section.

Scollar et al. (1990) next elaborated upon the role of the surface layer. If the surface layer is composed of homogenous material it will uniformly dampen the thermal responses of any subterranean features (Scollar et al. 1990: 605). The amount of dampening depends on the thickness, thermal diffusivity, and thermal conductivity of this surface layer. As Périsset and

Tabbagh previously stated, a thick surface layer or a surface layer with low diffusivity will attenuate the strength of anomalies (1981: 171). Scollar and coauthors pointed out that these characteristics will also delay the appearance of anomalies (1990: 605). On the other hand, increased conductivity attenuates anomalies, but does not affect their timing (Scollar et al. 1990: 605). Thus a thin surface layer or one with high diffusivity is a prime environment for thermal prospecting. Plowed fields are also favorable as the aeration caused by plowing will reduce conductivity, but not affect diffusivity (Scollar et al. 1990: 605).

The surface layer plays a more complex role when it is of heterogeneous composition. This is also the most common situation as surface inhomogeneities are frequently introduced by human agricultural and construction activities, variations in subsurface rock, hydrology, and archaeological material (Scollar et al. 1990: 606). These inclusions can be helpful if they are surface reflections of deep archaeological features, or they may have the opposite effect of overwhelming and masking subsurface features. These shallow inhomogeneities are strongly affected by diurnal variations and most visible in the afternoon, as Scollar and coauthors observed in a survey of several agricultural fields (Scollar et al. 1990: 606). Based on this information and their understanding of transient heat flux variations, Scollar and coauthors established three rules regarding the appropriate time to conduct thermal survey:

> “(1) It is preferable to make measurements without clouds in order to record anomalies due to microrelief…
>
> (2) It is better to take readings during the morning so that the effects of diurnal variation on surface inhomogeneitites do not mask deeper weak anomalies. A flight during the first half of the night might be of interest, but the microrelief will not appear…

(3) It is better to fly after a sufficiently well-marked long variation in transient flux. Calculations of slow variations in transient flux using data from meteorological stations allow verification of whether or not this condition has been fulfilled" (Scollar et al. 1990: 609).

Finally, Scollar et al. ended with a discussion of the role of vegetation in thermal imaging. Dead or inactive plants have poor heat conduction, and the temperature of living plants is regulated by transpiration, not by the surface on which they grow (Périsset and Tabbagh 1981: 169). As previously mentioned, this causes vegetation to act as a screen which obscures the thermal response of any features below. However, thermography of vegetated areas can occasionally provide indirect information about subsurface features (e.g. Tabbagh 1979). Subterranean features may affect the growth of vegetation over them either positively or negatively. For example, stone walls will impede root growth and stunt plants, while a trash pit might be especially nutrient-rich and encourage thick growth (Giardino and Haley 2006: 60). Plant transpiration will change with the health of the plants, which in turn alters plant temperature (Scollar et al. 1990: 631–633).

Few archaeologists have added to the foundations of thermal prospection laid out by Périsset, Tabbagh, and Scollar. Among those who have described additional fundamental rules of thermal behavior are Stanjek and Faßbinder (1995), who provided an excellent overview of the effects of water and soil density. They determined that these characteristics will affect all of the factors previously identified, including volumetric specific heat, diffusivity, and thermal conductivity.

As mentioned previously, volumetric specific heat, or heat capacity, depends on soil composition. The total heat capacity of a soil matrix is simply the sum of the specific heats of all the soil components multiplied by the bulk density (Stanjek and Faßbinder 1995: 97). Therefore, as density increases so does the heat capacity. Density, the ratio of mass to volume, can be also assessed by considering the porosity of soils (Stanjek and Faßbinder 1995: 95). Porous soils are less dense and will generally have lower heat capacity, but this property is easily affected by moisture content. While air has a very little heat capacity, water has twice as much heat capacity as some common minerals such as quartz (Stanjek and Faßbinder 1995:97). Therefore, dry porous soil will contain a fair amount of air and have low heat capacity, while in moist soil water replaces the air between particles and increases heat capacity.

Water content can also improve the thermal conductivity of soils. Even though water does not have as high thermal conductivity as minerals, it is still higher than that of air (Stanjek and Faßbinder 1995: 97). In dry soil, low-conducting air fills the space in between soil particles, thereby limiting heat transfer. When the soil water content increases the air is replaced with water which improves overall conductivity (Stanjek and Faßbinder 1995: 97).

As we can recall from above, thermal diffusivity is the ratio of thermal conductivity to volumetric specific heat ($\Gamma = \frac{k}{Cv}$). Thermal diffusivity will increase quickly with small increases in water content since conductivity increases more quickly than volumetric specific heat as water is added (Stanjek and Faßbinder 1995: 98). However, as the ground becomes saturated the trend will reverse and diffusivity will begin to decrease (Stanjek and Faßbinder 1995: 98). More energy must be used to heat or cool the large amount of water, which has very high thermal inertia.

As areas such as filled ditches or pits tend to retain water, these areas may often create thermal anomalies due to the reduced thermal inertia of the moist soil they contain. Conversely, stone walls contain less water and have higher heat diffusivity and lower heat capacity, which may lead to swift, strong cooling when the air temperature drops (Stanjek and Faßbinder 1995: 100).

2.2. Processing Thermal Data

The results of a thermal survey are visually represented by images referred to as thermograms (Danese et al. 2010: 484). Although most modern thermal cameras record video feeds, it is possible to extract still frames which can be studied individually or mosaicked into a single image for analysis (see Chapters 4 and 5). These thermograms are stored as raster files for data processing. A raster is composed of a grid of cells where each cell represents a geographic location and contains data values for that location (Wheatley and Gillings 2002: 50). In the case of a thermogram, each cell identifies the average temperature in the area represented by that cell. Although any range of colors may be used to represent temperature variations, thermograms are usually grayscale images with black cells assigned to the coldest areas and white cells for the warmest. This is a relative scale that depends on the range of temperatures within each frame; in other words, specific temperatures are not consistently represented by designated gray values.

The quality of a thermogram is determined by several factors, including temperature resolution, spectral resolution, radiometric resolution, and spatial resolution. The temperature resolution depends on the sensitivity of the thermal camera and refers to what temperature increments the camera is capable of detecting. A camera with high temperature resolution can distinguish between very close temperatures. The spectral resolution describes which wavelengths, or range of wavelengths, are recorded (Abrams and Comer 2013: 64). The radiometric resolution refers to the way data is encoded (Abrams and Comer 2013: 65). Most modern thermal data is recorded at 8-bit resolution, meaning that temperatures are distributed across 256 shades of gray. Higher radiometric resolution would allow smaller temperature increments to be recorded across a larger range of gray values, and vice versa. Finally, the spatial resolution refers to the cell size, or the real physical area each cell represents (Abrams and Comer 2013: 64). The higher the resolution, the more information a thermogram can offer; however, too much detail can look noisy and be difficult to interpret.

Once a thermogram is acquired it can be georeferenced to real-world coordinates and then compared with photographs, maps, or other geophysical data to aid in interpretation (e.g. Casana et al. 2014; Kvamme 2008a). This is usually done in a Geographic Information Systems (GIS) program where the data may also be filtered and otherwise manipulated to highlight subtle anomalies (Giardino and Haley 2006: 61–65; see also Wheatley and Gillings 2002). Several archaeologists have had great success discovering archaeological features by combining aerial thermography with other remote sensing or geophysical methods, as will be discussed in the following section.

The research of Bellerby, Noel, and Branigan (1990) provides some interesting ideas for the thermal prospector. They applied a direct-contact method by inserting temperature probes 20 cm into the ground in a grid pattern across archaeological sites. The data was then compiled into a low-resolution thermogram (Bellerby, Noel, and Branigan 1990: 200–201). While this labor-intensive method is unlikely to persist now that aerial thermography has become a more feasible option, the data processing techniques developed by Bellerby and his coauthors may endure.

Bellerby et al. (1990) developed a noteworthy method for filtering out surface-layer noise created by diurnal variation, irregular topography, and soil inhomogeneities. During each survey, they collected multiple temperature readings over time at each point in the survey grid and at a base station. They interpolated a linear function from the first and last base station readings and subtracted it from the total set of base station data. This was then converted into a Fourier series and subtracted from the site grid data (Bellerby, Noel, and Branigan 1990: 197–199). Reducing thermal noise in this manner allowed them to isolate deep features from surface anomalies. Perhaps this technique could be applied to aerial thermography by the addition of a base station when collecting thermal data.

Another interesting analytical technique was presented by Danese et al. (2010). They were not using thermography as a prospecting method, but as a means for detecting decay in historic buildings. However, the data processing approach they describe may be applied to aerial thermography. In addition to the standard practice of visually identifying hot and cool anomalies in individual thermograms, Danese and coauthors suggest searching for temporal anomalies by comparing multiple sequential thermograms. "[P]ixels that follow a similar temperature profile throughout the sequence of thermal images…represent thermal inertia, which measures the tendency of a substance to resist changes in temperature" (Danese et al. 2010:484). In other words, a particular cluster of pixels might not stand out as a noticeably hot or cold anomaly on an individual thermogram, but when studied over time it may be observed that this same cluster of pixels has significantly less or more variance than its neighbors. This would indicate the presence of a material with higher or lower thermal inertia, i.e. more resistant or more susceptible to temperature changes.

3. Previous Archaeological Applications

Among the earliest researchers to employ aerial thermography were geologists. As early as 1934, Van Orstrand employed thermal imaging for geological reconnaissance (Bellerby, Noel, and Branigan 1990: 191). It was not until the 1960s that some geologists realized the potential that thermal imaging holds for archaeologists.

In April 1966, the National Aeronautics and Space Administration conducted a thermal survey of the San Francisco volcanic field northeast of Flagstaff, Arizona. The data was being collected for the Earth Resources Survey Program directed by the U.S. Geological Survey (Berlin et al. 1977: 588). Flying at an altitude of 762 m at 4:00 pm, they collected thermograms with an H.R.B. Singer Co. Reconofax IV scanning radiometer. It recorded wavelengths between 8 and 14 µm at a temperature resolution of 0.25° C (Berlin et al. 1977: 588; Schaber and Gumerman 1969: 712). They also collected simultaneous black and white panchromatic photographs with a ground resolution of 0.3 m (Berlin et al. 1977: 588–589). Upon reviewing their data, the NASA and USGS scientists were surprised to discover three groups of parallel linear anomalies in the thermograms. These anomalies are nearly indistinguishable in the panchromatic photographs despite their fairly high resolution (Schaber and Gumerman 1969: 712).

Gerald Schaber of the USGS and archaeologist George Gumerman performed the initial investigation of these anomalies and published a brief report in 1969. They visited the locations identified in the thermograms and were able to confirm via soil and pollen analysis that the sites were ancient agricultural plots, even though only one of the three anomalies was actually visible on the ground surface (Schaber and Gumerman 1969: 712–713). They also found small habitation sites nearby where they collected diagnostic potsherds that dated to the Sinagua Period between circa AD 1067 to 1200 (Schaber and Gumerman 1969: 712–713).

Schaber and Gumerman (1969) determined that the linear thermal anomalies were the ridges and swales of ancient agricultural fields. Although these features had fairly subtle topography, ranging from 3 to 4 m across and only 5 to 30 cm of vertical relief, they were comprised of two types of soil with distinct thermal characteristics. The ridges were composed of a basaltic ash which has a very low thermal inertia, causing them to warm quickly during the day. The swales, consisting of a buff soil with higher thermal inertia and partially sheltered from the sun by their lower relief, remained cooler (Schaber and Gumerman 1969: 713).

Berlin et al. (1977) conducted further extensive fieldwork at these agricultural plots in the early 1970s. They focused on one field measuring 265 m by 67 m composed of 10 ridge-swale pairs (Berlin et al. 1977: 590). Numerous samples confirmed that the ridges had a 10 to 30cm cap of basaltic ash beneath which lay 5 to 20 cm of brown-buff soil. The swales consisted of this same buff soil with occasional patches of basaltic ash ranging from 2 to 5 cm thick (Berlin et al. 1977: 590). Soil temperature was recorded over a 24-hour period on four of the ridge-swale pairs in early May of 1975. During daylight the ridges measured 1.1° to 6.2° C warmer than the swales, but at night they cooled swiftly until at midnight the ridge temperature actually dropped below that of the swales (Berlin et al. 1977: 590–591). These results are consistent with the ash having lower thermal inertia than the buff soil.

After this initial foray into the use of aerial thermography for archaeological prospection, several archaeologists set out to test the method by more vigorous means. Périsset and Tabbagh, introduced in the previous section, began their work around this time. In addition to their theoretical, physics-heavy research described above, they carried out multiple field-based case studies. For all field research, they used an ARIES radiometer mounted on a small, low-flying aircraft (Périsset and Tabbagh 1981: 170). The spatial resolution of the ARIES varies with altitude and velocity of the aircraft, but can be as high as 1.13 m by 1.17 m (Scollar et al. 1990: 618).

One early case study was thermal survey of the necropolis of La Tombe in Seine et Marne, France (Périsset and Tabbagh 1981: 181). Aerial photography had previously revealed a square enclosure, but no excavation had been conducted. The enclosure appeared as a cold anomaly in the thermogram. As the subsoil was known to be a high thermal inertia clay, this indicated that the enclosure was formed by a ditch containing low thermal inertia fill which had cooled more quickly than its surroundings (Périsset and Tabbagh 1981: 181).

In another case study, Périsset and Tabbagh (1981) surveyed the route of a planned motorway. The flux was not strong enough to induce strong temperature changes at depth, yet several ancient roads and field boundaries were clearly visible among the modern agricultural fields (Périsset and Tabbagh 1981: 184). The visibility of the ancient fields alongside the modern indicates that the ancient features were in the superficial layer (Périsset and Tabbagh 1981: 185).

In their most elaborate case study, Périsset and Tabbagh (1981) surveyed several known Neolithic ditches in Seine et Marne, France. They took samples of soil across the sites and flew aerial survey in three different seasons, attaining the best thermal response in May. They observed that filled pits were visible when dug into compact, high conductivity and high diffusivity gravel, but not in silty ground (Périsset and Tabbagh 1981: 175–176). Since silt and fill material have a low contrast coefficient while gravel and fill together have a high contrast coefficient, this was exactly the response they had anticipated. In contrast, data collected during their December flights had very poor results. At one site thick vegetation obscured all subsurface thermal signatures. A second, unvegetated site had a poor response as well, which was attributed to the late flight time. They were able to see only anomalies in the superficial surface layer that had been exposed by the diurnal heat flux, but no deeper anomalies (Périsset and Tabbagh 1981: 180).

Scollar (1990) presented the results of several other aerial thermography surveys conducted by Périsset and Tabbagh that were not described in their 1981 article. The first was a survey of a Gallo-Roman structure in Leyment, France. No structure was visible in standard or near infrared photographs. However, thermal imagery collected three days after the transient heat flux had reversed from negative to positive clearly exposed structure foundations as a cold anomaly (Scollar et al. 1990: 620, 623). The high thermal inertia of the stone foundations had caused them to warm slowly relative to the surrounding soil matrix.

In another case study in Seine et Marne, microrelief turned out to be a useful phenomenon in a survey of ancient field systems. Soil had piled up at the ends of agricultural fields, perpendicular to the movement of the plow. While too subtle to be visible to the naked eye, the increased thickness of the topsoil in these regions altered the thermal response just enough to be identifiable in the thermograms as linear anomalies marking the location of field boundaries (Scollar et al. 1990: 623–624).

Périsset and Tabbagh also used aerial thermography to pinpoint the location of a deserted village at St Vincent. Survey was conducted after several days of positive heat flux. Multiple large rectilinear anomalies, interpreted as cold stone foundations, were clearly visible. The identification of the site was confirmed by comparison with historic texts (Scollar et al. 1990: 621, 625).

Other field research described by Scollar et al. (1990) took place at a Gallic and Gallo-Roman complex at Maillys, France. There had been no strong variations in transient heat flux leading up to the survey. By the rules established in the previous section, this makes it likely that any observed thermal anomalies would be near-surface and a product of diurnal, not transient, flux. Several cold anomalies indicated a road, Roman camp, and Iron Age rural settlement. Many of these remains had been previously recorded in standard aerial photography, which further supports the analysis that the thermal survey only recorded those near-surface features affected by diurnal heat flux (Scollar et al. 1990: 621–623).

In an aerial survey of a prehistoric complex at Villeneuve La Guyard, a large Gallo-Roman enclosure was visible even through a layer of growing wheat. This was not the result of subterranean thermal anomalies powerful enough to be seen even through vegetation cover. Rather, the composition of subterranean features affected the growth of vegetation over them, which led to altered plant transpiration, which was then recorded by the thermal camera (Scollar et al. 1990: 631–633).

While others were working in France, Bengt Lundén of the University of Stockholm had been researching thermal applications since 1976 (see Lundén 1985). As a professor in the Department of Physical Geography, his initial work focused on using thermography to test subsurface geological conditions and vegetation health. His first attempt at an archaeological application was conducted as part of a rescue archaeology project (Lundén 1985: 162). A new road being constructed in Dalecarlia, Central Sweden, was to cross an area known to contain medieval settlements. Topsoil had already been stripped, so Lundén took advantage of the lack of vegetation noise to collect several unobstructed images. He surveyed the area from a helicopter to acquire color photographs during the day and thermal data shortly before midnight (Lundén 1985: 162). Lundén preferred night thermography as it avoids reflected radiation or an overly warm surface layer that could obscure the thermal signatures of buried features. By collecting thermal data at night, he ensured that only re-radiated heat would be recorded. The timing also guaranteed that diurnal flux would have recently inverted from positive to negative.

It can be inferred from his statement "The day before, like the whole summer, was characterized by dry, warm weather" that he did not take transient flux into account (Lundén 1985: 162).

Lundén's (1985) thermal data was collected by a radiometer capable of recording wavelengths in the range of 8 – 12 µm and sensitive to temperature increments of 0.1° C. This data was recorded to a video cassette which was then reviewed on a monitor. Comparing the thermograms to the color images and maps produced during rescue excavation, he noted a strong correlation between warm areas and archaeological features. Since heat flux was negative at the time of his survey, this indicated that the features had higher thermal inertia than the background environment and were likely stone foundations (Lundén 1985: 163–165).

The earliest example of digital video aerial thermography, the type still employed today, was presented by a team of researchers from Tel Aviv University in Israel. Ben-Dor et al. (1999) mounted a thermal infrared video radiometer on a helicopter and flew it over the Bronze Age settlement Tel Leviah, Israel. They used an Inframetrics Model 760, capable of capturing wavelengths from 3 – 12 µm and temperatures between -20° C and 400° C, accurate to less than 0.1° C at 30° C. They flew several pre-dawn passes at varying altitudes between 1000 and 5000 feet, resulting in spatial resolution ranging from 60 cm to 3 m. By comparing the resultant thermograms with maps of the area, several previously unrecognized linear features were discovered. Ground survey of the anomalies found basalt stones, probably buried walls. Ben-Dor and coauthors emphasize "It is important to mention that these patterns would never have attracted out attention were it not for the additional information provided by the thermal image" (1999: 124).

A few years later, Bryan Haley, Jay Johnson, and Richard Stallings received a grant from the Office of Naval Research to conduct an extensive case study on archaeological thermal prospecting (2002). They begin their report by stating that while Périsset and Tabbagh made an excellent case for the benefits of employing long-term heat flux to detect archaeological features at depth, the calculation of this variation is generally too complicated to be practical in most archaeological research (Haley, Johnson, and Stallings 2002: 3). Transient flux determination requires extended monitoring of soil temperatures, and even when optimal conditions are reached, most archaeologists do not have the ability to visit their sites on a moment's notice. Bearing this in mind, Haley and coauthors focused on the utility of thermal imaging when only diurnal heat flux is considered.

Haley et al. (2002) employed a FLIR Agema 570 for their research at the Mississippian-period Hollywood Mounds Site. The Agema is capable of recording wavelengths from 7.5 to 13 µm at a sensitivity of 0.2° C onto a 320 by 240 pixel video image (Haley, Johnson, and Stallings 2002: 6). The camera was mounted on a helium blimp for the four surveys conducted between July and December (Haley, Johnson, and Stallings 2002: 7). They collected data during several day and night flights. During each survey they tracked relative temperature, humidity, and sunrise/sunset times to study the impact of these factors upon the thermal data.

Haley et al. (2002) georeferenced their thermograms to the Hollywood site grid to allow comparison with the results of previous geophysical surveys and test excavations. Most thermal images collected during daylight hours only recorded reflected surface radiation and did not reveal subsurface features. The exception was a house feature visible as a cool anomaly recorded shortly before midday in July (Haley, Johnson, and Stallings 2002: 13–14). The surrounding soil had warmed just slightly faster than the house materials. Surprisingly, this feature was not visible in any other images, likely because it had nearly identical thermal properties to the surrounding soil matrix. The other house features successfully identified in the thermal imagery were only seen in data collected at night, while known mound remnants were not identifiable (Haley, Johnson, and Stallings 2002: 14).

The most interesting results of Haley, Johnson, and Stallings' study were the impact of local weather patterns on thermal behavior. They were startled to observe that rainfall appeared to have no consistent impact on the quality of thermal data, despite the known effects of water content on thermal inertia (Haley, Johnson, and Stallings 2002: 16). They also noted that the daily temperatures prior to data collection did not seem to have an entirely predictable effect either. They had predicted that a day with a 25° F temperature range would create stronger anomalies than a day with a 20° F range, but the opposite proved true in one survey. They hypothesized that sun intensity and cloud cover, which were not tracked, may have made the difference (Haley, Johnson, and Stallings 2002: 16).

Archaeological aerial thermography has focused almost exclusively on identifying large features, due to the common assumption that that individual artifacts are too small relative to the spatial resolution of most geophysical methods to be detected (Buck, Sabol, and Gillespie 2003: 974). Buck et al. (2003) set out to challenge this belief by testing for the thermal detection threshold of artifact assemblages.

The idea of a detection threshold was originally established by Sabol, Adams, and Smith (1992). They realized that if artifacts within a pixel are sufficiently dense and their spectral response contrasts well with the background environment, they will change the average spectral value of the pixel enough to create a noticeable anomaly (Sabol, Adams, and Smith 1992: 2660). The minimum fraction of the pixel that must be occupied by artifacts varies depending on their physical characteristics and the spectral range being recorded. That fraction is the detection threshold (Buck, Sabol, and Gillespie 2003: 975).

Buck et. al. (2003) collected thermal images of obsidian and ceramic artifact assemblages to calculate the thermal detection thresholds for these materials. They collected data in two field environments, the Mojave Desert and the Pajarito Plateau, and at the Jet Propulsion Laboratory. Field data was collected with a modified FLIR infrared camera. Laboratory data was collected using the Nicolet Spectrometer Model 520, capable of recording wavelengths between 2 and 15 µm. The laboratory data was then resampled to simulate the output of different imaging systems to test the effectiveness of various imaging systems. Detection thresholds varied depending on the background environment and the spectral range of the equipment in use. The obsidian detection threshold in thermal images ranged from 4% to 14% against bare ground and up to nearly 30% as vegetation cover approached 100%. Ceramics were more difficult to identify thermally, having a detection threshold ranging from 12% against a bare mineral surface to 67% against vegetation. Both materials needed to have at least 85% coverage to be detected by visible (VIR) and near-infrared (NIR) imaging sensors in any environment (Buck, Sabol, and Gillespie 2003: 978–984).

Buck and coauthors clearly demonstrated that small artifact assemblages, not just major features, can be detected via remotely-sensed spectral data. This breakthrough should trigger a realization that many archaeologists have been setting our expectations too low, and that it may be time to rethink and re-test the limits of our technology. Furthermore, the knowledge that thermal infrared imaging is far more effective than either VIR or NIR for detecting certain materials is a revelation. These results indicate that thermography has the potential to go beyond replicating other survey results, to uncovering information not obtainable through other methods.

The benefits of conducting aerial thermography in addition to other survey methods are underlined by two case studies conducted by Kenneth Kvamme of the University of Arkansas.

At Army City, Kansas, he employed six different geophysical remote-sensing technologies in order to demonstrate several methods for integrating and analyzing discrete data sets (Kvamme 2006). A second survey at Double Ditch State Historic Site, North Dakota, also combined the results of several prospecting methods (Kvamme 2008a). At both locations thermal images were acquired with a Raytheon Palm-IR250, which records eight-bit data in the 10 µm band and is sensitive to 0.1° C temperature increments. Evening flight data was recorded from the seat of a manned powered parachute flown at an altitude of 250 to 500 m above the sites, resulting in spatial ground resolution up to 10 cm. Still frames were extracted from the thermal video and manually mosaicked, a painstaking process (Kvamme 2006: 60; Kvamme 2008a: 74).

Both of Kvamme's case studies found occasions where features overlooked by other methods were identifiable in the thermal images. At Army City, suspected cellars and streets are visible only in the thermograms (Kvamme 2006: 59). The presence of these features could have been inferred from the foundations and street gutters detected by the ground-penetrating radar and electrical resistivity surveys, but complementary data sets give more confidence to final analysis. At Double Ditch State Historic Site, thermal anomalies successfully matched up with houses, pits, roads, and ditches identified in other surveys (Kvamme 2008a: 74). Thermography was unable to reach the same depths as other technologies, but the anomalies which were visible were strongest in the thermal data sets. In addition, thermography seemed uniquely able to distinguish the lived-in, cultural landscape from the surrounding environment (Kvamme 2008a:74–75). In fact, Kvamme stated that while there is certainly some overlap between the types of features visible in all data sets, "analyses…indicate the thermal data to be most independent of other data sets" (2006: 66). However, while thermal data collection proved efficient and productive, its success was somewhat offset by the increased amount of processing time required to prepare and composite images (Kvamme 2008a: 77).

The recent proliferation of UAVs combined with the emergence of photogrammetric image processing software is proving to be a watershed moment for aerial archaeological investigations. While initial equipment costs may exceed those associated with hiring a small plane for one day of survey, ownership of a UAV which can be flown frequently for several years with relatively little advance planning or training makes the investment worthwhile. UAVs are also capable of flying at lower altitudes and slower speeds than private planes, drastically improving the spatial resolution of remotely-sensed data and aerial images. Several recent studies have explored these and other benefits of UAV-based aerial thermography.

The newly-established Archéodrone project at the University of Toulouse 2, France, is conducting ongoing UAV-based thermography research (Poirier, Hautefeuille, and Calastrenc 2013). They use a radio-controlled octocopter equipped with global positioning system (GPS) and an inertial stabilization system and is capable of lifting 3 kg. The thermal camera used is a FLIR T620 that has a resolution of 640 by 480 pixels and is capable of detecting temperature increments as small as 0.04° C. Automatic flight paths are created using the MikroKopter Tool software which allows the user to program waypoints, flight speed, and altitude onto a map downloaded from Google Earth or similar websites.

Poirier and coauthors published a short report on preliminary Archéodrone project results in 2013. They conducted surveys at Saint-Bertrand-de-Comminges, an ancient roman town in southern France, and at Kroomdraï and Sterkfontein, prehistoric sites in the South-African Cradle of Humankind (Poirier, Hautefeuille, and Calastrenc 2013: 206). Images from these surveys were monitored live, and still frames were extracted and processed to enhance thermal anomalies, but were not composited to create complete site maps. Results at the former site found that linear thermal anomalies corresponded well with streets and buildings. At the latter locations, they were able to detect several underground cavities (Poirier, Hautefeuille, and Calastrenc 2013: 306). This outcome confirms the results of previous research as well as highlights the potential of aerial thermography to discover not just cellars and storage pits, but cave sites, which can be valuable sources of well-preserved artifacts, ancient art, and human remains.

Jesse Casana, John Kantner, Adam Wiewel, and Jackson Cothren conducted a similar UAV-based thermal survey at the Blue J community in New Mexico (2014). The southwest is known to be problematic for most types of geophysical remote sensing, as the terrain is too rough for ground-penetrating radar and the common stone building materials are generally undetectable by magnetic gradiometry or electrical resistivity (Casana et al. 2014: 217–218). Casana and his coauthors sought an alternate solution by means of aerial thermography.

Casana et al. (2014) used a FLIR Tau II LWIR thermal camera mounted on a gimbal fixed to a Cinestar 8 octocopter. The camera was sensitive to 0.05° C temperature increments and recorded 640 by 512 pixel video at 8-bit radiometric resolution (Casana et al. 2014: 210). Using MikroKopter, they programmed the UAV to follow transects at a speed of 5 m per second and an altitude of 70 m. This speed and altitude were selected as a compromise between the need to collect high-resolution images over a large area and the limitations of the Cinestar, which has a maximum flight time of approximately 15 minutes. They spaced these transects only 20 m apart to ensure that the resulting images had sufficient overlap for photogrammetric processing (Casana et al. 2014: 211–212).

Casana et al. (2014) collected four thermal videos, one in the evening and three in the early morning, as well as a set of color aerial images. Using AgiSoft PhotoScan and Microsoft Image Composite Editor (ICE), video frames were extracted, mosaicked, and georeferenced with ground control points. These software programs allowed the creation of a site-wide, high resolution composite image with a mere fraction of the manual labor previously required. The final image had a ground resolution of 6 to 7 cm and covered a 220 by 360 m total surface area (Casana et al. 2014: 212).

Casana et al. (2014) compared their thermograms to the color images and records of the Blue J site created during 2004 and 2006 archaeological surveys and excavation. Several roomblocks and plazas had been mapped during the previous excavation and then backfilled, leaving only a few remains visible on the surface. Casana et al. successfully detected most of these known archaeological features, which appeared as high-value areas in the thermograms due to the low thermal inertia of the stone building materials. They also detected several anomalies that seem to indicate the presence of previously undetected architecture and warrant further investigation (Casana et al. 2014: 217).

In the analysis of their results, Casana and coauthors noted that their first morning flight at 5:18 am, just before sunrise, seemed to be the best for detecting archaeological features (Casana et al. 2014: 213). The stone architecture had retained enough heat to stand out in the thermograms while most of the surrounding soils and vegetation had cooled with the change in diurnal flux. The evening flight was heavily obscured by warm vegetation noise, since the water content in the vegetation allowed even small grasses to retain heat into the evening and mask the thermal response of the ground. The later morning flights did not capture clear images of subsurface features as the warming surface had already started to cover their responses, although their 7:18 flight did produce a crisp image of microtopography in the reflected thermal radiation. However, perhaps the most exciting of their observations was that well-timed thermal imaging was consistently successful at detecting ancient stone architecture in rocky, sandy soil where other remote sensing techniques had repeatedly failed (Casana et al. 2014: 218).

Throughout the brief history of aerial thermography, the technology and methodology have steadily improved. Thermal cameras have evolved from large, airplane-mounted scanners to tiny handheld varieties. Spatial resolution has increased from just over one meter to under ten centimeters. Image processing now allows the swift and relatively simple creation of large-scale, high-resolution image composites. However, in nearly all case studies the quality of thermal data has only been judged by comparison with other types of data sets, such as site maps or the results of other geophysical surveys, the only exceptions being Périsset and Tabbagh (1981) and Casana et al (2014). To accurately assess the most productive conditions for aerial thermography, we must also compare sets of corresponding thermograms that were collected at the same location, but under a wide variety of conditions.

4. Experimental Plot

4.1. Setup

Périsset and Tabbagh's argument for the benefits of planning a thermal survey around long-term heat flux is strong. However, tracking this flux is a very involved, time-consuming process that is generally beyond the scope of most archaeological field research projects (see Périsset and Tabbagh 1981: 174–175; Scollar et al. 1990: 598–600; Haley, Johnson, and Stallings 2002: 3). Instead, most archaeologists will have to rely only on diurnal flux due to their limited field time. Acknowledging this reality, I designed an experiment to help assess the best time of day as well as the best weather conditions for data collection. I built a test site that could be monitored and recorded at regular intervals in all conditions. To narrow my focus and reduce variables, I included only a limited combination of simple features in this experimental plot.

The area in which I set up the experimental plot was a level patch of open grassland among the fields owned by the University of Arkansas' agricultural research department in Fayetteville. I selected a rectangular area measuring approximately 4 m by 6 m and oriented roughly north-south along the long axis. It was located on level ground in an open field, away from any trees or other structures that might create shade.

University agricultural department personnel used a backhoe to excavate the plot to a depth of about 0.3 m. I then added several simple feature types common to many archaeological sites within this test plot. Each feature was oriented east-west, parallel with the short sides of the test plot. They included a ditch, a clay berm, and six walls (Figure 3). The ditch measures 30 cm wide and 30 cm deep. This puts the bottom of the ditch 60 cm below the level of the ground surface. The clay berm was constructed out of the material removed from the ditch. It was hand-packed into a rough mound measuring approximately 30 cm across at the base, with its top lying 15 cm below the surface.

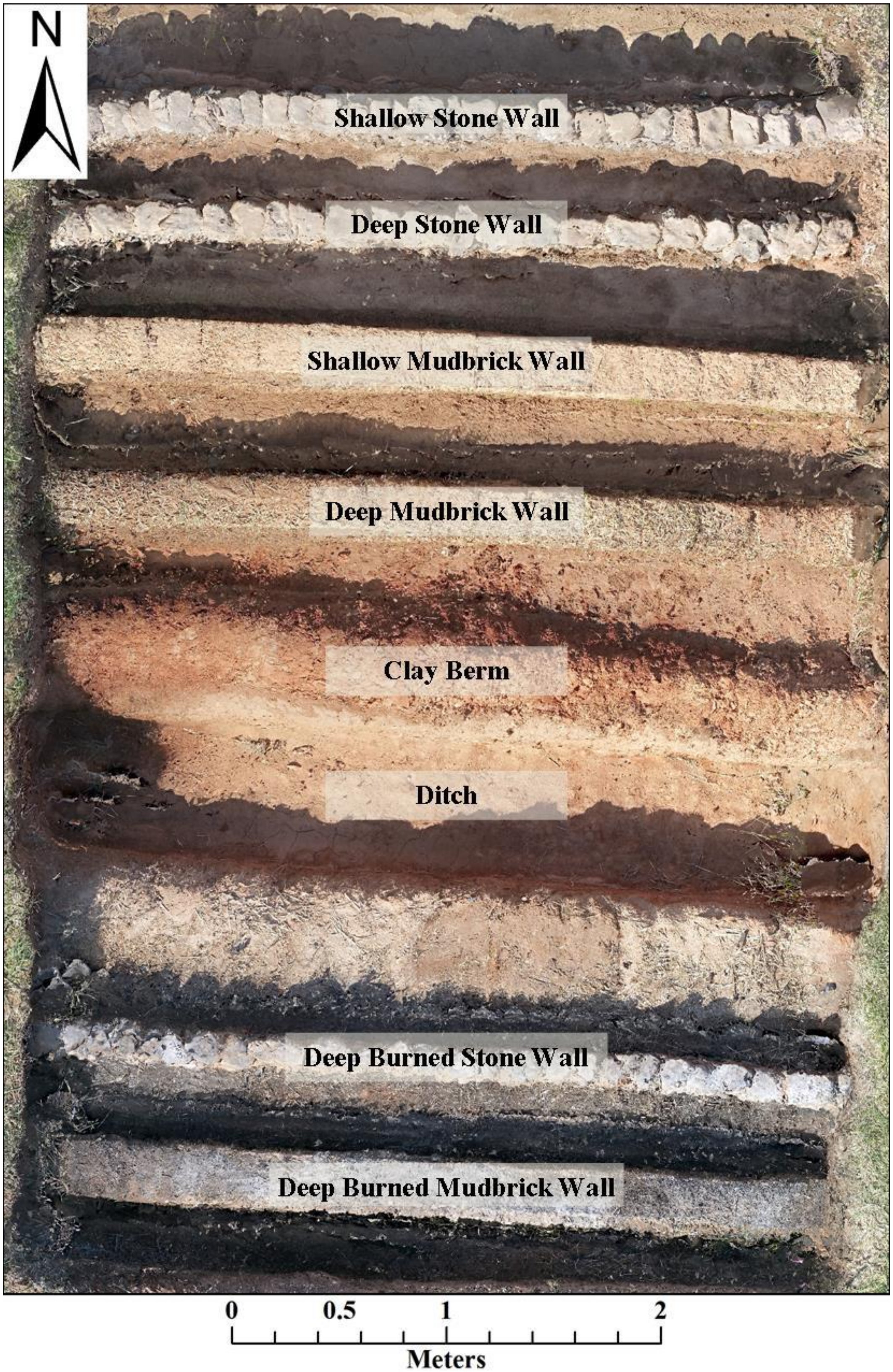

Figure 3: Plan view of the experimental plot before backfilling (Image: Autumn Cool).

Figure 4: Students constructing walls in the test plot (Image: Autumn Cool).

I constructed the walls with the assistance of several students (Figure 4). The three stone walls were made with of Arkansas Fieldstone purchased from a local landscaping supplier. Arkansas Fieldstone is a type of sandstone quarried from the Hartshorne formation in the Ozark Mountains of Arkansas. It has a density of 149.3 lbs per cubic foot and an absorption rate of 2.8% (Stone Descriptions & Specs 2013). The individual stones are fairly flat and uniform in size, averaging roughly 5 cm thick and 15 cm diameter. The stone walls were formed by stacking a single row of stones mortared with a simple mixture of water and native clay. We built one stone wall to a height of 25 cm so that its top lay just 5cm below the level of the original ground surface. The second and third stone walls were only 15 cm tall, leaving their tops approximately 15 cm below the level of the original ground surface.

The three mudbrick walls we constructed were assembled out of 105 hand-made mudbricks. Undergraduate students prepared the first 40 bricks as an experimental archaeology lab activity (Figure 5). We mixed the bricks in a wheelbarrow using a combination of the clay which had been excavated from the test pit, sand, and hay. We did not measure the proportions of each component as the bricks were mixed, so there were inconstancies between batches. We shaped the bricks in a wooden mold that could produce three 25 cm by 25 cm by 8 cm bricks at once and then sun-dried them for several days. As with the stone walls, I constructed the three mudbrick walls by stacking single rows of bricks to create one shallow and two deep walls. The final mudbrick walls were 25 cm wide and lay roughly 5 and 15 cm below the surface.

Figure 5: Mudbricks dry in the sun while a student prepares the mold for a new batch (Image: Autumn Cool).

To create additional variation in the wall features, I burned one each of the deep stone and mudbrick walls (Figure 6). The firing took place over two days. I maintained the first fire for approximately 3 hours and the second fire for 4 hours. Wary of creating a large, indistinguishable burned area, I tried to keep the fire isolated from the surrounding floor and sides of the test pit by focusing it solely on the tops of the walls. I did this by layering wood charcoal, kindling, and damp hay on each wall top. As the kindling and charcoal caught fire, I added more damp hay on top to maintain a hot, smoldering fire. Although this method prevented the walls from heating all the way through to their bases, and the fire did not match the heat of a kiln, my hope was that this would be a fairly accurate imitation of an accidental burning of a dwelling or storage structure.

Figure 6: Wall burning (Image: Autumn Cool).

After completing construction of the features, I divided the plot in half along the north-south, or long, axis. With the help of several students, I refilled the western half of the plot with the original clay soil and the eastern half with fill sand purchased from a local quarry. By backfilling in this manner, I ensured that each feature was buried half under clay and half under sand. Unfortunately, a small section of the shallow stone wall was knocked over by the sand as it was poured out of the dump truck. I then leveled the backfill to be even with the surrounding undisturbed ground. I placed aluminum pie plates at the corners of the test plot to act as ground control points (GCPs), which aid in georeferencing the data. I later added four additional GCPs made out of aluminum foil crosses to the sides of the plot after several attempts at georeferencing data failed. Throughout the study this plot remained naturally free of vegetation due to the winter season. It was also not covered with sod or topsoil, which would obscure any patterns in the thermal images. Thus all of the experimental plot data is concerned only with thermal prospection on bare soil.

4.2. Data Collection

The data I collected at the experimental plot consisted of both color images and thermal video. I recorded a set of color images prior to backfilling as a visual record of the features and so that I could reconstruct a 3D model of the walls, ditch, and berm in PhotoScan (Figure 3, Figure 10). The color images were taken with a Samsung Galaxy S3's 8 megapixel camera with the resolution set at 3264 by 2448 pixels.

The thermal camera used was FLIR's Tau II LWIR uncooled camera core with a 19mm lens. This camera records thermal radiation between 7.5 and 13 μm at a sensitivity of <50 milliKelvins. This sensitivity rating indicates that the FLIR can distinguish between temperatures that differ by less than 50 mK (equivalent to 0.05° C). It is capable of operating in ambient temperatures ranging from -40 to 160° C and has a high lens speed of f/1.0. It records 8-bit video at a 30 Hz frame rate with a resolution of 640 by 512 pixels and pixel pitch of 17 μm (FLIR Systems 2015).

I used an Orion StarShoot LCD-DVR was used to record the thermal video to an SD card. The StarShoot records video with a maximum input resolution of 720 by 576 pixels at a 30 Hz frame rate (Orion StarShoot LCD-DVR 2015). It records the thermal data on a relative 8-bit scale. Each video frame is a grayscale image made of 256 different shades, where black cells represent the coldest values and white the warmest. As the camera films it constantly adjusts the distribution of these gray values to fit the range of temperatures in each frame. One effect of this constant calibration is that identical temperatures in different frames will not always be represented by the same gray value.

The FLIR was housed in a custom-made aluminum case and powered by an external USB battery. Initially, I placed the FLIR and accessories in a picavet attached to the end of a painter's 16-foot extension pole. A picavet is a suspension system used by kite photographers to stabilize a camera (e.g. Digital Camera Setup 2013). A single string is threaded through a series of U-hooks fastened to the rim of a plastic tub and then through two carabiners. I later replaced this system with a more stable hinged camera housing built by Jesse Casana (Figure 7).

Figure 7: The string picavet (left) and the hinged suspension system (right) (Image: Autumn Cool).

The camera was originally powered by a Duracell USB battery with 500 mAh. This battery had a tendency to lose power quickly, especially in colder temperatures, which caused fogginess to obscure the thermal video. Most videos remained clear for five to six minutes, but some became unusably clouded within two minutes. This issue was resolved by switching to an Asus USB battery with 3000 mAh.

I collected thermal video by walking transects across the test plot with the FLIR suspended from the end of the painter's extension pole (Figure 8). As I did not use a harness or other stabilization system for the pole, the angle at which I held it varied between approximately 60° and 70°. This resulted in thermal images with spatial resolutions varying between 0.3 and 0.4 cm. These images were collected over the course of three months during both day and night and under a variety of weather conditions to create a diverse data set. At each collection, the current time, weather conditions, air temperature, wind speed, and humidity were recorded in a field notebook (Appendix B).

Figure 8: The author collecting thermal data of the experimental plot (Image: Autumn Cool).

After recording the thermal video, I used a Raytek MiniTemp MT4 infrared thermometer to measure the ground surface temperature at three points each in the sand and clay sections of the test plot. This IR thermometer is effective in ambient temperatures between 0 and 50° C and capable of recording surface temperatures from -18 to 400° C. It is accurate to within 2° C when the actual temperature is between -1 and 400° C, or to within 3° C when the actual temperature is between -18 and -1° C (MiniTemp: Portable Infrared Thermometer 2004). When recording surface temperature, the MiniTemp thermometer was always oriented vertically and held 24 cm above the ground surface to maintain consistency between measurements.

In addition to recording temperature, I collected soil moisture content data. For this step I used a Delta-T SM150 Soil Moisture Sensor with the HH150 Hand Held Meter attachment. This sensor records the soil moisture as a percentage by volume with an accuracy of within 3% (Delta-T Devices 2015). I took measurements at three separate points in both the sand and the clay sections of the test plot to establish a mean value. Soil moisture and sand temperature are summarized in Appendix B.

Finally, I acquired additional temperature data and sunrise/sunset times from Weather Underground (The Weather Channel, LLC. 2015). Weather Underground hosts a historic archive of National Weather Service meteorological data which allowed me to supplement my field notes with detailed reports of the weather conditions leading up to each data collection event. The data I selected originated at weather station KFYV, the nearest official NWS station to the experimental plot. Located at Drake Field in Fayetteville Arkansas, the KFYV station records climatic conditions every hour. This data has been charted in Appendix A.

4.3. Data Processing

To prepare my data for analyses I created thermograms from the thermal video feed. For this process I first attempted to use AgiSoft PhotoScan, which is able to stitch together overlapping photos to create 3D representations of scenes or objects by identifying common points between images to reconstruct geometry (AgiSoft PhotoScan User Manual: Professional Edition, Version 1.0.0 2013: 4). It is now being widely used by archaeologists to create everything from orthorectified digital elevation models and site maps to 3D models of individual artifacts (e.g. Casana et al. 2014; Magnani 2014; Verhoeven 2011). However, I discovered that still frames extracted from my thermal videos would not align in PhotoScan. This is likely due to the constant auto-calibration of the FLIR as thermal data is recorded. Since identical temperatures are not recorded as identical gray values across frames, it is difficult for PhotoScan to pinpoint corresponding points in overlapping images. In addition, many images may have been either too blurred or simply too uniform for PhotoScan to correctly match corresponding points. This issue continued even after adding more GCPs to assist with image alignment.

I was able to successfully create thermograms of the test plot using Microsoft Image Composite Editor, a free photo-stitching program. Microsoft ICE is capable of creating mosaics directly from most videos or collections of photographs. I found that my thermal data had too much blurring and too little contrast for the automatic mosaic from video function to work. Instead, I first used the free program ImageGrab to extract one frame per second from the video feed (Glagla 2010). I then manually sorted through the frames to remove blurry images before importing them into Microsoft ICE for automatic mosaicking. The final image composites were saved as Tiff files.

This image mosaicking process often took multiple attempts to select the best frames for compositing. Several early videos never produced a useable thermogram. This issue was almost completely resolved after blurring was significantly reduced by switching from the string picavet to the hinged suspension system. Adding additional GCPs also improved photo alignment. However, even many of the successful thermograms contain visual artifacts created by the FLIR’s auto-calibration process. Inconsistencies between the relative grayscales used to represent temperatures on separate transects and individual image frames create light and dark patches in the thermograms that are not associated with physical features within the experimental plot ().

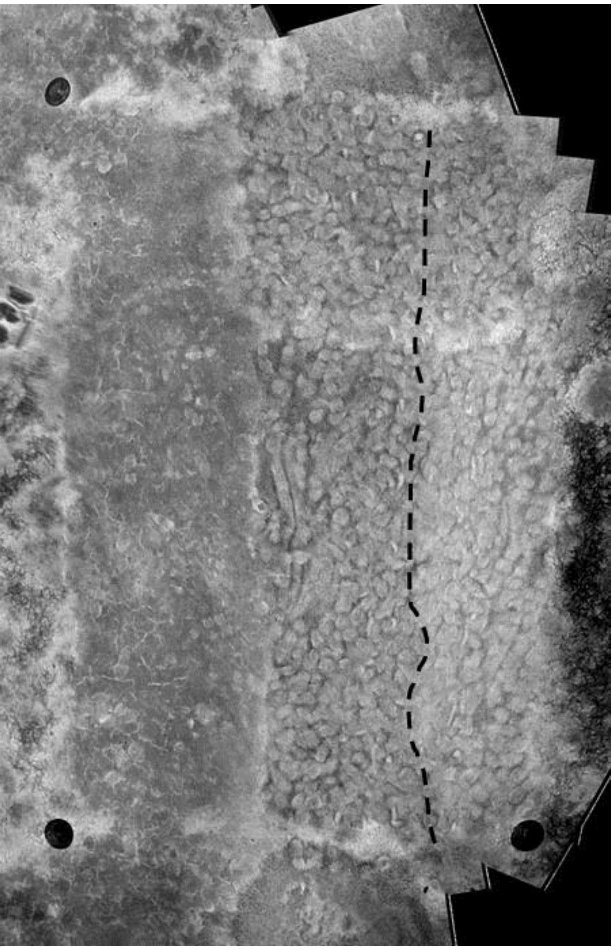

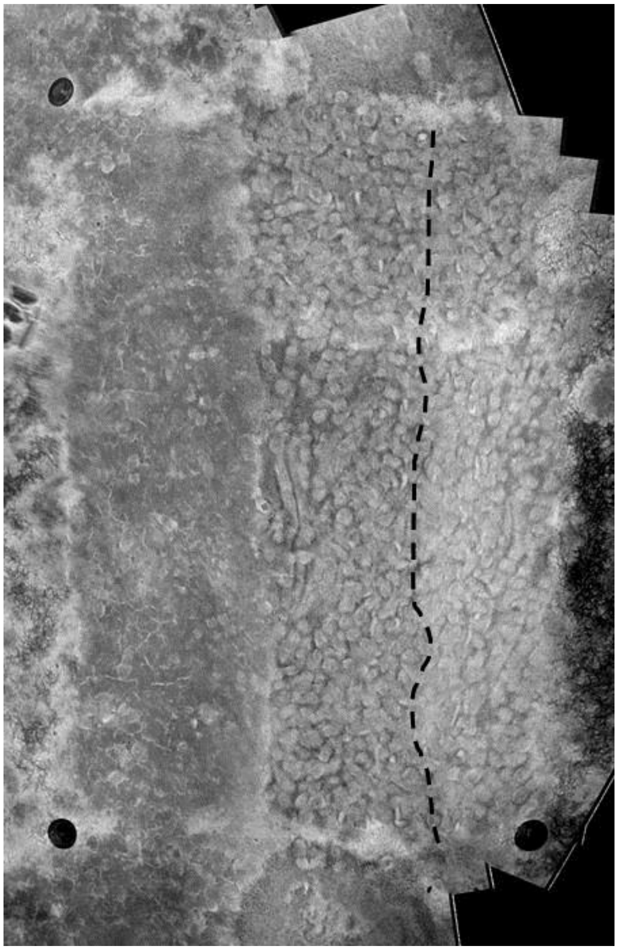

Figure 9: The dotted line on the thermogram indicates a visual artifact created by the FLIR's auto-calibration process. To the right of the line, the image is light because the original transect overlapped the very cold grass at the edge of the test plot. To the left of the line the image is darker with more contrast because the temperature range within that transect was smaller.

I used AgiSoft PhotoScan to process the color images of the features in the experimental plot. PhotoScan is able to stitch together sets of overlapping images by first identifying common points to create a sparse point cloud. It then uses this sparse point cloud to calculate the original camera positions and parameters, as well as to build a 3D polygonal mesh that links overlapping images. Next, I visually identified the GCPs in the individual images, marked them, and imported their coordinates. PhotoScan uses these coordinates and the estimated camera positions to correct image alignment and create a dense point cloud (Figure 10). It then constructs a new 3D polygonal mesh out of this dense cloud to fill in the detailed geometry of the surface. The final product was a full-color, geometrically correct map of the features within the experimental plot (Figure 3). I exported this image as a Tiff file for further processing.

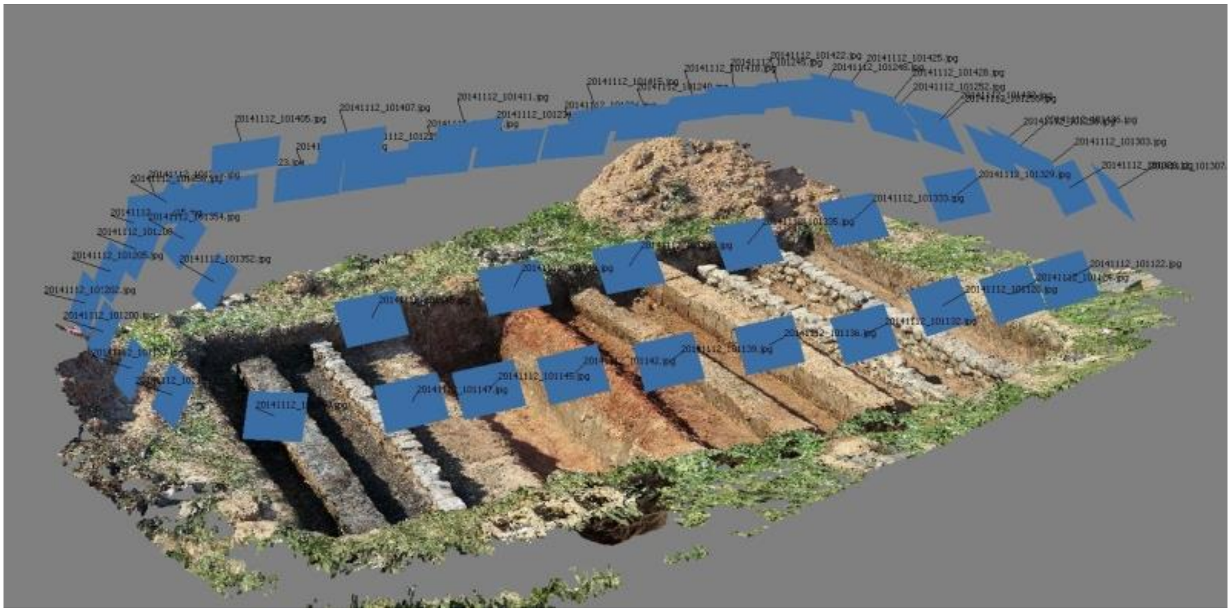

Figure 10: Dense point cloud of the experimental plot, produced in AgiSoft PhotoScan. Blue squares represent estimated camera positions.

I used ArcMap 10.1 to georeference the color feature map and the thermograms. I used an arbitrary coordinate system based on the actual plot dimensions. With ArcMap's georeferencing tool I assigned coordinates to each visible ground control point. ArcMap uses these coordinates to transform and align the images, so the later images with more GCPs had significantly better alignment. I then layered them to help identify the source of visible anomalies as well as to allow comparison between thermograms. I visually assessed the results of the thermal imaging to determine which features were visible in each thermogram. I cross-referenced this information with the ambient temperature, soil temperature, soil moisture, time of day, and weather conditions to look for correlations.

In addition to creating the thermograms and color reference image, I processed several thermograms together to look for temporal thermal anomalies as described by Danese et al. (2010, also see section 2.2). To apply their analytical method to my data, I needed to calculate the standard deviation of corresponding cells across several thermograms. I selected the seven thermograms that had been acquired during the evening of March 22 and the morning of March 23 as they were among the highest-quality images and had strong alignment.

To calculate the standard deviation of cell values, we must first calculate the mean thermal value of the thermograms on a per cell basis. If x_i is the value of cell X in thermogram i, the mean μ of all values of x_i is calculated by the equation:

$$\mu = \frac{1}{N}\sum_{i=1}^{N} x_i$$

The standard deviation σ of the values of cell X can then be calculated with the equation:

$$\sigma = \sqrt{\frac{1}{N}\sum_{i=1}^{N}(x_i - \mu)^2}$$

Again, this calculation is repeated for each cell to find the thermal variation per cell. The outcome is a new raster dataset where each cell no longer represents a temperature, but instead displays the standard deviation of all of the temperature ranges within each corresponding cell across the seven thermograms. I used IDRISI's map calculator tool to apply these equations to the dataset. The resulting images will be discussed in the next section.

4.4. Results

Out of the forty thermal videos recorded I was able to create twenty-six orthorectified thermograms (see Appendix D for complete collection). Seven of these were only partial images or were poorly mosaicked with obvious errors. Five of the poor images were collected before the new battery and stable camera mount were incorporated. The remaining two may have been blurred due to weather interference or human error. From these results I have been able to draw several conclusions regarding the effects of the soil matrix, feature characteristics, weather, and timing have on the success of thermal imaging.

The soil matrix or background environment in which archaeological features are embedded can be the deciding factor in the success or failure of thermal prospection. As stated in Section 2.1, dense or slightly moist soil generally has higher diffusivity (the ratio of conductivity to heat capacity) than dry or porous soil of the same type. However, very high water content will actually begin to decrease soil diffusivity as increasingly more thermal energy is used to heat and cool the water, which has both high heat capacity and high thermal inertia (see also Stanjek and Faßbinder 1995: 97–98). These properties can be clearly observed in the thermal behavior of the sand and clay matrixes of the experimental plot.

The sand-filled experimental plot had by far the best results, revealing at least one feature in nearly all images. The large-grained, porous sand has less heat capacity than the clayey soil and high conductivity, resulting in high diffusivity and very low thermal inertia. The sand warms quickly during the day and cools just as fast at night. The high diffusivity enables thermal energy to travel through the matrix with little attenuation, allowing subsurface features with higher thermal inertia to transmit their thermal signatures to the surface. However, it is also a very noisy matrix as even slight variations in the surface topography of the sand are visible. In the case of my experimental plot, the sand section is riddled with footprints in all thermograms. At night these footprints are warmer than the ridges in between then, and during the day they are cooler. This trait can be ascribed to the mild compaction of the footprints, which has slightly increased heat capacity and thermal inertia compared to the loose sand of the ridges.

Water content alters the thermal properties of sand to a limited degree. When damp, the sand has increased conductivity and diffusivity, which in turn increases its thermal inertia. The diffusivity allows subsurface features to remain visible, but the increased thermal inertia somewhat minimizes the strength of their anomalies. This can be seen in the comparison of the March 15 and 22 8:30 pm thermograms (Figure 11). Both data sets were collected an hour after sunset and had very similar ambient and soil temperatures, but the March 15 data collection followed two days of rain and the recorded soil moisture was over one standard deviation above the mean and 2.5% higher than on March 22 (Appendix B, D). The anomaly created by the shallow mudbrick wall, although visible in both images, is much crisper in the March 22 image. However, the quick drainage properties of this porous sand prevents it from ever becoming so saturated that the very high thermal inertia of water itself would block deeper thermal signatures.

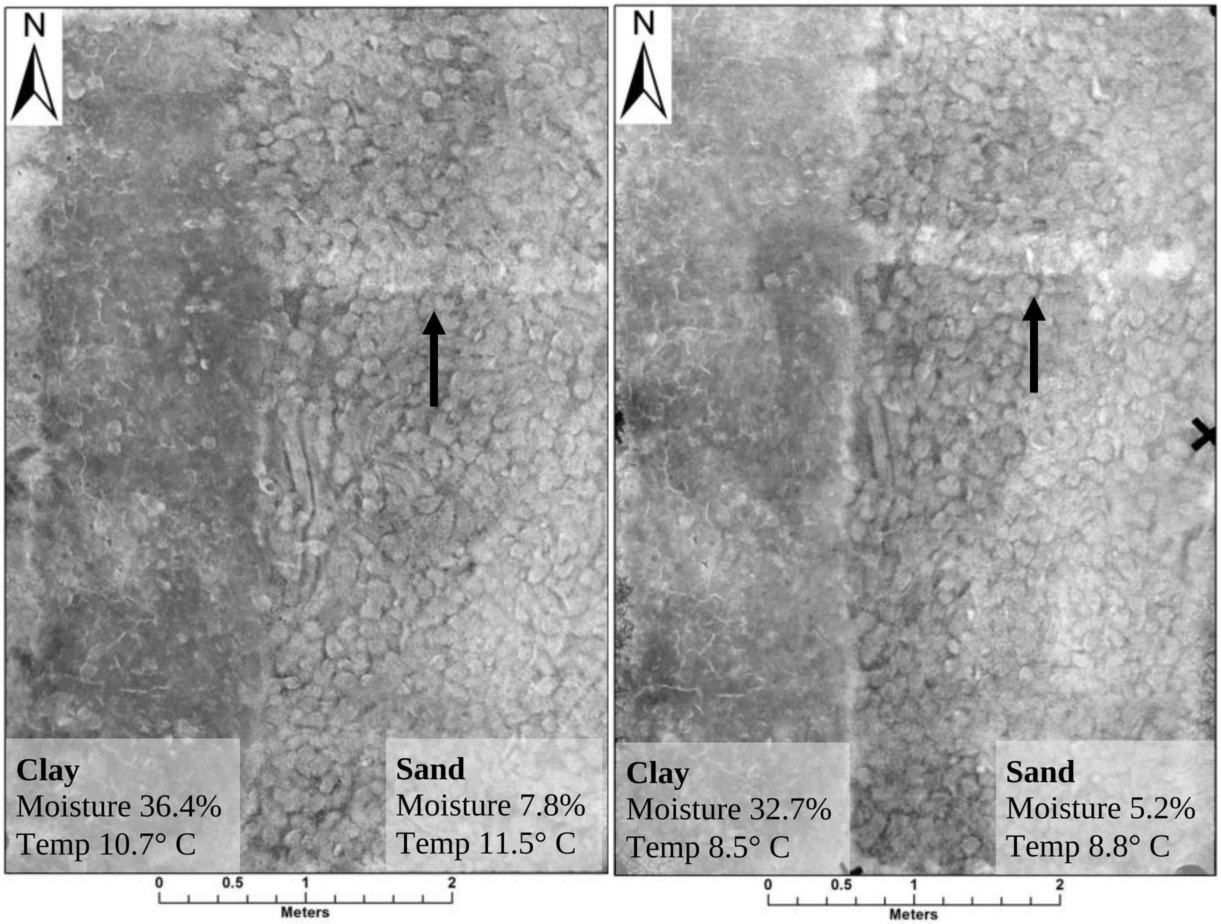

Figure 11: March 15, 8:30 pm (left) and March 22, 8:30 pm (right). Arrows indicate shallow mudbrick wall. Respective air temperatures were 58° F and 54° F.

In the clay half of the experimental plot I observed the opposite situation. Anomalies caused by the buried features are almost nonexistent. This is due to the high moisture content and density of the clay soil. While these characteristics allow it to retain large amounts of heat, it is resistant to temperature changes and conducts heat poorly. This results in low diffusivity, or a reduced ability to transport thermal energy. The clay ends up acting as a filter which blocks most heat from being absorbed and attenuates the transfer of what thermal energy does manage to penetrate the surface. This prevents features buried in the clay from warming or cooling quickly, regardless of their own inherent thermal properties, and also impedes whatever signals may be originating below the surface.

The characteristics and location of archaeological features determine their visibility in thermal images. The only feature that is visible in nearly all thermograms is the shallow mudbrick wall (Figure 11). It stands out brightly in the sand-filled half of the experimental plot. This is due to the water retention properties of the clay and straw mixture. The moist, dense mudbrick has high thermal inertia, so it remains cool well into the day and retains heat throughout the night. On the other hand, the more deeply buried mudbrick walls and the clay berm are not visible in any images. The depth at which these features are buried insulates them from most of the thermal radiation that creates changes in surface temperature. With their high thermal inertia, what little heat does make it to depth is unable to affect them.

The stone walls, with their high density and low absorption rate, have little water content. This results in lower heat capacity than moist materials such as the mudbrick walls. On the other hand, dense stone has high thermal conductivity, which increases diffusivity and thermal inertia. Thus while they cannot store as much heat as mudbrick, they are still slightly more resistant to temperature changes than dry or porous soils such as sand. With one exception, I was never able to distinguish any of the stone walls in the experimental plot using the thermal camera. In the west, clay-filled half of the plot this is unsurprising as the clay matrix blocks most thermal signals. In the eastern sandy portion, this is likely due to the close physical similarities between the sandstone and the sand itself, which produces very similar thermal signatures. If either a different type of stone or soil had been used, the results may have been very different.

The single instance when the stone walls were identifiable occurred at noon on March 2 (Figure 12). A light layer of snow on the ground had begun to melt, leaving very distinct snow marks over the experimental plot. Solid snow covered the clay half of the plot and the shallow mudbrick wall, the areas with the highest thermal inertia. A thinner layer remained over the ditch. Over the stone walls, however, the sand was bare. This was at first surprising as the stone walls should have slightly higher thermal inertia than the sand. However, this can be explained by the increased water content from the melting snow. While the stone walls do not absorb water readily, the sand around them became saturated, increasing its thermal inertia until it surpassed that of the stone walls.

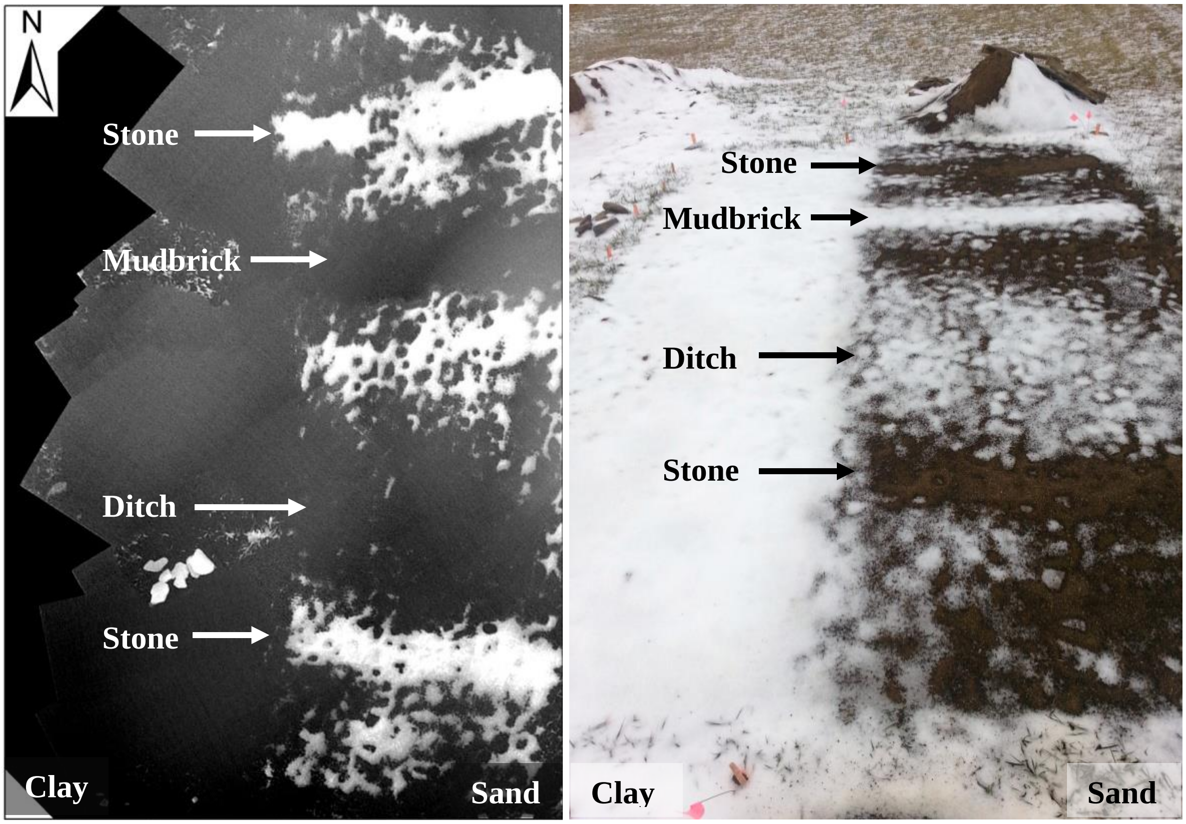

Figure 12: Thermogram (left) and color image (right) collected at noon on March 2. The sand above the stone walls is bare, but snow remains over the rest of the features. Note that colors are inverted as thermograms indicate warm areas with white (Photograph: Autumn Cool).

The final feature in the experimental plot, the ditch, is visible in half of the thermograms. Its signature is generally very faint. Surprisingly, the ditch is most often visible as a light, warm area in the clay half of the plot (Figure 13). This may be a result of the clay being less densely packed in the ditch. However, the warm anomaly in the clay also spreads a bit north from the ditch to cover part of the clay berm. This could indicate that the anomaly is not caused directly by the ditch itself, but by an inclusion in the clay matrix. When the experimental plot was excavated I noted that the topsoil had a higher loam-to-clay ratio than the subsoil. The ditch was the last area to be completely filled in, so we had been approaching the bottom of our pile of material and some of the loamy topsoil may have mixed in with the clay. Still, this should not necessarily be considered a flaw in the experiment design. Ancient ditches in archaeological sites are also usually filled with a higher concentration of topsoil, whether they were gradually filled over time by natural processes or backfilled by human hands.

The ditch is also visible in the sand matrix in several thermograms. It is most visible in two daytime images where it occurs as a cool, dark anomaly (Figure 12, Figure 13). The ditch is likely trapping water, which takes longer to heat than the rest of the plot. At night this water remains slightly warmer than the surrounding sand and the anomaly is reversed (Figure 13). In most thermograms, however, the ditch is not visible in the sand matrix, perhaps due to the overall low water content.

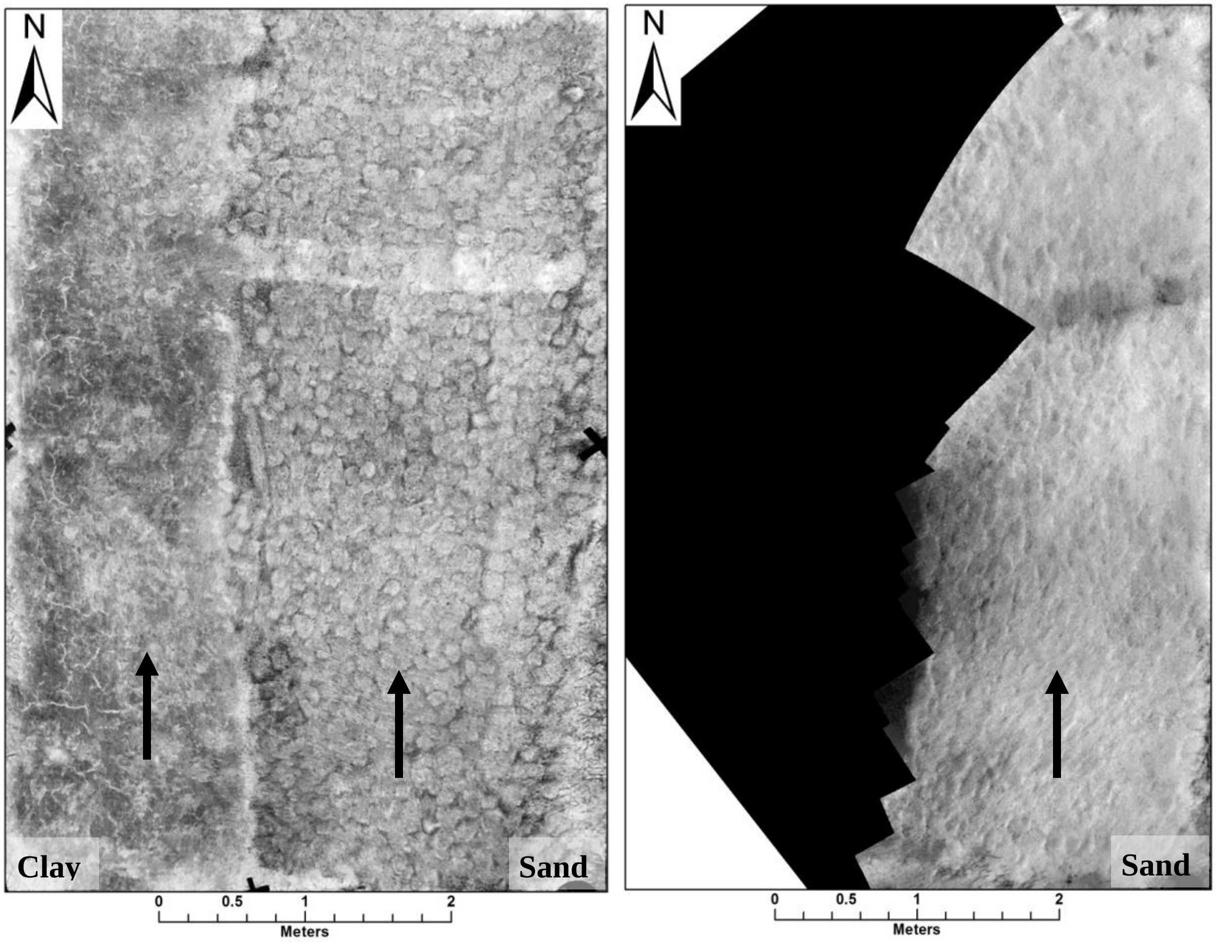

Figure 13: The ditch, indicated by arrows, appears as a light linear anomaly on March 23, 12:30 am (left) and as a dark anomaly at noon on February 27 (right).

While my data collection occurred over the course of only a single season, some small effects of weather on thermal prospecting may be observed in my thermal data. The clearest example is the March 2 image, where the snow marks as well as the thermal image revealed several features (Figure 12). As previously discussed, high water content due to the melting snow may have played a large role in the expression of the anomalies at this time. Therefore it is also possible that collecting thermal data shortly after a heavy rainfall, as the ground is beginning to dry, could have similarly crisp results.

The amount of cloud cover throughout the day does not appear to significantly affect thermal results. Instead, sustained high temperature appears to be much more important (Figure 14). The temperature variations on March 7 and March 11 follow a similar curve throughout the day. March 7 was clear while March 11 was mostly overcast and foggy. I collected thermal data one hour after sunset on both days. The March 11 thermogram has marginally better results despite the overcast day, probably due to the higher peak temperature. However, both thermograms are of relatively low quality and reveal only the faintest anomaly over the shallow mudbrick wall. In comparison, March 22 was overcast yet had on average higher sustained (although not absolute) temperatures throughout the 24 hours leading up to the data collection. The thermogram recorded one hour after sunset on this day has a much stronger anomaly over the same mudbrick wall. The sustained warm temperatures leading up to this data collection allowed the heat to penetrate the features better, so they had more absorbed thermal radiation to emit once the sun had set.

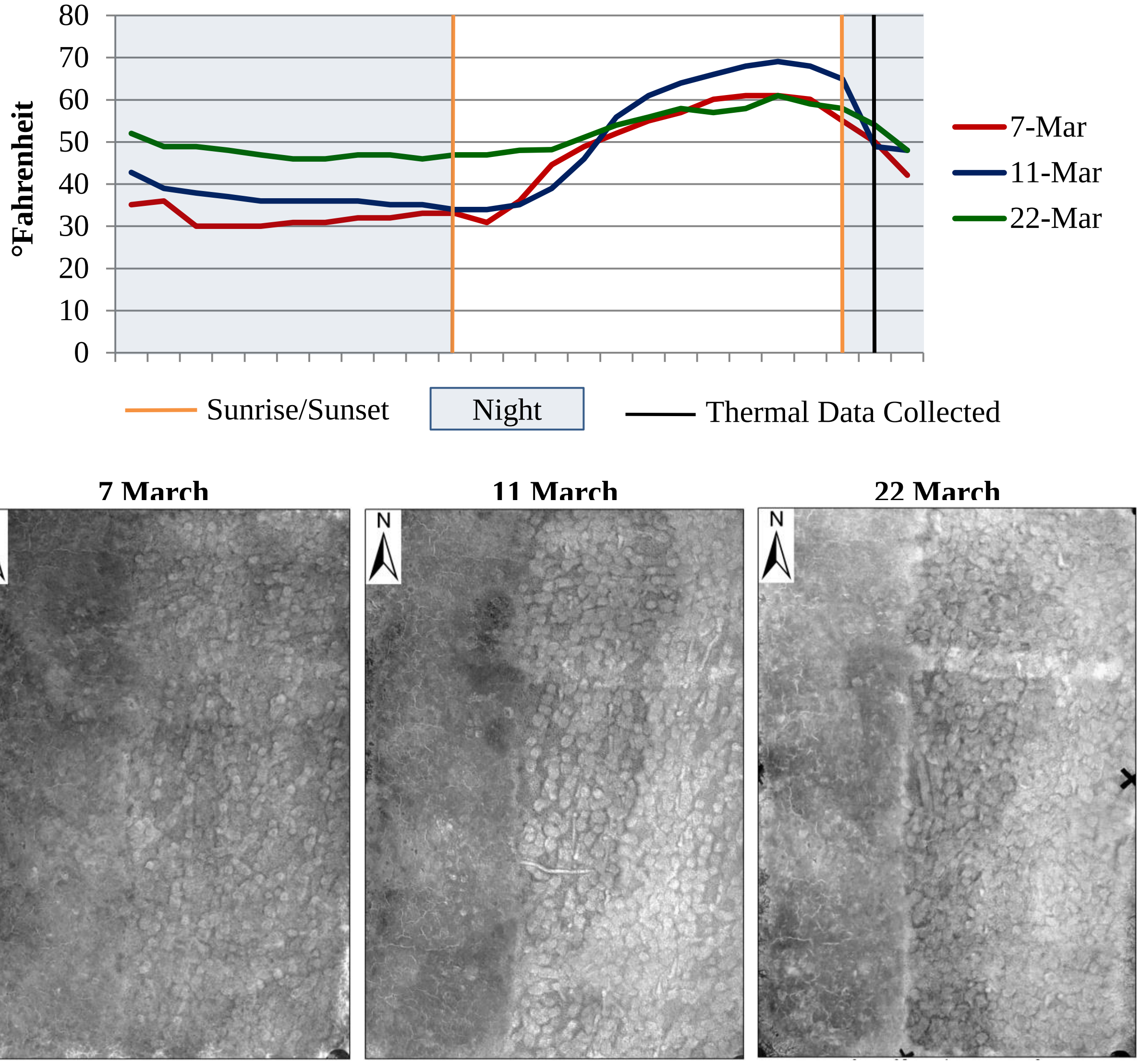

Clay	Sand
Moisture 35.2%	Moisture 6.1%
Soil Temp. 1.8° C	Soil Temp. 3.5° C

Clay	Sand
Moisture 36.4%	Moisture 7.8%
Soil Temp. 10.7° C	Soil Temp. 11.5° C

Clay	Sand
Moisture 32.7%	Moisture 5.2%
Soil Temp. 8.5° C	Soil Temp 8.8° C

Figure 14: Daily temperatures (top); thermograms (middle); associated metadata (bottom).

Perhaps the most important consideration when conducting a thermal survey is timing. As previous researchers have noticed, most thermography conducted during daylight hours will only reveal surface features and topography due to the reflected radiation. I have noted two exceptions to this rule (Figure 12 and 13). These two noon images revealed cold anomalies over the shallow mudbrick wall and the ditch. These thermograms were collected on overcast days while the temperature was still far from its peak, so the thermal radiation had not yet penetrated to subsurface features and there was less reflected radiation to mask their signals. However, other images taken in the afternoon show nothing but surface topography. This can be useful when topography reflects subsurface features, such as a shallow dip over an ancient ditch, but these topographic features are already identifiable by several other methods. Thermography is most revealing when used at night to discover subsurface features.

I have found it challenging to interpret exactly at what point during the night it is best to collect thermal data. My results are somewhat inconsistent. I collected thermal data every two hours during the nights of March 22-23 and 23-24 (Figures 15, 16, and 17). On the first night, the temperature continued to drop steadily until sunrise. All thermograms collected that night reveal fairly strong anomalies, with the clearest appearing between 10:30 pm and 4:30 am, 3 to 9 hours after sunset (Figure 16).

The second night, March 23-24, is less consistent. The best thermograms for identifying anomalies in this set are the 10:30 pm and the 2:30 am images (Figure 17). The 12:30 am, 4:30 am, and 6:30 am images show faint or no anomalies. The two later data sets may be accurate images as the temperature stayed fairly constant throughout this night. There was little diurnal flux to create thermal anomalies and what anomalies did exist would have faded into the background by this time. However, it is unclear why the 2:30 am thermogram would show strong anomalies while the 12:30 am does not. This may be due to a technical error that occurred during data collection or processing.

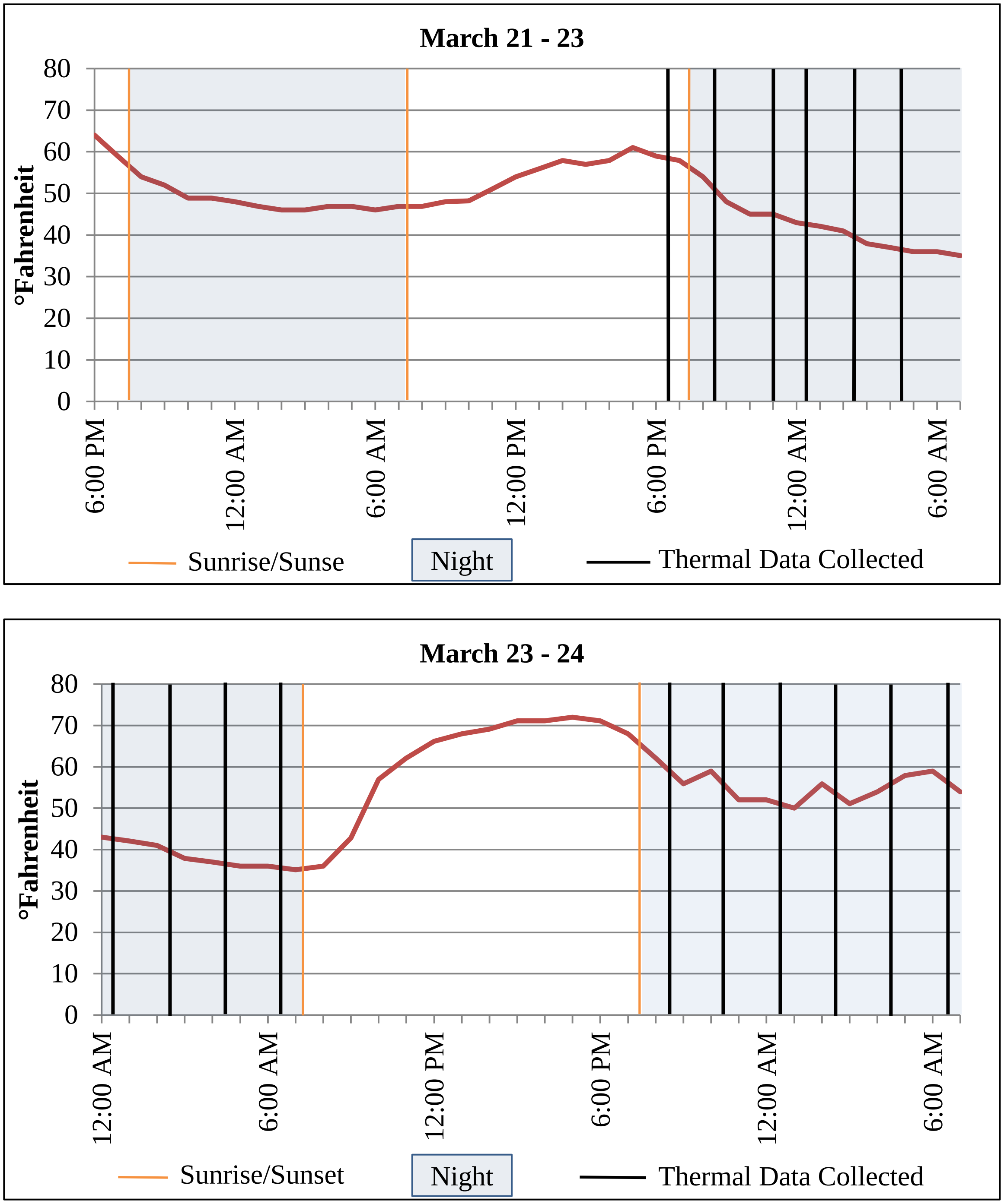

Figure 15: Chart of thermal data collection times compared to daily temperature.

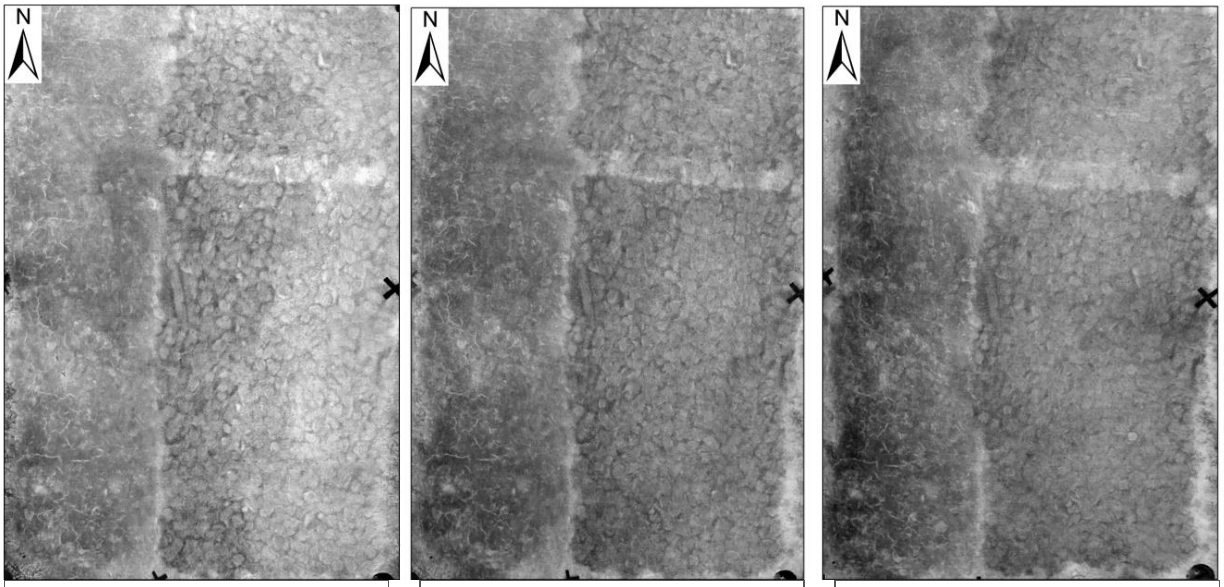

8:30 pm	
Clay	**Sand**
Moisture 32.7%	Moisture 5.2%
Soil Temp. 8.5° C	Soil Temp. 8.8° C

11:00 pm	
Clay	**Sand**
Moisture 32.2%	Moisture 5.1%
Soil Temp. 5.7° C	Soil Temp 6.5° C

12:30 am	
Clay	**Sand**
Moisture 35.3%	Moisture 6.3%
Soil Temp. 5.3° C	Soil Temp 6° C

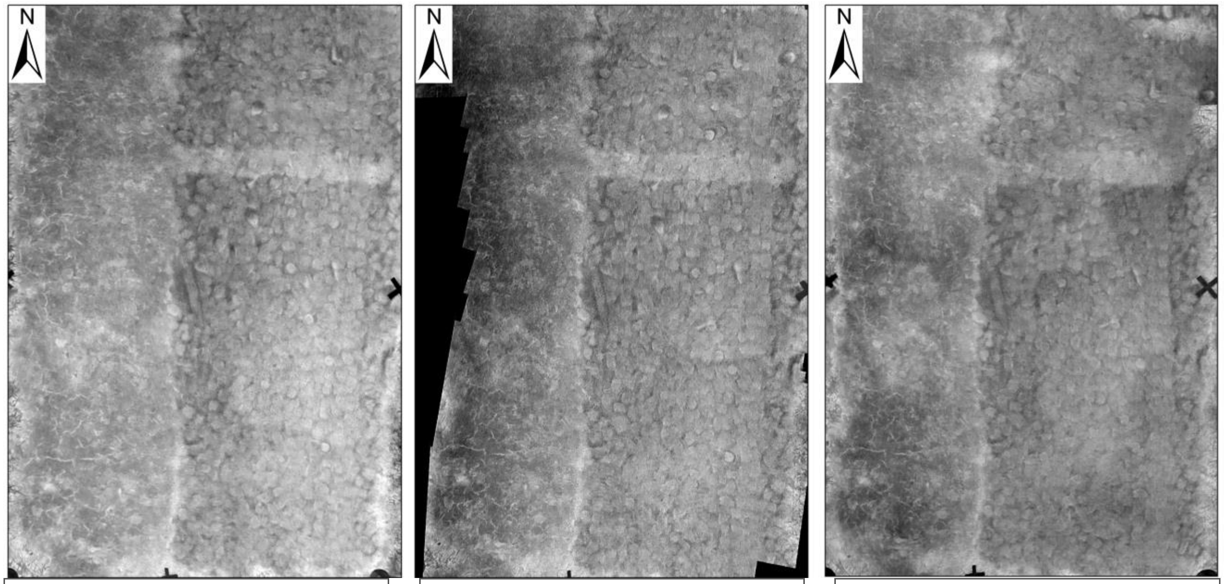

2:30 am	
Clay	**Sand**
Moisture 34.1%	Moisture 5.2%
Soil Temp. 3.7° C	Soil Temp. 4° C

4:30 am	
Clay	**Sand**
Moisture 33.8%	Moisture 4.7%
Soil Temp. 2.3° C	Soil Temp. 2.2° C

6:30 am	
Clay	**Sand**
Moisture 34.8%	Moisture 4.7%
Soil Temp. 1.7° C	Soil Temp 1.2° C

Figure 16: Thermograms collected the night of March 22 – 23.

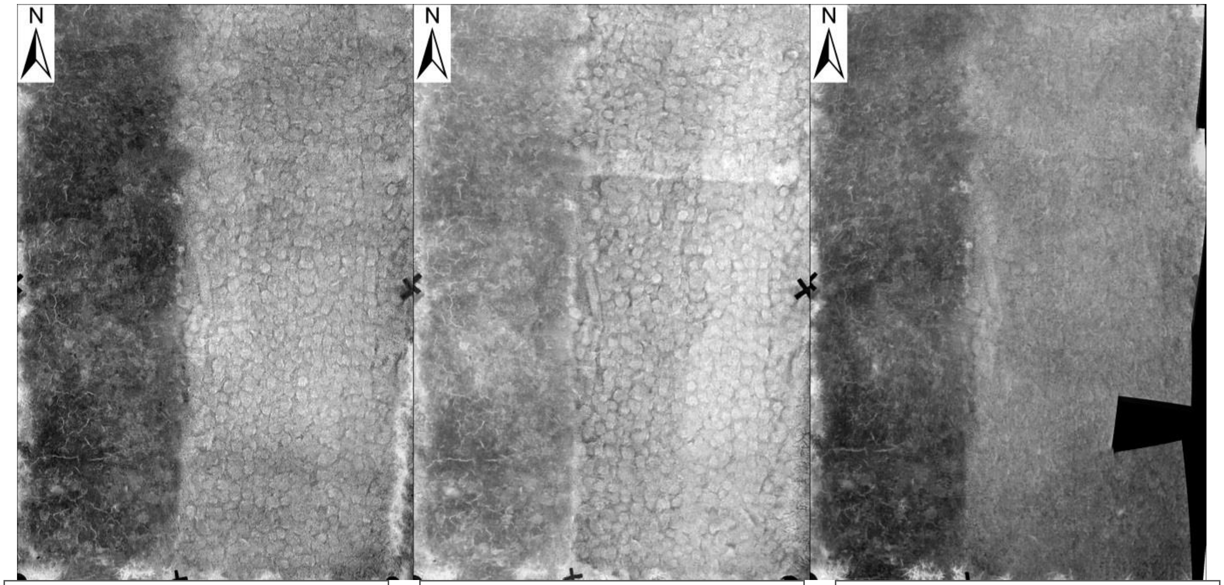

8:30 pm	
Clay	**Sand**
Moisture 31.5%	Moisture 6%
Soil Temp. 12.3° C	Soil Temp. 14.5° C

10:30 pm	
Clay	**Sand**
Moisture 30.7%	Moisture 5.4%
Soil Temp. 10° C	Soil Temp 11° C

12:30 am	
Clay	**Sand**
Moisture 30.8%	Moisture 4.9%
Soil Temp. 8.7° C	Soil Temp 10.3° C

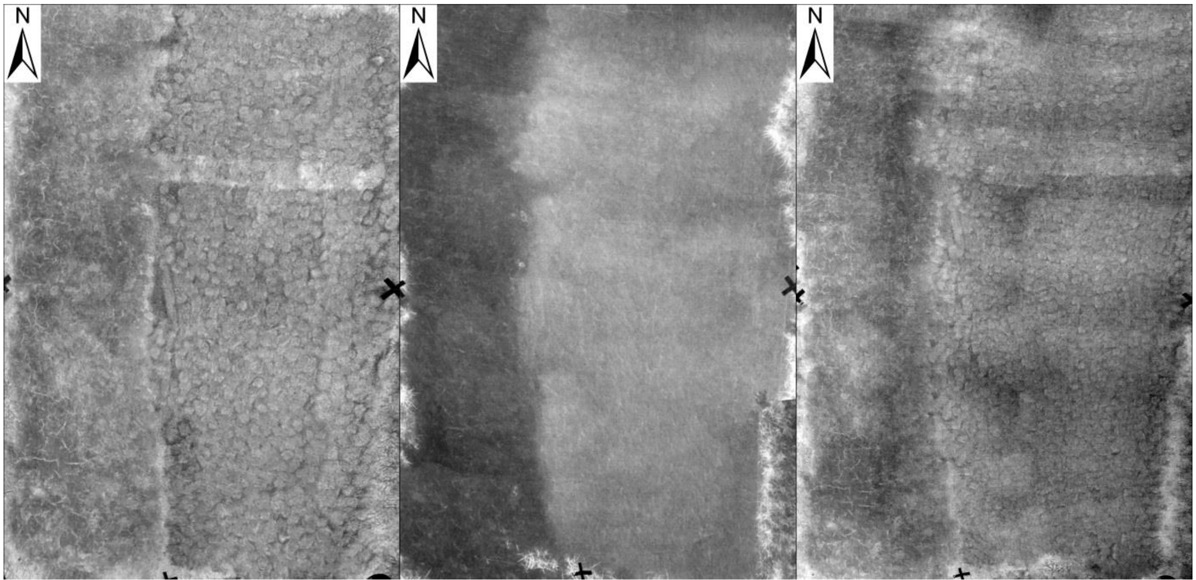

2:30 am	
Clay	**Sand**
Moisture 31.6%	Moisture 4.3%
Soil Temp. 7.5° C	Soil Temp. 7.8° C

4:30 am	
Clay	**Sand**
Moisture 31.6%	Moisture 4.6%
Soil Temp. 8.5° C	Soil Temp. 10° C

6:30 am	
Clay	**Sand**
Moisture 30.8%	Moisture 4.3%
Soil Temp. 8° C	Soil Temp 9.2° C

Figure 17: Thermograms collected the night of March 23 – 24.

From this data I can draw the rough conclusion that collecting data several hours after diurnal flux has changed from positive to negative generally provides a clearer picture in this particular context. This change usually occurs in the late afternoon and early evening with the drop in air temperature, so that the ideal imaging time starts two or three hours after sunset (see Appendix A for complete temperature data). Within the first hour or two after sunset, this change is relatively recent. Materials are still just beginning to cool, so there are few obvious thermal differences between the archaeological features and their surrounding soil matrix. As the night passes the differences grow more pronounced. Materials with low thermal inertia, such as the sand, cool quickly while high thermal inertia features buried within this matrix, such as the mudbrick wall, still retain heat. In other contexts this timing will vary. If the soil matrix of a site has an even lower thermal inertia than sand, anomalies will be visible earlier in the night. If the thermal inertia is higher, features and the background environment may remain indistinguishable until near sunrise. If there is no significant diurnal flux variation or temperature change as day goes into night, collecting quality data may not be possible.

At the time of year in which my data was collected, late winter and early spring, the diurnal flux does not become positive again until sunrise (Appendix A). It can be inferred from Périsset and Tabbagh (1981) that the thermal signatures of data collected after the morning transition from negative to positive flux will follow the same pattern as the night data, although anomalies will be reversed. Images taken immediately after the change to positive flux will show little distinction since all materials are just beginning to warm, while images taken several hours after diurnal flux transition will have stronger anomalies. I do not have any data for the hours immediately after sunrise, but my data collected in the late morning does show some strong anomalies despite significant noise from reflected radiation. In the late summer when this transition from negative to positive flux begins several hours before sunrise, it should be possible to capture these stronger anomalies closer to sunrise before reflection noise causes major interference.

The previous paragraphs discuss at which point during the day, based on lighting and diurnal flux variations, thermal data should be collected. It is also interesting to consider which type of flux, diurnal or transient, actually has the largest impact on the strength of recorded thermal anomalies, or if perhaps another variable is more influential than either flux type.

As discussed in Section 2.1, Périsset and Tabbagh (1981) state that transient flux variations are primarily responsible for creating thermal anomalies. They claimed that diurnal flux does not penetrate deeply enough to reveal to reveal subsurface features (Périsset and Tabbagh 1981: 169). Scollar (1990) countered that diurnal flux can produce useful anthropogenic anomalies (598). To make my own assessment, I again considered the thermograms collected approximately one hour after sunset on March 7, 11, and 22 (Figure 19). I compared them with the daily (Figure 18) and weekly (Figure 20) temperature variations to estimate the impact of diurnal versus transient flux.

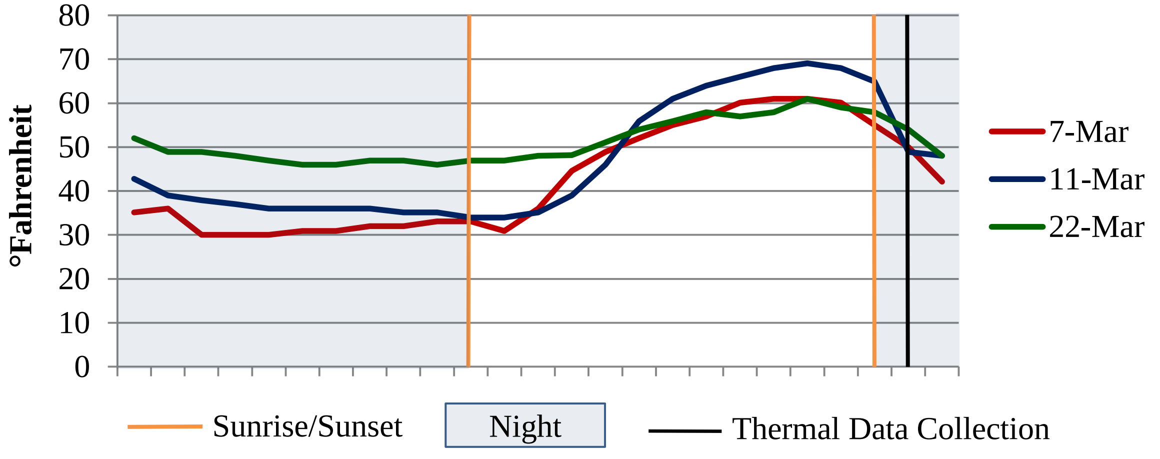

Figure 18: Daily temperature variation for March 7, 11, and 22.

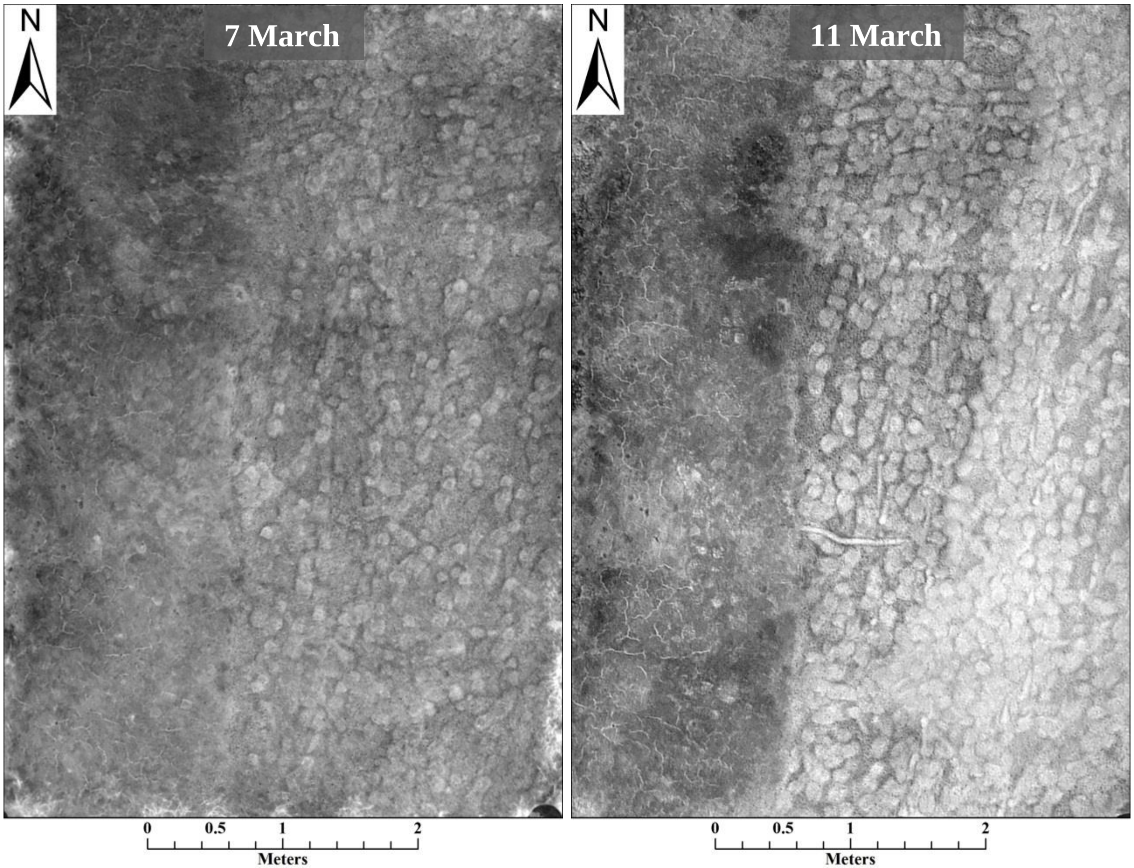

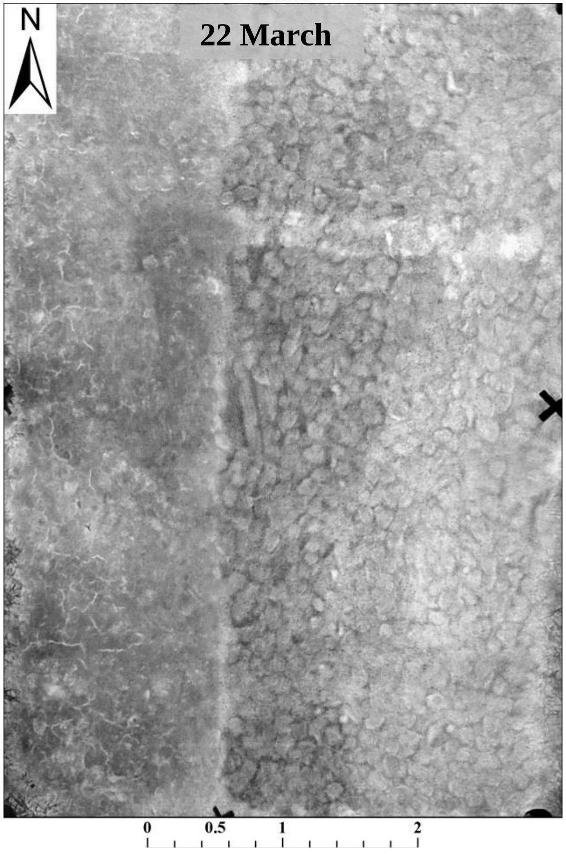

	Clay	Sand
7 March	Moisture 35.2%	Moisture 6.1%
	Soil Temp. 1.8° C	Soil Temp. 3.5° C

11 March	Moisture 36.4%	Moisture 7.8%
	Soil Temp. 10.7° C	Soil Temp. 11.5° C

22 March	Moisture 32.7%	Moisture 5.2%
	Soil Temp. 8.5° C	Soil Temp 8.8° C

Figure 19: March 7, 11, and 22 thermograms and associated metadata.

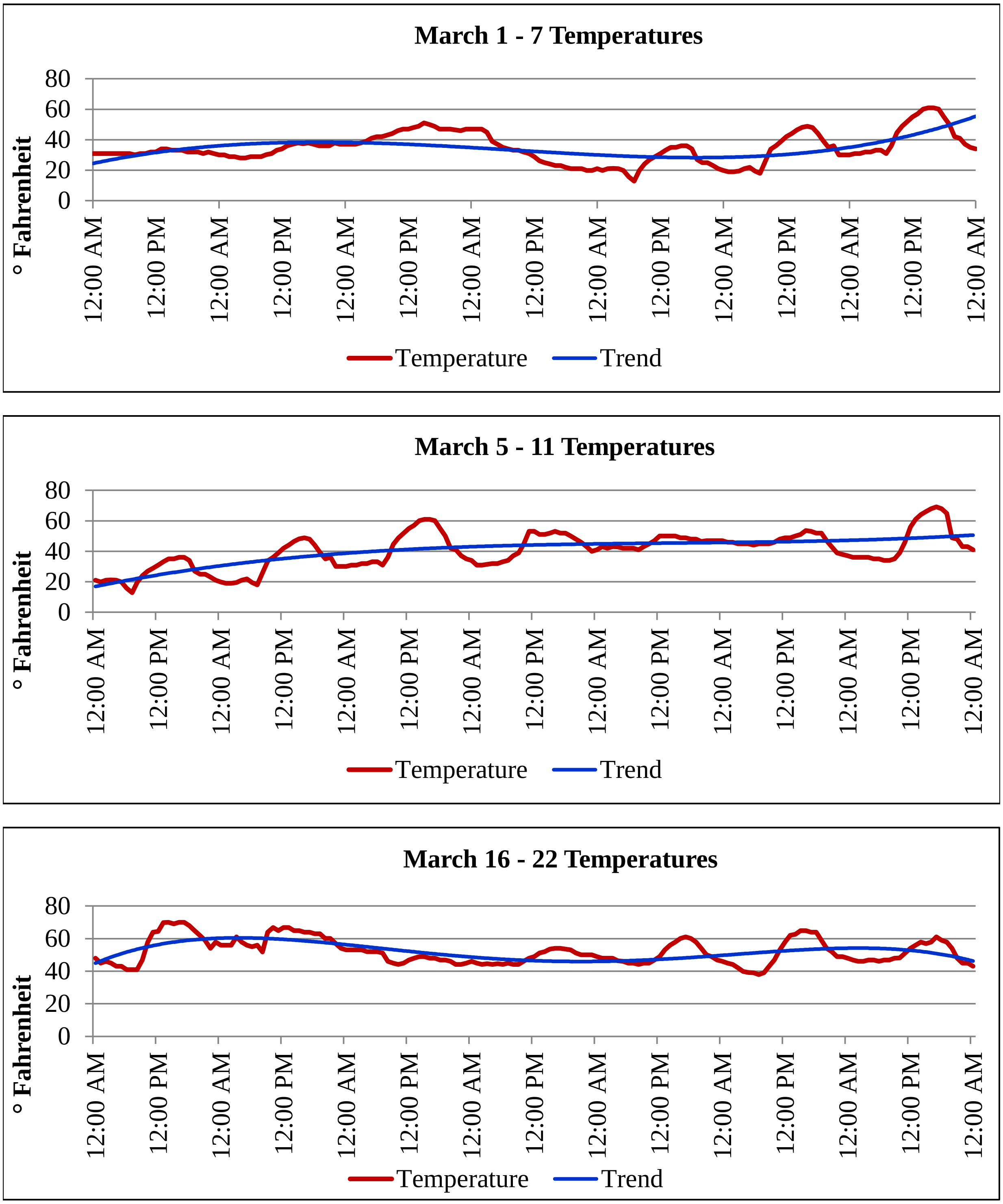

Figure 20: Weekly temperatures prior to data collection, with fourth-order polynomial trend line to estimate transient flux.

As previously pointed out, the March 22 thermogram clearly has the best results despite having the least dramatic diurnal flux (Figures 18 and 19). I stated that this may be due to the higher sustained temperature throughout the day leading up to data collection, which would have allowed more thermal energy to penetrate to subsurface features. It appears that the strength or amplitude of the diurnal flux variation itself does not have a major impact on the visibility of thermal anomalies.

In my consideration of transient flux I looked at temperature variations over the week prior to each data collection event (Figure 20). I did not apply the complex flux calculation methods presented by Périsset and Tabbagh (1981: 175-175) because air temperature, as the physical phenomena that creates flux, is a reasonable stand-in. I did create a fourth-order polynomial trend line to estimate general temperature trends over each week.

The week prior to the March 7 thermogram shows two flux variations, the second occurring approximately 48 hours prior to data collection. The week preceding the March 11 thermogram shows only a steady warming period with no flux variation. The week leading up the March 22 thermogram has three flux variations, the last occurring no more than 24 hours prior to data collection. These results are contrary to those of Périsset and Tabbagh, whose research generally indicated that data collected two or three days after a change in transient flux would have the most visible anomalies (1981: 172-175). If that had held true in this experiment, the March 7 thermogram would have been the clearest. Instead, it was the least revealing of the datasets. However, their claim is somewhat supported by the fact that the March 22 thermogram, recorded one day after a transient flux variation, is stronger than the March 11 thermogram, which had no preceding transient flux variation. Perhaps the timing of data collection with regards to transient flux is highly dependent upon the seasons or the amplitude of transient flux variations. In the spring, data collection might be ideally conducted very shortly after a change in transient flux, as is the case in my experiment. Perhaps in warmer months or regions with more drastic flux and temperature ranges, Périsset and Tabbagh's two or three day delay would produce better results. It is also possible that other variables, such as the amount of solar radiation the surface is exposed to each day, is actually more influential than temperature and flux. This is a variable which I did not consider during data collection, but should be investigated in the future.

The final set of results wanting discussion is that obtained by attempting the temporal processing technique suggested by Danese et al. (2010: 484). Her technique was based on the idea that temporal variation, or the lack thereof, in thermal anomalies may reveal subsurface features. By comparing thermal variation across corresponding thermograms and combining thermograms into a single comprehensive dataset, more anthropogenic anomalies may be discovered.

I used ArcMap 10.1's raster calculator function to create a thermal mean values image and a thermal standard deviation image from the March 22-23 thermograms (Figure 21). These images show the thermal mean and standard deviation on a per-cell basis using data from seven different thermograms. At least in this example, Danese's processing technique failed. The standard deviation raster reveals not a single identifiable anomaly. However, the thermal mean image highlights the shallow mudbrick wall under the sand as well as the ditch in both the clay and sand sections. I found this image to be extremely helpful, as until I created it I had not noticed the subtle, light ditch anomalies in the individual thermograms. While this processing did not provide the exact results I hoped for, it was still very informative and I will continue to experiment with mean values and standard deviations in the future.

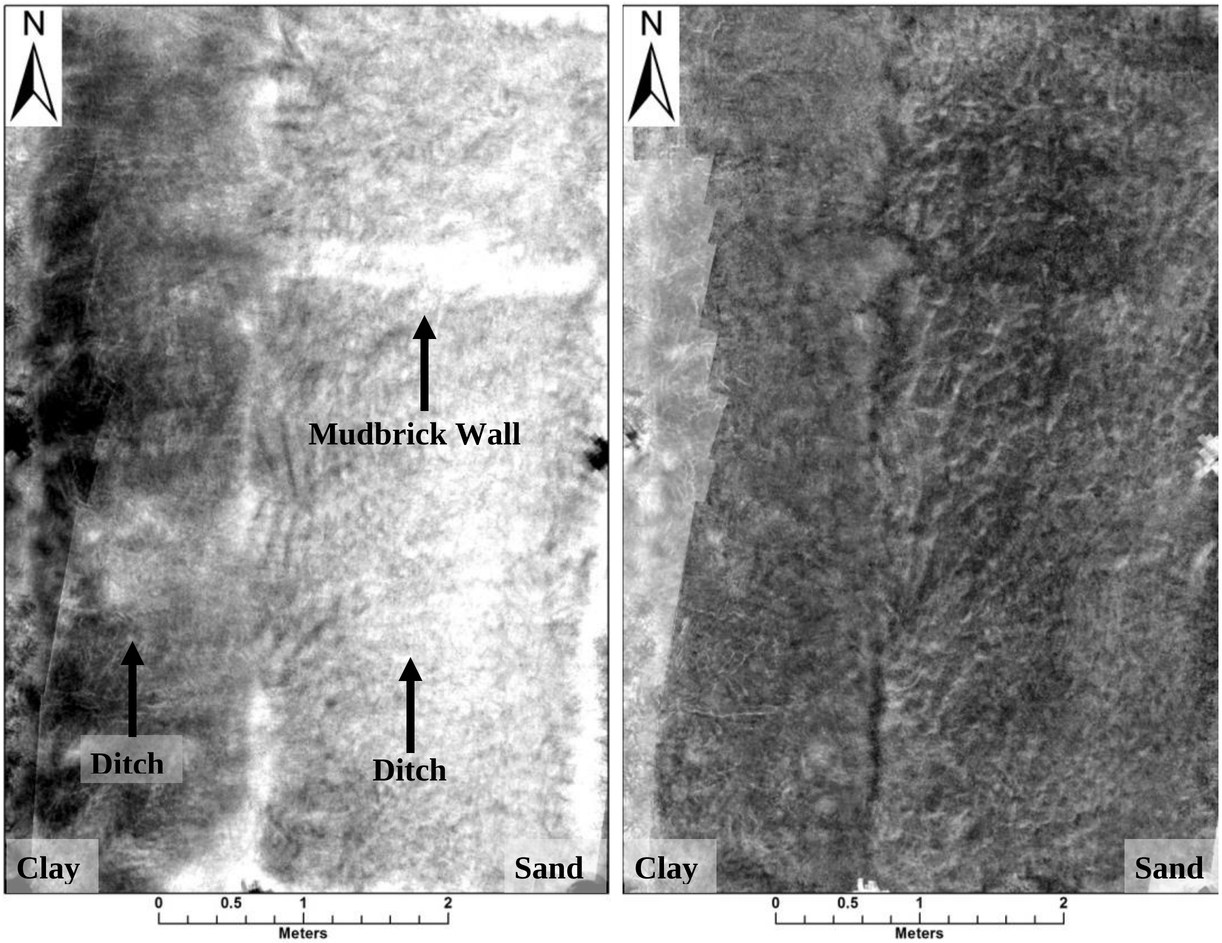

Figure 21: Thermal Mean (left) and Thermal Standard Deviation (right).

5. The Collins Site

5.1. Background

In addition to the experimental plot discussed in the previous section, I was interesting in employing aerial thermography in a field setting. Real archaeological sites rarely have so few environmental variables as my experiment and I was curious to see if field applications would be as productive. Furthermore, Jesse Casana and I were interested in exploring methods for reducing vegetation noise. As previously described in Périsset and Tabbagh (1981: 169), Scollar et al. (1990: 630-631), and Lundén (1985: 161), among others, vegetation acts a screen which obscures or distorts the thermal signatures of features on and below the ground surface. This has been a major limiting factor in the application of thermal prospection which archaeologists are still working to resolve (e.g. Bellerby, Noel, and Branigan 1990).

The Collins site, designated 3WA1, is multi-mound civic ceremonial center located alongside the White River in northwest Arkansas (Sullivan and McKinnon 2013; Kay, Sabo III, and Merletti 1989; Vogel 2005). It is currently being used as a cattle pasture and is covered with a thick layer of grasses, presenting an excellent opportunity for experiments with vegetation noise reduction. The Collins site dates to ca. AD 900 – 1400 in the Early to Middle Mississippian period (Sullivan and McKinnon 2013: 72). The site is located in an alluvial valley and remains relatively well preserved. It contains five documented mounds, A through E, that range from 0.5 to 3 m in height (Figure 22). No other archaeological features are visible on the surface.

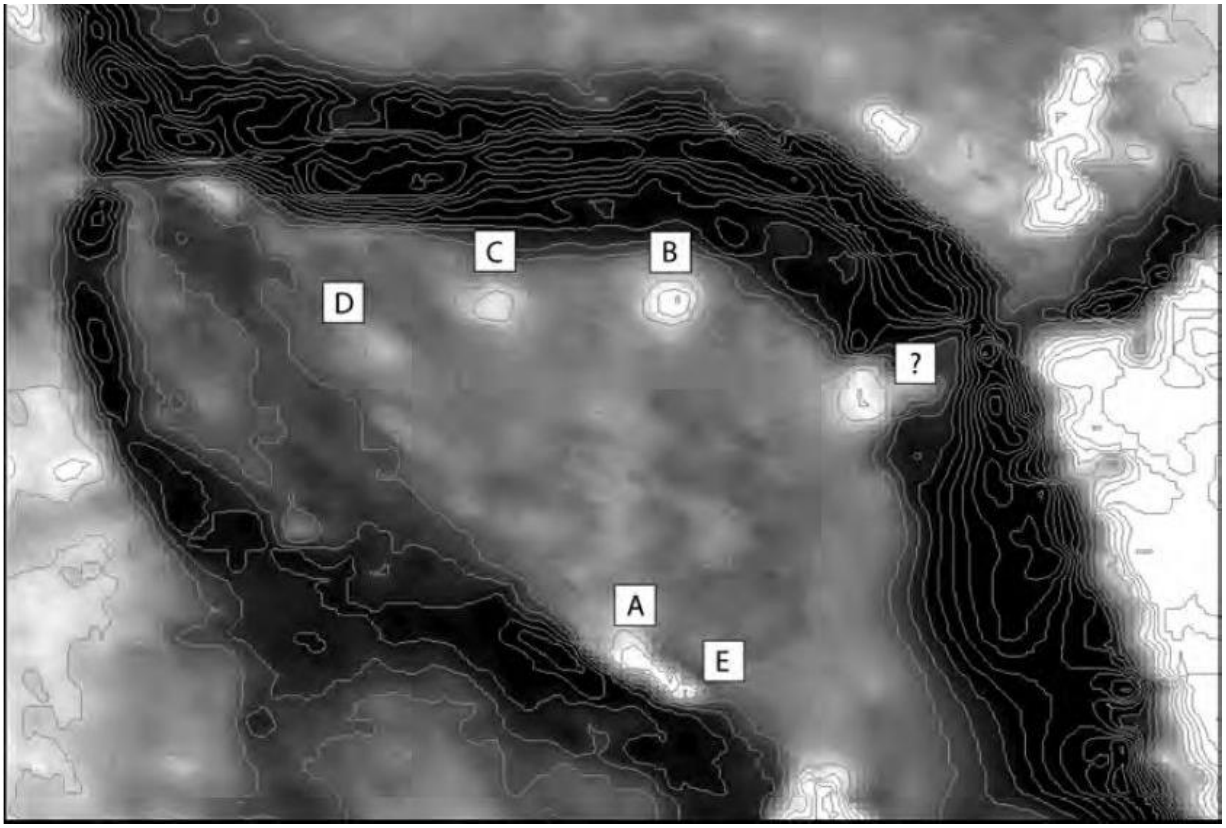

Figure 22: Map of the Collins Site (Sullivan and McKinnon 2013: 73).

Sullivan and McKinnon (2013: 79–81) conducted extensive geophysical surveys at the Collins site, and a magnetic gradiometry survey across the northern portion of the site reveals the presence of several structures located on and off of the mounds. The largest structure, on top of Mound C, is characterized by a very high magnetic signature. It was likely a charnel house used for the temporary interment of the dead. At designated times during the ritual calendar the dead were removed and the house was cleaned and ritually burned. A fresh layer of soil was spread over the remains and a new structure was built in the same location to restart the cycle. Repetitions of this process contributed to the formation of the mound. Mounds B and D also contained rectilinear structures, but their function is more ambiguous. In addition to the structures over the mounds, a number of smaller, off-mound rectilinear structures and a possible plaza area were also detected. A comparison of these magnetic gradiometry results with data collected during excavations of similar sites in the region suggests that the Collins site once served as a civic ceremonial center.

Stephanie Sullivan, Adam Wiewel, and Jesse Casana, and I conducted a thermal survey at Collins Mounds in the spring of 2014. We anticipated that this survey would provide a complementary dataset offering further information on the subsurface features identified with magnetic gradiometry. Furthermore, I saw the fairly homogenous layer of pasture grass covering the site as an opportunity to test a new thermal data processing technique that uses the Normalized Difference Vegetation Index (NDVI) to remove vegetation noise (see section 5.3). This research was originally described in a paper and video submitted to DRS Technologies' Student Infrared Imaging Competition (Cool, Wiewel, and Sullivan 2014; University of Arkansas DRS 2014 Thermal Imaging Competition Entry 2014).

5.2. Data Collection

We used a Cinestar 8 UAV made by Freefly Systems to collect aerial thermal, near infrared, and color images of the Collins site (Figure 23). This UAV has eight rotors and can lift approximately 2 kg. Average flight time of the laden craft is about 10 to 12 minutes, so to maximize efficiency we designed a flight path in the MikroKopter Tool program. MikroKopter guides the UAV along a series of transects between designated waypoints through the use of GPS. This also helped ensure that our final images would have sufficient overlap for mosaicking with photogrammetric software. We set the craft to fly at a 60 m altitude, at a speed of 4 m/s, along 200 m transects spaced roughly 20 m apart. We reserved manual flying of the UAV for takeoff and landing only.

Figure 23: The Cinestar 8 with FLIR in aluminum case mounted on the gimbal (Image: Autumn Cool).

We flew three flights over the Collins site to collect data. The color and NIR images were collected on March 24th at approximately 4:30 in the afternoon. The thermal video was recorded shortly before sunrise on March 25th, at approximately 6:45 am. The cameras were mounted on a gimbal fixed to the bottom of the UAV. A gimbal allows the camera to move independently and maintain a predetermined angle regardless of the rotation or tilt of the main body of the craft.

We again used the FLIR Tau II for the thermal data collection (see section 4.2). For color images we used a Nikon D600 digital SLR. This is a 24.3 megapixel camera with a 35.9 mm by 24.0 mm sensor. We set the D600's timer to take images at one-second intervals to guarantee complete, overlapping coverage of the site. For near infrared imagery, we used a Nikon D200 digital SLR, also set to collect images at one-second intervals. The D200 is a 10.2 megapixel camera with a 28 mm fixed focus lens. It had a modified Bayer filter installed to block any wavelengths below 0.72 µm (see Barnes 2013). This filter blocks visible blue and green wavelengths while allowing some visible red and NIR through. NIR-only is recorded in bands 2 and 3 of the Bayer filter, while band 1 records both NIR and partial visible red.

Twelve ground control points (GCPs) were distributed on the ground across the survey area in advance of the flights to aid in georeferencing the final image mosaics. Each GCP was mapped in real world coordinates through real-time kinematic survey with survey-grade GNSS (Global Navigation Satellite System). The aerial images were collected over Mounds C and B of the Collins site where the most striking features in the magnetic gradiometry data are located.

5.3. Data Processing

Our primary goal in the data processing described here was to find a method for reducing vegetation noise in thermal imagery. As few archaeological sites are covered only by bare soil, this is perhaps the primary obstacle deterring many would-be thermal prospectors. I hoped to minimize this concern by reducing vegetation noise using the Normalized Difference Vegetation Index (NDVI). The NDVI is an image processing method normally used to map and quantify vegetation health. By creating raster thermal and NDVI images and subtracting the latter from the former, we theorized that we could remove vegetation noise from the thermogram.

NDVI is calculated with the simple equation

$$NDVI = \frac{(NIR - R)}{(NIR + R)}$$

where NIR is reflected near-infrared and R is reflected visible red light. This formula is based on the spectral reflectance properties of plants. Chlorophyll, which gives plants their green color, strongly absorbs visible red light, while the cell structure of leaves reflects near-infrared light (Weier and Herring 2000). Healthy, leafy vegetation will then absorb most red light, resulting in an NDVI value close to 1. Unhealthy vegetation lacking in chlorophyll will instead reflect red light, resulting in NDVI values close to -1. A zero value indicates no vegetation.

To collect the information necessary to test this processing method, I needed to create a set of thermal, NIR, and red images. The first step was to extract still frames from the thermal video feed. For this process I again used the free program ImageGrab to extract one frame per second from the video (see Glagla 2010). I then manually sorted the thermal, color, and NIR images to delete pre- and post-flight photos taken while the UAV was on the ground as well as photos that were extremely blurry or lay outside the main survey area.

As in the previous chapter, I used Agisoft PhotoScan to produce orthorectified thermal, NIR, and color images of the entire survey area. I exported the final georeferenced images from PhotoScan as GeoTiff files. I also used the full-color images, the highest-resolution dataset, to export a digital elevation model (DEM) to retain natural and anthropogenic topographic information. I completed the remainder of the processing using ESRI's ArcMap 10.1.

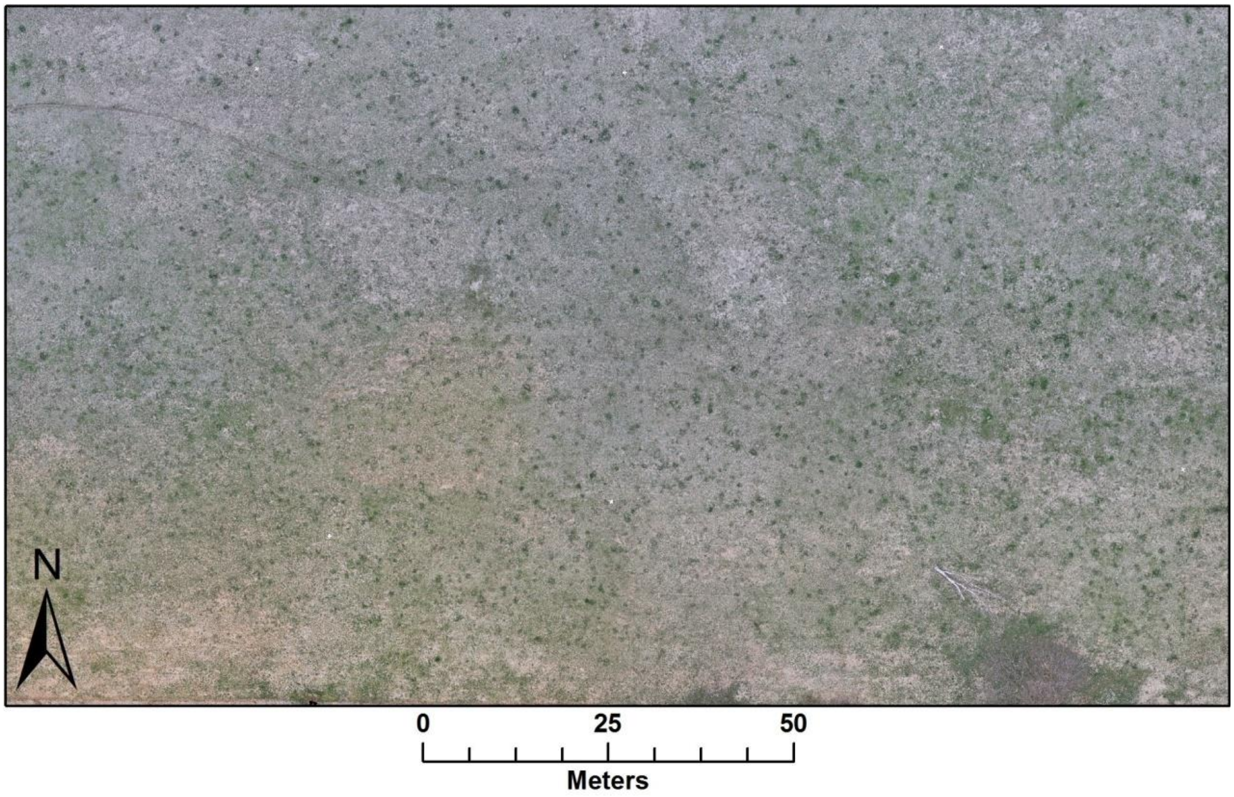

Figure 24: Color image of the Collins Site.

The PhotoScan-created GeoTiff files each contain four raster bands, including three normally used for RGB color display and one transparency layer. For the full-color image I imported all bands into ArcMap to display a realistic RGB image (Figure 24). For the thermal image I imported Band 1 only since all of the bands contained identical grayscale information (Figure 25). Similarly, I only imported band 3 from the NIR image as it is the IR-only band, while the other bands contained some visible red. All of these images are 8-bit files, meaning the cells in each raster band contain values ranging from 0 to 255.

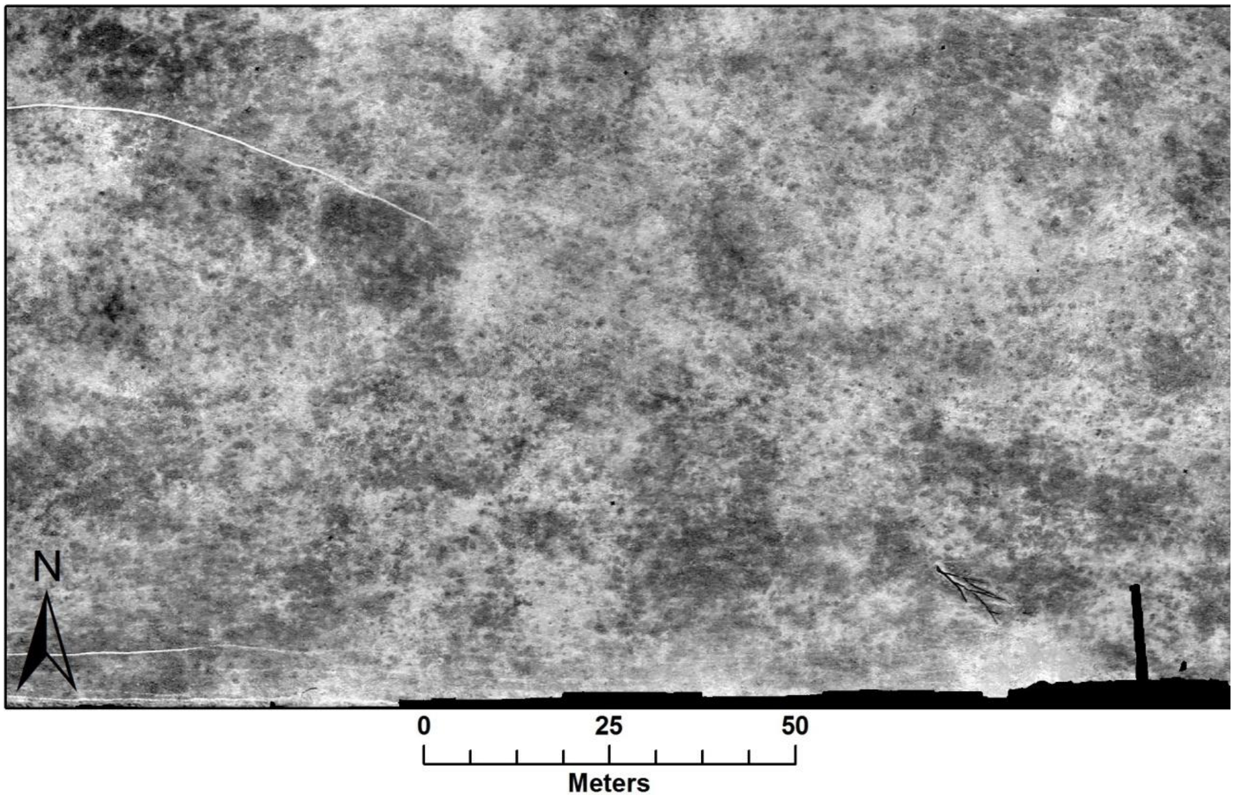

Figure 25: Original thermal image of the Collins site.

I used ArcMap's Raster Calculator tool to compute the NDVI using the red band from the full color image, the IR band, and the NDVI formula described in the previous section. The resultant NDVI raster contained values ranging from -1 to 1 (Figure 26).

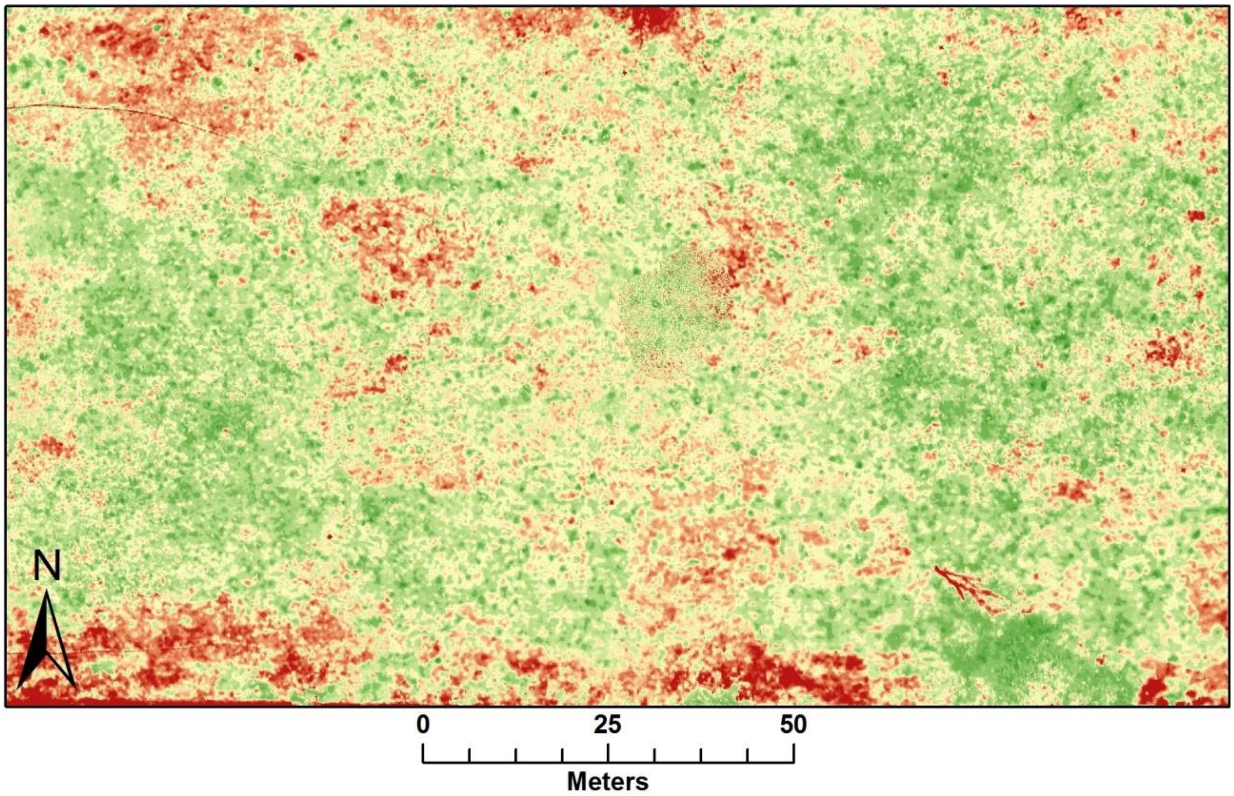

Figure 26: NDVI of the Collins site. Green areas indicate healthy vegetation.

To facilitate further map algebra with the other images, it was necessary to convert the NDVI back to a 0 to 255 range raster. In order to preserve the relative distribution of values and avoid losing any individual data points, this was accomplished with an affine transformation:

$$\mathit{To\ map\ value\ x\ in\ the\ range}\ [a,b]\ \mathit{to\ the\ corresponding\ value\ y\ in\ the\ range}\ [c,d]$$

$$y = (x-a)\frac{(d-c)}{(b-a)} + c$$

In this case the affine transformation is calculated with the formula

$$y = (x+1)127.5$$

This equation can then be entered into the Raster Calculator with the original NDVI layer input for *x*. The output raster is visually identical to the original image, but with the NDVI values now mapped onto the 0 to 255 range. Values below 127.5 indicate poor or unhealthy vegetation, values above 127.5 indicate healthy vegetation, and values exactly 127.5 indicate the absence of vegetation.

The final processing step in this experiment was to subtract the remapped NDVI from the thermal image to create a “sans vegetation” thermal image raster (Figure 27). This can then be overlain and compared with the other layers in ArcMap. I also imported the final images into ESRI’s ArcScene and draped them over the PhotoScan-generated DEM. This lets the images be viewed as pseudo-3D models and can often aid interpretation.

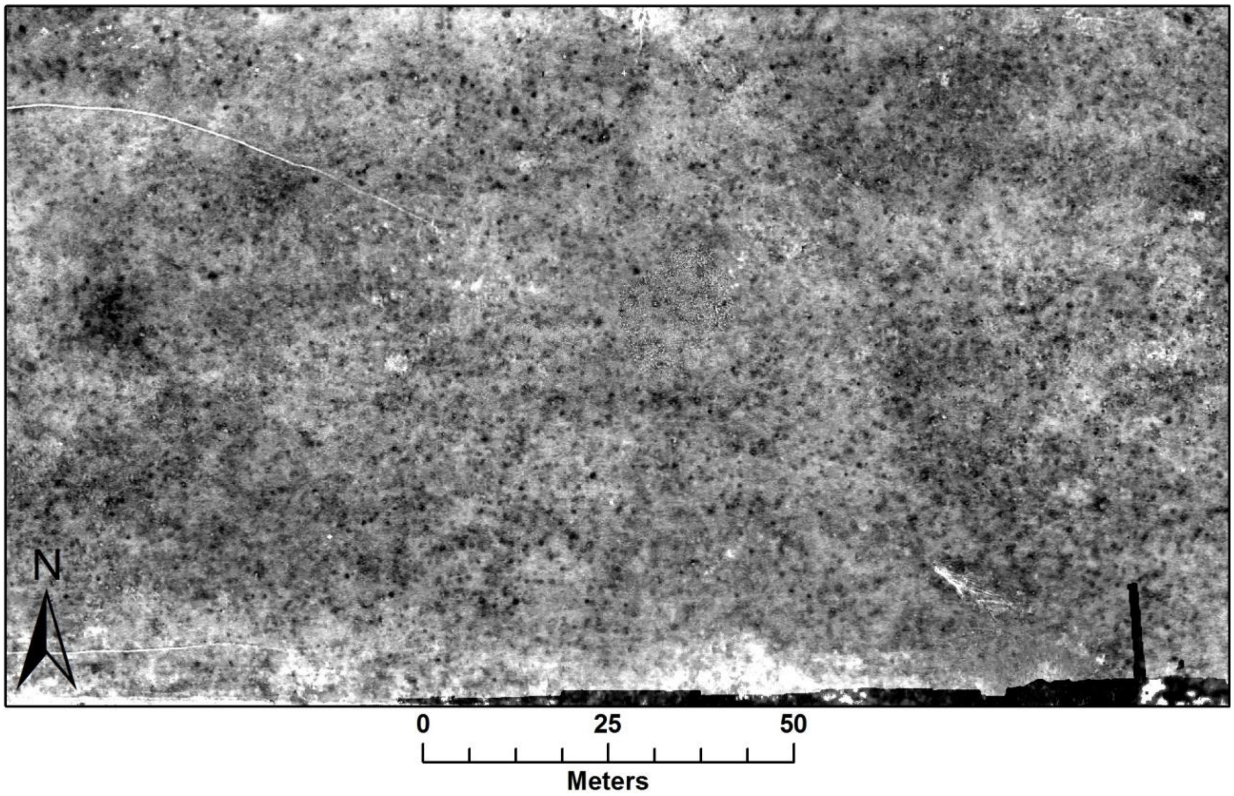

Figure 27: Thermal – NDVI.

5.4. Results

Upon first glance at the final thermal-NDVI image, it is apparent that not all vegetation noise was removed. By comparing the final product to the thermal and NDVI images, we can see that some areas of noise were reduced while others actually became more prominent. Some of these flaws may have been potential derived from imperfectly georeferenced images. I had experienced some difficulty identifying GCPs in the thermal data. If any were inaccurately marked, this would have resulted in subtracting high-NDVI (thick vegetation) values from areas where there was in fact no vegetation, skewing the results. However, there is an alternative interpretation for these results.

The increase in noise is especially noticeable on top of Mound C. The original thermal image shows a dark, cool area in the center of the mound. The NDVI indicated a corresponding area of thick vegetation (Figure 28). Subtracting this high, healthy vegetation value from a relatively low thermal value has resulted in a very low value in the final Thermal-NDVI image that does not correspond to the actual thermal properties of the earth or archaeological features in that area. Instead of creating a true “sans vegetation” thermal image, the final image appears to work best as a map of cool, thickly vegetated areas.

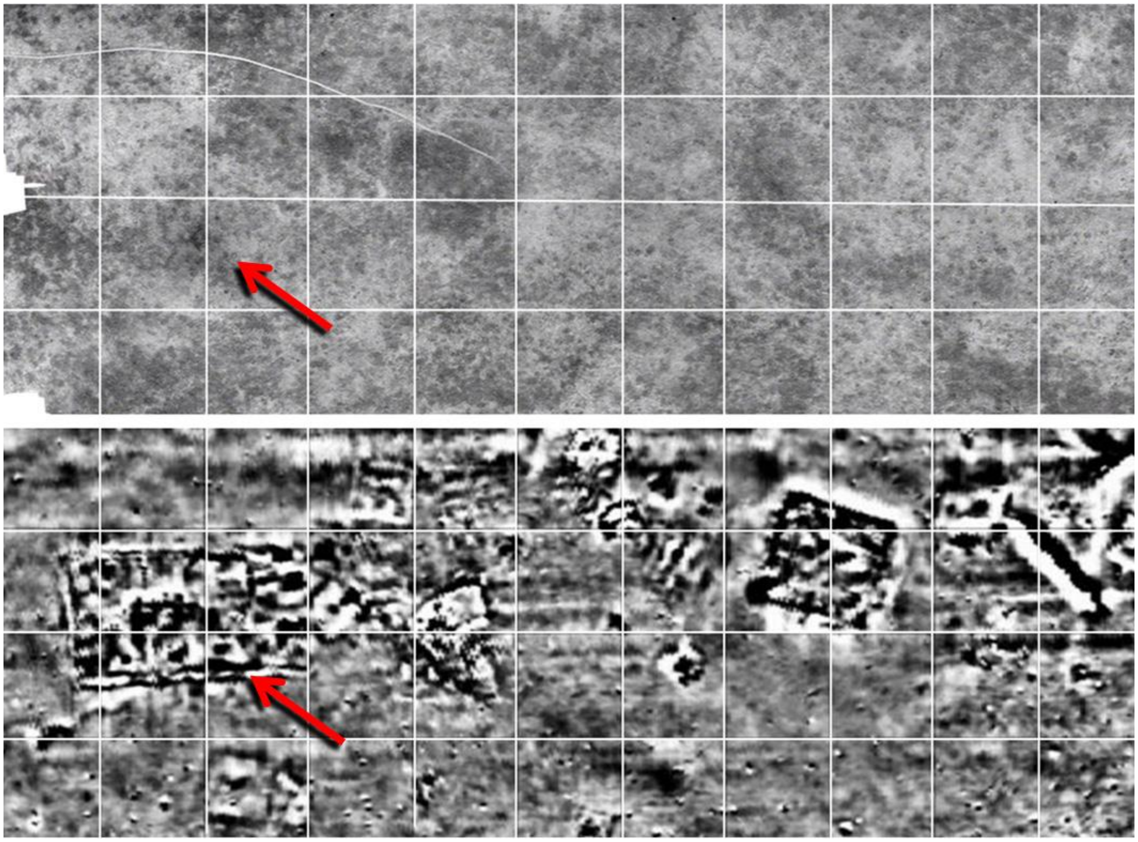

Figure 28: Thermal – NDVI image (top) compared to the magnetic gradiometry data (bottom). Red arrow indicates the feature at the top of Mound C (Magnetic data Sullivan and McKinnon 2013: 75; Grid alignment Stephanie Sullivan 2014).

While this map of cool vegetation does not directly or consistently indicate the presence of archaeology, it may be an effective way of discovering certain types of archaeological features. Ditches, packed floors, and storage pits are likely to collect water. The presence of water creates an environment where vegetation can flourish and lowers thermal inertia so that area remains cool throughout the day. This theory is supported by the presence of one of these cool, thickly vegetated areas over the location of a suspected charnel house on top of Mound C (Sullivan and McKinnon 2013: 75–76). Further testing of this method in sites known to contain features such as pit-houses could confirm this result.

6. Discussion

6.1. Experimental Plot

Based on the information gathered over the course of this limited experiment, some conclusions can be drawn regarding the appropriate and productive application of aerial thermography. Any area with very dense, moist soil, such as clay, is unlikely to produce clear thermal results. This type of matrix will block most thermal radiation from penetrating the surface and will also mask the responses of buried features. On the other hand, soils with low thermal inertia, such as sand or silt, are more likely than dense or moist soils to be amenable to thermal prospection. Areas with very dry climates such as the Near East and the American southwest would be excellent places for thermal prospection, especially if they are only sparsely vegetated, as illustrated by Casana et al. (2014). However, thermal prospection is limited to near-surface archaeology. This will reduce its usefulness in parts of the Near East where many features are buried under a meter or more of soil. Additionally, if common building materials share similar physical properties with their surrounding environment, even near-surface features may be difficult to detect.

The ideal time for thermal data collection is at night, several hours after diurnal heat flux has transitioned from positive to negative. In my data sets, the ideal time started halfway through the period of negative flux, approximately eight to ten hours after daytime temperature had peaked. While daytime thermograms had some minor success, they did not show any unique anomalies not already visible in the night images, and most anomalies were obscured by reflected radiation. The exact timing of this data collection will vary with the magnitude of diurnal flux, which depends on the season as well as short-term weather, and the thermal inertia properties of the background environment.

In my consideration of transient versus diurnal flux and their impact on the strength of thermal anomalies, I determined that the amplitude of the diurnal flux does not appear to affect the visibility of anomalies. Instead, diurnal flux is primarily useful for determining at what point during the day data collection should occur. I also showed that transient flux variations do not always reliably produce highly visible thermal anomalies. Thermal data collected two days after transient flux variation revealed no anomalies, but data collected only one day after flux variation had excellent results. This could indicate that the ideal time window for collecting thermal data is very narrow and must be carefully calculated, taking into account the amplitude of transient flux and temperature ranges preceding data collection. However, this line of reasoning is called into question by the mediocre thermogram collected after a week with no transient flux variations. Assuming flux variation determines the quality of thermal anomalies, this should have been the worst thermogram of the set, but it was not. Clearly transient flux variation is not the only factor to be considered. Another possibility is that a completely different variable, such as solar radiation, is the primary source for highly visible thermal anomalies. These possibilities require further investigation, but should not preclude the use of aerial thermography in current archaeological research. Productive data is still easily acquired, even if we have not yet pinpointed the ideal timing.

As UAV technology becomes more accessible, archaeological prospecting via aerial thermography will become even more efficient and inexpensive. There can be a steep learning curve for UAV piloting and some devices are prone to malfunction, as described by Casana et al. (2014). However, growing consumer demand for these vehicles is prompting manufacturers to develop more user-friendly and reliable versions, so I expect that these concerns will soon become negligible.

Although nighttime data collection is somewhat inconvenient it can hardly be described as labor-intensive or time-consuming, especially when compared to other archaeological prospecting methods. If one night has poor results, the entire process can be repeated again on the next night. Video feeds can be monitored live, as in the case of Poirier et al. (2013), to aid in on-the-spot decision making. Detailed processing can be done on a field computer or in the lab and has recently been drastically simplified by the use of automatic image stitching software such as AgiSoft PhotoScan or Microsoft ICE, as demonstrated by Casana et al. (2014) and in this research. With the combination of these two technologies and their success in recent thermal surveys in New Mexico (Casana et al: 2014) and at the Collins site in Arkansas (Chapter 5; Cool et al.: 2014), my certainty that aerial thermography can be a reliable and feasible archaeological prospecting method only continues to increase.

6.2. The Collins Site

Although unplanned for, the map of cool, vegetated areas created by subtracting the NDVI from the thermogram may actually be beneficial in archaeological prospecting. At least in this case study there is a definite correlation between dark areas of the thermal-NDVI image and areas containing archaeological features. We know from previous research that Mound C contains a large structure, probably a charnel house (Sullivan and McKinnon 2013: 75–76). The packed floor of this house may be trapping water above it. The high water content increases thermal inertia, creating a cool thermal anomaly while the rest of the soil begins to warm with the coming dawn. Additionally, this surplus of water creates an environment where vegetation can flourish. In a homogeneously-planted field, such a feature would likely have appeared as a distinct crop mark. In the patchy cow pasture of the Collins site, no easily identifiable crop marks were present. Adding this extra processing step allowed significant vegetation patterns to be identified. Further research into this and similar potential correlations is certainly worth exploring.

As encouraging as these results are for prospection in general, I have not reached my original goal of reducing vegetation noise in thermal images. By treating the NDVI as a proxy for vegetation-based thermal anomalies, I disregarded the fundamental fact that the NDVI measures chlorophyll content, not transpiration. Transpiration is the characteristic that determines the thermal properties of plants. While it seems reasonable that there is a connection between the chlorophyll content of healthy vegetation and their rate of transpiration, it is unlikely to be a one-to-one relationship. Furthermore, thermal vegetation noise may manifest as either an increase or a decrease to the thermal signatures of the background environment depending on the time of day in which the data is collected as well as the properties of the soil matrix. In the thermograms of my experimental plot, the vegetation growing alongside appears cooler than the bare soil during the day and warmer at night.

While the NDVI works as an excellent method for mapping the location of vegetation, it does not provide sufficient information for the removal of thermal vegetation noise. We must find a means of measuring or calculating the thermal properties of plants directly. We must also take into account the time at which thermal images are collected to ensure that processing will reduce and not increase this issue. If we subtract values from thermal data where vegetation is having a cooling effect, we will only increase the noise. We must identify when plants are relatively warm or cool in each environment and learn to quantify their impact before they can be effectively removed.

6.3. Future Directions

My goal has been to provide some general guidelines for archaeologists interested in adding aerial thermography to their toolbox and to set the stage for future investigations into thermal prospecting. I only considered a small handful of variables in this preliminary research, and I am unlikely to exhaust new lines of inquiry any time in the near future.

In further research I hope to expand my study by creating a larger experimental plot that incorporates more variables, such as additional features, soil types, and ground cover. Ideally I would like to spend at least a year collecting data to observe how thermal responses change with the seasons. This would also allow time for gathering enough data to conduct meaningful statistical analyses relating factors such as soil moisture, solar radiation, and diurnal and transient flux variations to the manifestation of anthropogenic thermal anomalies. Furthermore, I am interested in exploring the relationship between transpiration and the thermal properties of plants. This may help me to derive a more accurate method or algorithm for reducing vegetation noise.

Throughout this study technical issues such as low-quality batteries, too few ground control points, and my unstable picavet suspension system created persistent problems that reduced data quality. While I resolved many of these issues during the course of research, for future experimental plot-based data collection I plan to establish a permanent, stable recording station. This would increase the consistency and quality between thermograms. If possible, this recording platform will have a permanent supply of electricity so that the thermal camera can be left running for extended periods. The ability to gather thermal data over the course of a full day would be a significant asset when attempting to pinpoint the precise times for obtaining maximum results.

A few of the quality issues I encountered can be attributed to the innate limitations of current thermal imaging technology. The primary such challenges I experienced were due to the low bit-rate of the recording device and the auto-calibration feature of the thermal camera. The low bit-rate resulted in low-resolution images. This can make identifying smaller features or less intense anomalies impossible to identify due to insufficient contrast for visual analysis. The low resolution also reduces the ability of photo-stitching programs such as AgiSoft PhotoScan and Microsoft ICE to mosaic individual frames as common points between images are difficult to distinguish. The use of a DVR with a higher bit-rate will improve the resolution problem. Even a small increase in radiometric resolution from 8-bit to 16-bit will increase the number of distinct values from 256 to 65,536. This will drastically improve visualization and alignment.

The challenges I encountered while attempting to mosaic images were further exacerbated by the auto-calibration feature of the thermal camera. This feature constantly shifted the relative grayscale so that identical shades of gray did not represent identical temperature values between frames. There are several possible ways to address this problem. It may be possible to run a histogram equalization process on each individual frame before mosaicking to match their grayscale ranges, but this could result in the loss of outlier information and a reduction in already-low resolution. Another solution is to record the entire site within a single frame instead of in overlapping transects. This would ensure that a single visual scale is used for the entire site; however, data would have to be recorded from a much higher altitude to fit the entire site within a single frame, which would result in the loss of ground resolution. I believe the ideal solution would be a camera setting that allows the user to calibrate it once at the beginning of a recording session and then maintain that setting for the duration of data collection. This is, of course, up to the thermal camera manufacturers to implement, so we must make sure that we are providing them with regular feedback to encourage such developments.

UAV technology also comes with a set of technological challenges and limitations. UAVs still have a fairly steep learning curve and occasional tendency to malfunction. Inexperienced archaeologists may feel hesitant to load them with several thousand dollars' worth of equipment. I myself did not feel comfortable piloting a UAV alone and simply monitored the flight telemetry while my more experienced colleagues took the wheel. Thankfully, these issues are easily resolved. Would-be pilots can be trained by practicing with $20 miniature UAVs to hone their skills and gain confidence before conducting fieldwork. In addition, UAVs are becoming more reliable and user-friendly every day as consumer demand continues to soar. Soon aerial thermography will be listed among the most feasible and reliable forms of prospection for all archaeologists.

References

Abrams, M, and D.C. Comer
2013 Multispectral and Hyperspectral Technology and ARchaeological Applications. *In* Mapping Archaeological Landscapes from Space. D.C. Comer and M.J. Harrower, eds. Pp. 57–71. New York: Springer.

AgiSoft PhotoScan User Manual: Professional Edition, Version 1.0.0
2013. AgiSoft LLC.

Barnes, Adam
2013 Nikon D200 IR. Geospatial Modeling & Visualization. http://gmv.cast.uark.edu/photogrammetry/photogrammetry-hardware/nikon-d200-ir/, accessed March 27, 2015.

Bellerby, T.J., M. Noel, and K. Branigan
1990 A Thermal Method for Archaeological Prospection: Preliminary Investigations. Archaeometry 32(2): 191–203.

Berlin, G.L., J.R. Ambler, R.H. Hevly, and G.G. Schaber
1977 Identification of a Sinagua Agricultural Field by Aerial Thermography, Soil Chemistry, Pollen/Plant Analysis, and Archaeology. American Antiquity 42(4): 588–600.

Braasch, O.
1983 Luftbildarchäologie in Süddeutschland. Wurttemberg und Hohenzollern eV: Gesellschaft fur Vor-und Friihgeschichte.

Buck, P.E., D.E. Sabol, and A.R. Gillespie
2003 Sub-Pixel Artifact Detection Using Remote Sensing. Journal of Archaeological Science 30(8): 973–989.

Casana, J., J. Kantner, A. Wiewel, and J. Cothren
2014 Archaeological Aerial Thermography: A Case Study at the Chaco-Era Blue J Community, New Mexico. Journal of Archaeological Science 45: 207–219.

Cool, A.C., A. Wiewel, and S.M. Sullivan
2014 UAV-Based Aerial Thermography at the Collins Mounds Archaeological Site, Arkansas. Paper presented at the DRS Technologies Student Infrared Imaging Competition, Melbourne, Florida, June 28.

Crawford, O. G. S.
1923 Air Survey and Archæology. The Geographical Journal 61(5): 342–360.

Danese, M., U. Demšar, N. Masini, and M. Charlton
2010 Investigating Material Decay of Historic Buildings Using Visual Analytics with Multi-Temporal Infrared Thermographic Data. Archaeometry 52(3): 482–501.

Delta-T Devices
2015 SM150 Soil Moisture Sensor. Delta-T Devices. http://www.delta-t.co.uk/product-display.asp?id=SM150%20Product&div=Irrigation%20and%20Horticulture, accessed March 2, 2015.

Digital Camera Setup
2013 West Lothian Archaeology. http://www.armadale.org.uk/kitebasic.htm, accessed November 16, 2014.

Dockrill, S. J., J. M. Bond, J. Crummett, and C. P. Heron
1995 Scatness, Shetland: An Integrated Survey of a Multiperiod Settlement Mound. Archaeological Prospection 2(3): 141–154.

Ben-Dor, E., J. Portugali, M. Kochavi, M. Shimoni, and L. Vinitzky
1999 Airborne Thermal Video Radiometry and Excavation Planning at Tel Leviah, Golan Heights, Israel. Journal of Field Archaeology 26(2): 117–127.

FLIR Systems
2015 Tau 2 LWIR Camera Cores - Specifications. FLIR Systems, Inc. http://www.flir.com/cvs/cores/view/?id=54717&collectionid=612&col=54726, accessed March 2, 2015.

Gaffney, C, and J Gater
2010 Revealing the Buried Past: Geophysics for Archaeologists. Gloucestershire: The History Press.

Giardino, M., and B.S. Haley
2006 Airborne Remote Sensing and Geospatial Analysis. *In* Remote Sensing in Archaeology: An Explicitly North American Perspective. J. Johnson, ed. Pp. 47–77. Tuscaloosa: University of Alabama Press.

Glagla, P.
2010 Download ImageGrab. Paul Glagla’s Fine Contributions. http://paul.glagla.free.fr/imagegrab_en.htm, accessed April 25, 2014.

Haley, B., J. Johnson, and R. Stallings
2002 The Utility of Low Cost Thermal Sensors in Archaeological Research. Report Prepared for the Office of Naval Research NASA Grant NAG5-7671. Center for Archaeological Research, University of Mississippi.

Hodder, I.
2006 Çatalhöyük: The Leopards Tale: Revealing the Mysteries of Turkey’s Ancient “town.” London: Thames and Hudson.

Kay, M., G. Sabo III, and R. Merletti

1989 Late Prehistoric Settlement Patterning: A View from Three Caddoan Civic-Ceremonial Centers in Northwest Arkansas. *In* Contributions to Spiro Archaeology: Mound Excavations and Regional Perspectives. J.D. Rogers, D.G. Wyckoff, and D.A. Peterson, eds. Pp. 129–157. Studies in Oklahoma's Past, 16. Norman: Oklahoma Archeological Survey.

Kvamme, K.L.
2003 Geophysical Surveys as Landscape Archaeology. American Antiquity 68(3): 435.
2006 Integrating Multidimensional Geophysical Data. Archaeological Prospection 13: 57–72.
2008a Archaeological Prospecting at the Double Ditch State Historic Site, North Dakota, USA. Archaeological Prospection 15: 62–79.
2008b Remote Sensing Approaches to Archaeological Reasoning: Pattern Recognition and Physical Principles. *In* Archaeological Concepts for the Study of the Cultural Past. A.P. Sullivan III, ed. Pp. 65–84. Salt Lake City: University of Utah Press.

Landsat: A Global Land-Imaging Mission
2013. USGS. http://pubs.usgs.gov/fs/2012/3072/, accessed February 13, 2015.

Leisz, S.J.
2013 An Overview of the Application of Remote Sensing to Archaeology During the Twentieth Century. *In* Mapping Archaeological Landscapes from Space. D.C. Comer and M.J. Harrower, eds. Pp. 11–19. New York: Springer.

Lundén, B.
1985 Aerial Thermography: A Remote Sensing Technique Applied to Detection of Buried Archaeological Remains at a Site in Dalecarlia, Sweden. Geografiska Annaler. Series A, Physical Geography 67(1/2): 161–166.

Magnani, Matthew
2014 Three-Dimensional Alternatives to Lithic Illustration. Advances in Archaeological Practice 2(4): 285–297.

Mehta, A.
2011 Introduction to the Electromagnetic Spectrum and Spectroscopy. http://pharmaxchange.info/press/2011/08/introduction-to-the-electromagnetic-spectrum-and-spectroscopy/, accessed February 13, 2015.

MiniTemp: Portable Infrared Thermometer
2004. RayTek Corporation. www.raytek.com.

Neubauer, W.
2004 GIS in Archaeology—the Interface between Prospection and Excavation. Archaeological Prospection 11(3): 159–166.

Orion StarShoot LCD-DVR
2015 Orion Telescopes & Binoculars.

http://www.telescope.com/Astrophotography/Astrophotography-Accessories/Orion-StarShoot-LCD-DVR/c/4/sc/61/p/101876.uts, accessed February 26, 2015.

Périsset, M.C.
1980 Prospection Thermique de Subsurfaces: Application À Archéologie.

Périsset, M.C., and A. Tabbagh
1981 Interpretation of Thermal Prospection on Bare Soils. Archaeometry 23(2): 169–187.

Poirier, N., F. Hautefeuille, and C. Calastrenc
2013 Low Altitude Thermal Survey by Means of an Automated Unmanned Aerial Vehicle for the Detection of Archaeological Buried Structures. Archaeological Prospection 20: 303–307.

redIRIS Infrared Inspections
2009 What Is Infrared? Seeing the World in a Different Light & Hearing Your Concerns. http://www.rediris.ca/infrared.html, accessed March 27, 2015.

Sabol, D.E., J.B. Adams, and M.O. Smith
1992 Quantitative Sub-Pixel Sprectral Detection of Targets in Multispectral Images. Journal of Geophysical Research 97(E2): 2659–2672.

Schaber, G.G., and G.J. Gumerman
1969 Infrared Scanning Images: An Archeological Application. Science 164(3880). New Series: 712–713.

Science Mission Directorate
2010 Infrared Waves. National Aeronautics and Space Administration. http://missionscience.nasa.gov/ems/07_infraredwaves.html, accessed February 24, 2014.

Scollar, I., A. Tabbagh, A. Hesse, and I. Herzog
1990 Archaeological Prospecting and Remote Sensing. Topics in Remote Sensing, 2. New York: Cambridge University Press.

Stanjek, H., and J.W.E. Faßbinder
1995 Soil Aspects Affecting Archaeological Details in Aerial Photographs. Archaeological Prospection 2: 91–101.

Stone Descriptions & Specs
2013 Schwartz Stone Company. http://www.schwartzstone.com/stone-descriptions-specs, accessed March 1, 2015.

Sullivan, S.M., and D.P. McKinnon
2013 The Collins Site (3WA1): Exploring Architectural Variation in the Western Ozark Highlands. Southeastern Archaeology 32(1): 70–84.

Tabbagh, A.

1977 Sur La Détermination Du Moment de Mesure Favorable et L'interprétation Des Résultats En Prospection Thermique Archéologique. *In* Annales de Géophysique Pp. 243–253.

1979 Prospection Thermique Aéroportée Du Site de Prepou. Revue d'Archaeometrie 7: 11–25.

The Weather Channel, LLC.

2015 Weather Underground. www.wunderground.com.

University of Arkansas DRS 2014 Thermal Imaging Competition Entry

2014. https://youtu.be/Pjh0UO3_OqY.

Verhoeven, Geert

2011 Taking Computer Vision Aloft – Archaeological Three-Dimensional Reconstructions from Aerial Photographs with Photoscan. Archaeological Prospection 18(1): 67–73.

Vogel, G.

2005 A View from the Bottomlands: Physical and Social Landscapes and Prehistoric Mound Centers in the Northern Caddo Area. Unpublished Ph.D. dissertation, University of Arkansas.

Weier, J., and D. Herring

2000 Measuring Vegetation (NDVI & EVI). Text Article. NASA Earth Observatory. http://earthobservatory.nasa.gov/Features/MeasuringVegetation/, accessed March 26, 2015.

Wheatley, D., and M. Gillings

2002 Spatial Technology and Archaeology: The Archaeological Applications of GIS. London: Taylor & Francis.

Appendix A: Experimental Plot Data Collection Times and Temperature

Data from National Weather Service Station KFYV (The Weather Channel, LLC. 2015).

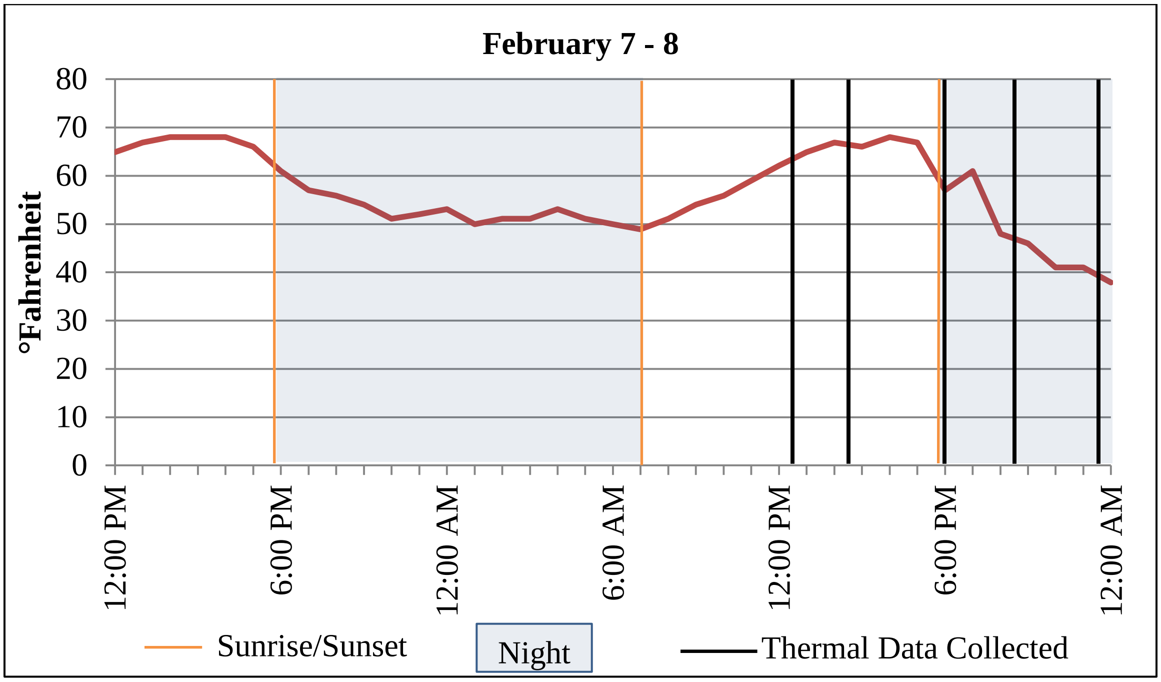

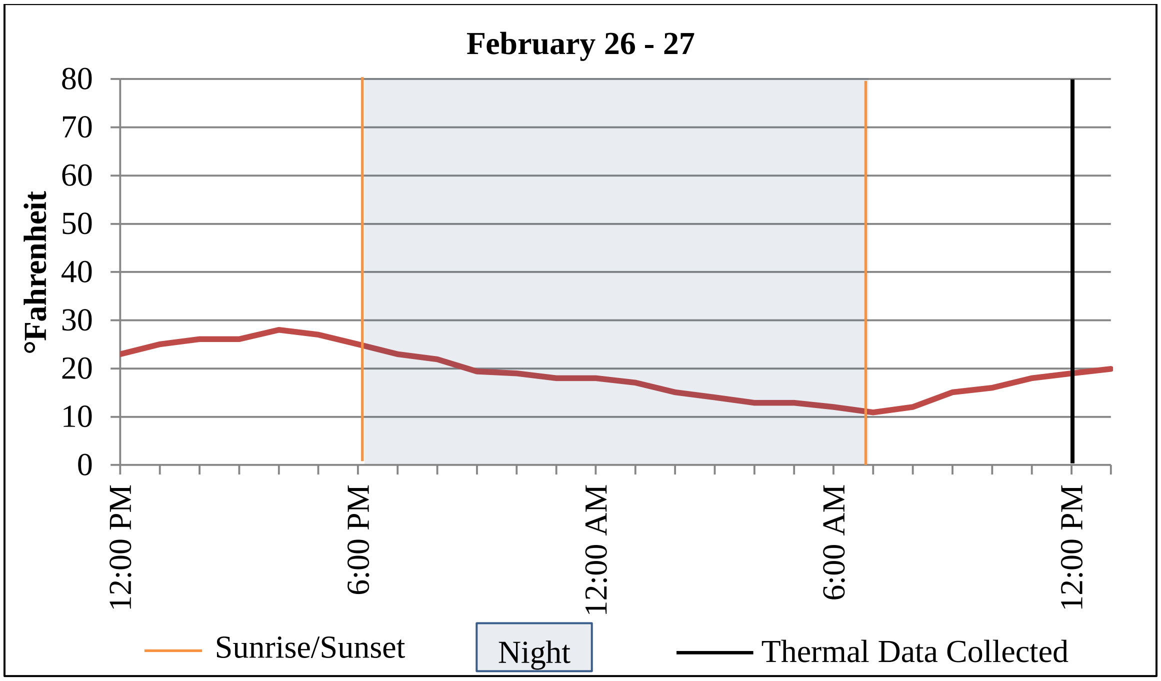

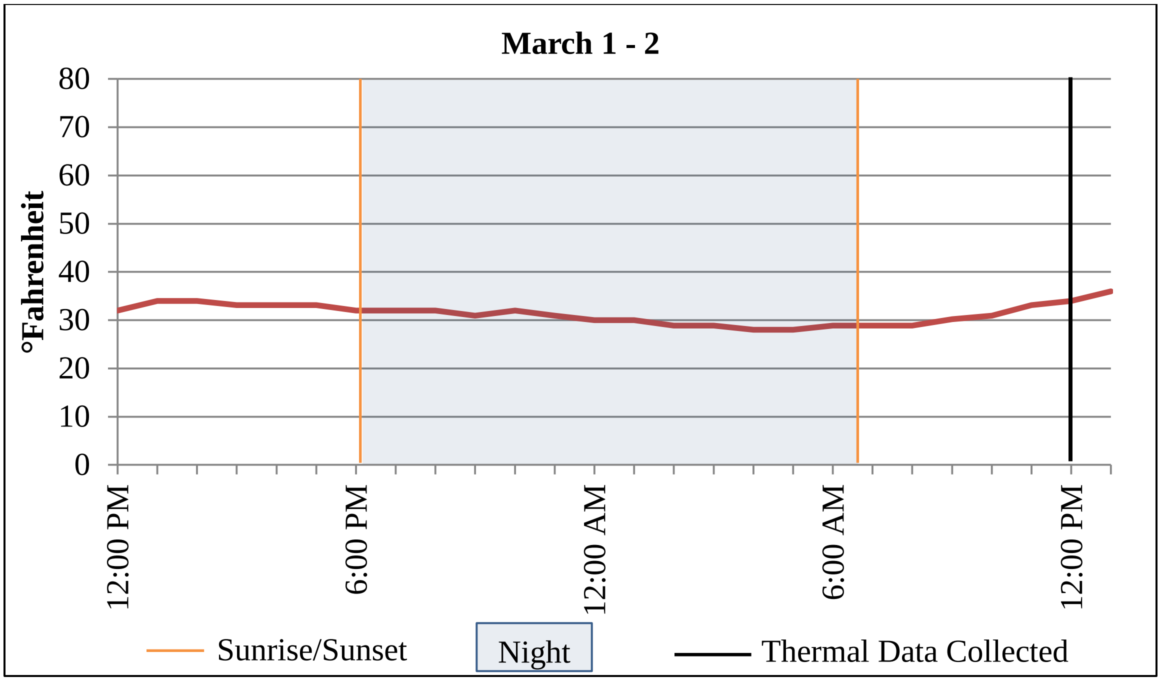
March 1 - 2
°Fahrenheit
80
70
60
50
40
30
20
10
0
12:00 PM
6:00 PM
12:00 AM
6:00 AM
12:00 PM
Sunrise/Sunset
Night
Thermal Data Collected

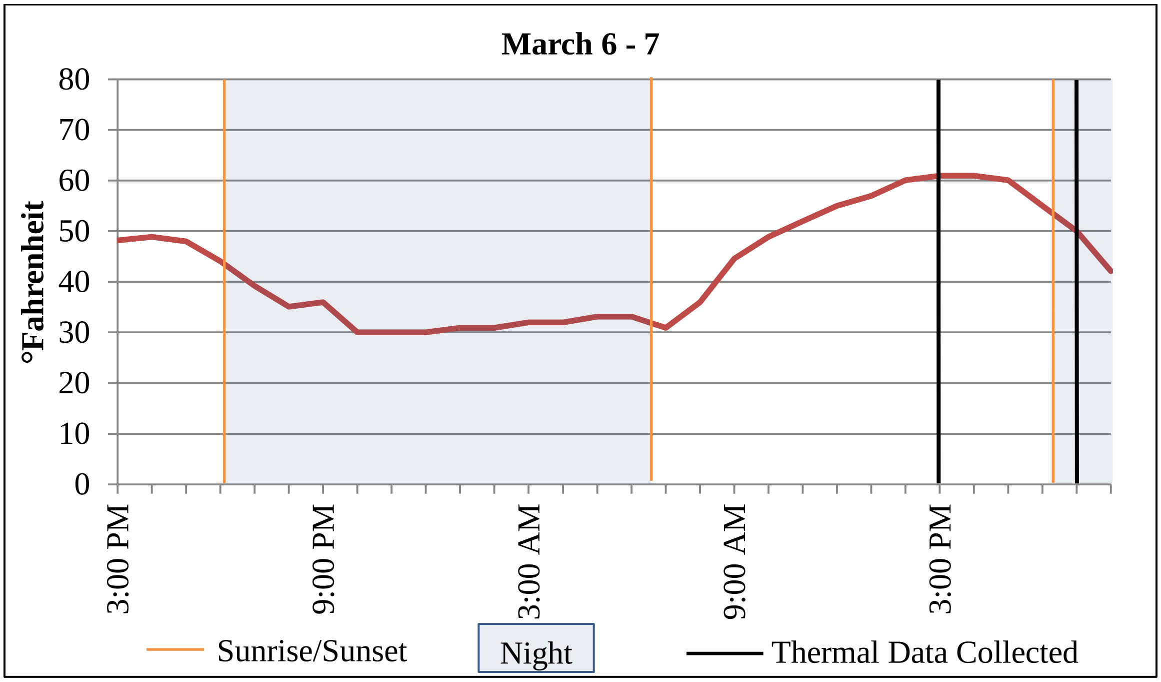
March 6 - 7
°Fahrenheit
80
70
60
50
40
30
20
10
0
3:00 PM
9:00 PM
3:00 AM
9:00 AM
3:00 PM
Sunrise/Sunset
Night
Thermal Data Collected

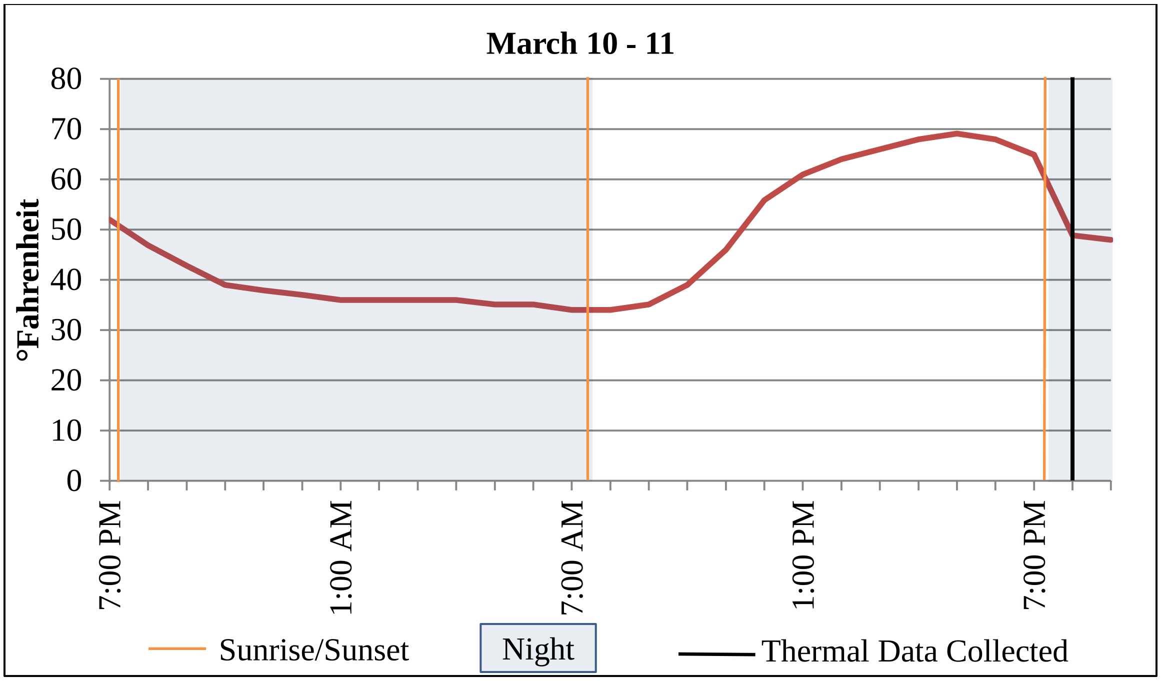
March 10 - 11
°Fahrenheit
80
70
60
50
40
30
20
10
0
7:00 PM
1:00 AM
7:00 AM
1:00 PM
7:00 PM
Sunrise/Sunset
Night
Thermal Data Collected

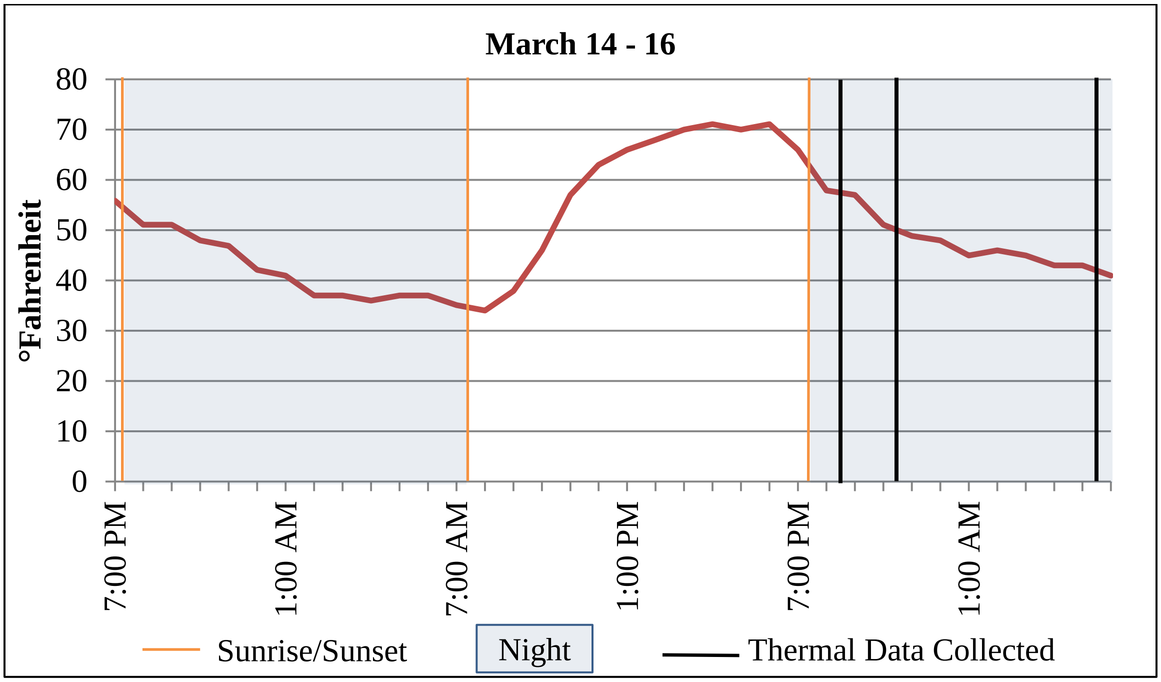
March 14 - 16
°Fahrenheit
80
70
60
50
40
30
20
10
0
7:00 PM
1:00 AM
7:00 AM
1:00 PM
7:00 PM
1:00 AM
Sunrise/Sunset
Night
Thermal Data Collected

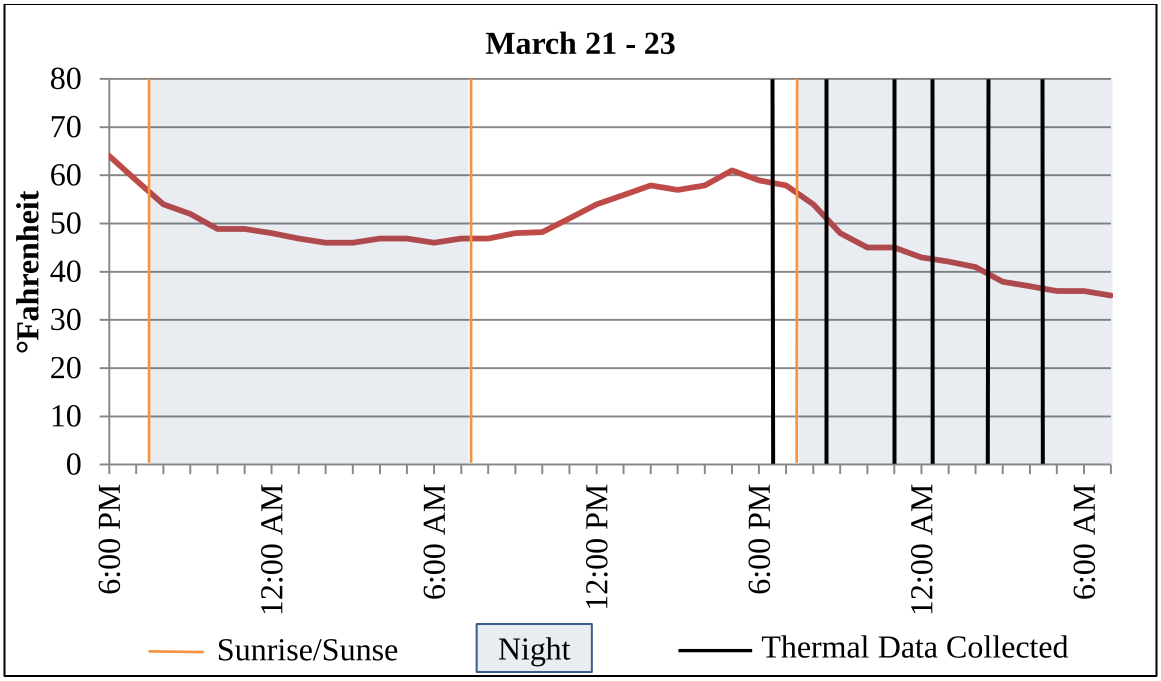
March 21 - 23
°Fahrenheit
80
70
60
50
40
30
20
10
0
6:00 PM
12:00 AM
6:00 AM
12:00 PM
6:00 PM
12:00 AM
6:00 AM
Sunrise/Sunse
Night
Thermal Data Collected

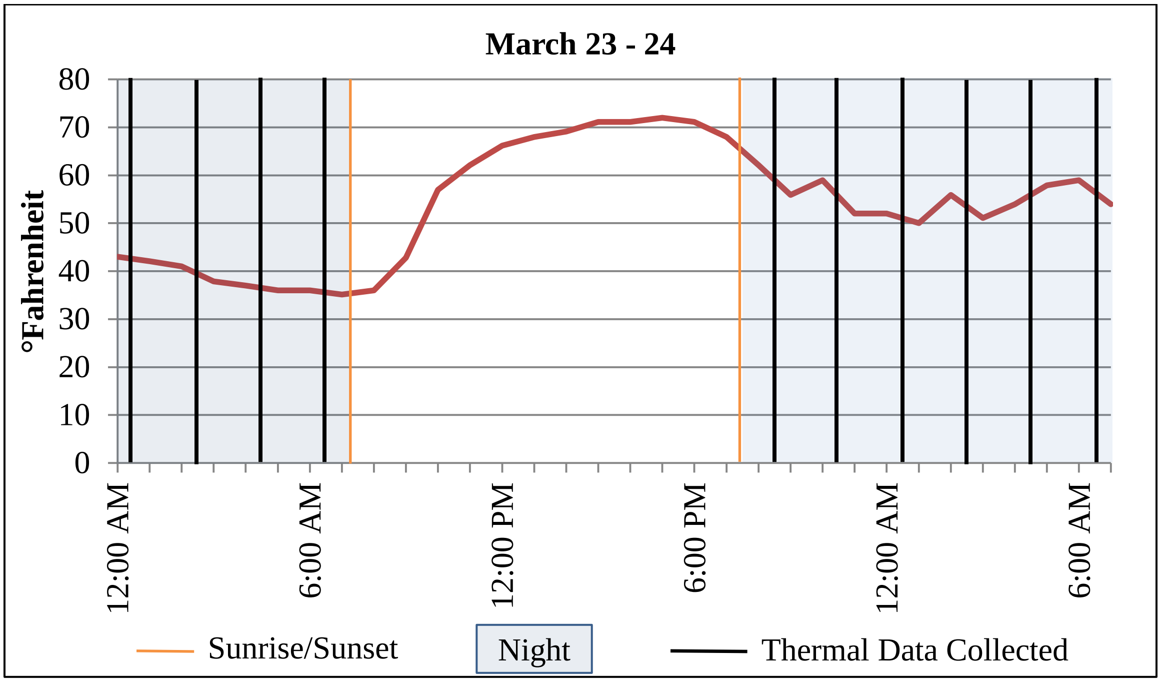
March 23 - 24
°Fahrenheit
80
70
60
50
40
30
20
10
0
12:00 AM
6:00 AM
12:00 PM
6:00 PM
12:00 AM
6:00 AM
Sunrise/Sunset
Night
Thermal Data Collected

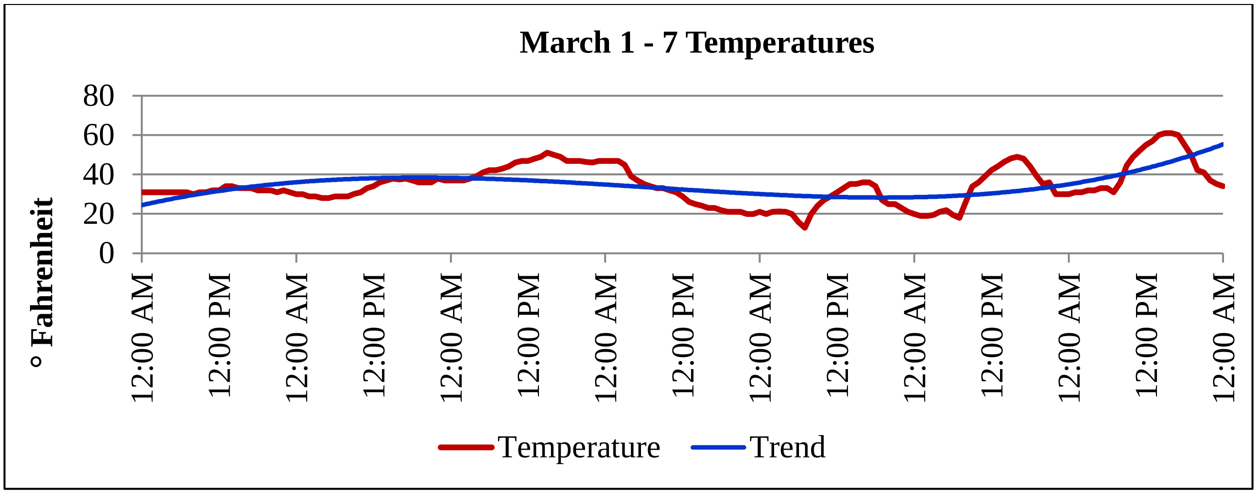
March 1 - 7 Temperatures
80
60
40
20
0
° Fahrenheit
12:00 AM
12:00 PM
12:00 AM
12:00 PM
12:00 AM
12:00 PM
12:00 AM
12:00 PM
12:00 AM
12:00 PM
12:00 AM
12:00 PM
12:00 AM
12:00 PM
12:00 AM
Temperature
Trend

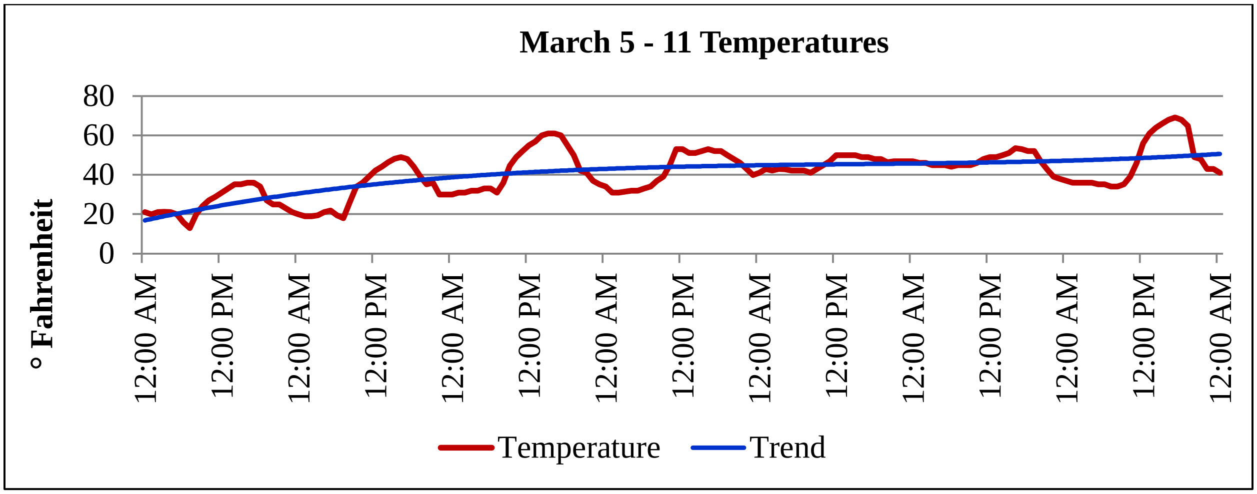
March 5 - 11 Temperatures
80
60
40
20
0
° Fahrenheit
12:00 AM
12:00 PM
12:00 AM
12:00 PM
12:00 AM
12:00 PM
12:00 AM
12:00 PM
12:00 AM
12:00 PM
12:00 AM
12:00 PM
12:00 AM
12:00 PM
12:00 AM
Temperature
Trend

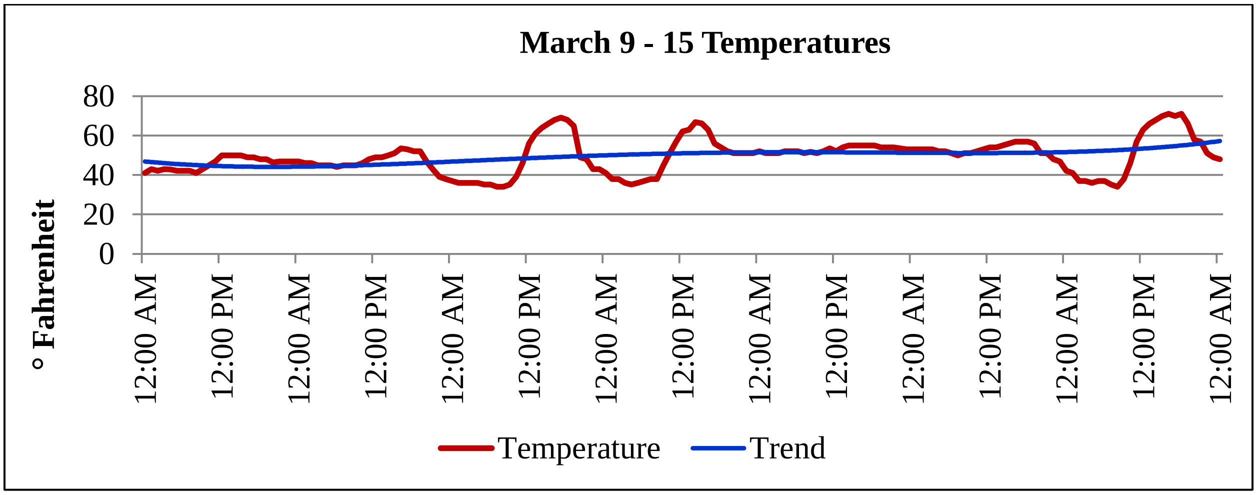
March 9 - 15 Temperatures
80
60
40
20
0
° Fahrenheit
12:00 AM
12:00 PM
12:00 AM
12:00 PM
12:00 AM
12:00 PM
12:00 AM
12:00 PM
12:00 AM
12:00 PM
12:00 AM
12:00 PM
12:00 AM
12:00 PM
12:00 AM
Temperature
Trend

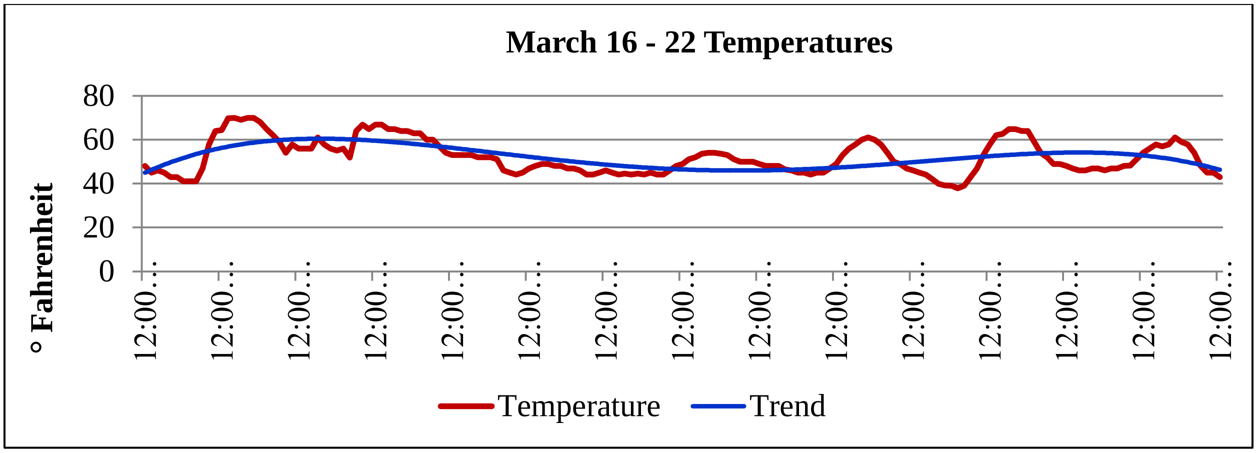
March 16 - 22 Temperatures
° Fahrenheit
80
60
40
20
0
12:00…
12:00…
12:00…
12:00…
12:00…
12:00…
12:00…
12:00…
12:00…
12:00…
12:00…
12:00…
12:00…
12:00…
12:00…
Temperature
Trend

Appendix B: Experimental Plot Conditions Summary

Date	Time	Weather	Air Temp ° F	Wind mph	Humidity %	Soil Temp Sand ° C	Soil Temp Clay ° C	Soil Moisture Sand % BV	Soil Moisture Clay % BV
2/8/2015	11:30 AM	Slightly Cloudy	59	10	69	19.0	15.2	4.9	25.5
2/8/2015	2:30 PM	Slightly Cloudy	67	9	48	24.8	18.6	4.7	21.3
2/8/2015	5:45 PM	Clear, indirect light	67	9	38	10.5	9.0	4.6	26.3
2/8/2015	8:30 PM	Night, clear skies	48	4	65	5.8	5.2	4.6	24.6
2/8/2015	11:30 PM	Night, clear skies	41	calm	85	2.3	1.8	3.7	24.6
2/9/2015	2:30 AM	Night, clear skies	36	4	92	0.7	-1.0	3.8	26.9
2/9/2015	5:30 AM	Night, clear skies	32	calm	95	-0.7	-1.0	4.5	26.1
2/9/2015	8:30 AM	Overcast	39	7	92	1.7	0.0	5.7	24.9
2/17/2015	2:30 PM	Overcast, snow 2cm deep	33	10	81	-10.3	-10.4	3.6	17.7
2/17/2015	6:30 PM	Overcast, sunset was 5:59	31	9	92	-8.8	-10.3	6.6	17.5
2/27/2015	12:00 PM	Overcast, some snow	19	8	49	-7.0	-10.3	1.2	6.0
3/2/2015	12:00 PM	Overcast, some snow	34	7	72	-1.3	-7.5	13.6	11.8
3/7/2015	3:00 PM	clear, sunny	61	6	34	22.5	14.2	6.6	36.0
3/7/2015	7:00 PM	clear, sunset 6:18	50	5	46	3.5	1.8	6.1	35.2
3/8/2015	9:00 PM	Night, partly cloudy, sunset 7:18	46	calm	70	2.5	1.5	5.1	34.7
3/8/2015	11:00 PM	Night, partly cloudy	40	calm	92	1.3	1.2	4.2	34.3
3/9/2015	7:00 AM	Night, cloudy, sunrise 7:36	42	calm	95	2.7	1.8	4.1	35.0
3/11/2015	8:00 PM	Night, sunny day	65	calm	37	10.2	8.0	6.5	35.7
3/12/2015	5:30 AM	Night, sunrise 7:32, cloudy	41	calm	84	2.3	2.0	6.4	35.8
3/15/2015	11:15 AM	Sunny, clear, last 2 days rainy	57	calm	58	24.7	19.3	9.1	38.5
3/15/2015	8:30 PM	Clear, sunset 7:23	58	7	74	11.5	10.7	7.8	36.4

Date	Time	Weather	Air Temp ° F	Wind mph	Humidity %	Soil Temp Sand ° C	Soil Temp Clay ° C	Soil Moisture Sand % BV	Soil Moisture Clay % BV
3/15/2015	11:30 PM	Clear	49	5	96	8.7	7.7	6.2	35.4
3/16/2015	5:30 AM	clear, sunrise 7:26	43	calm	86	4.5	4.5	5.7	36.2
3/22/2015	6:30 PM	Sunny, day cloudy	61	6	74	17.0	13.3	5.1	33.9
3/22/2015	8:30 PM	Sunset 7:29, clear	54	calm	86	8.8	8.5	5.2	32.7
3/22/2015	11:00 PM	clear	50	calm	99	6.5	5.7	5.1	32.2
3/23/2015	12:30 AM	clear	47	calm	99	6.0	5.3	6.3	35.3
3/23/2015	2:30 AM	Misty	43	calm	98	4.0	3.7	5.2	34.1
3/23/2015	4:30 AM	foggy	41	calm	99	2.2	2.3	4.7	33.8
3/23/2015	6:30 AM	Foggy, Sunrise 7:16	41	calm	99	1.2	1.7	4.7	34.8
3/23/2015	8:30 PM	Clear, sunset 7:30	66	calm	61	14.5	12.3	6.0	31.5
3/23/2015	10:30 PM	clear	62	calm	61	11.0	10.0	5.4	30.7
3/24/2015	12:30 AM	clear	59	2	70	10.3	8.7	4.9	30.8
3/24/2015	2:30 AM	partly cloudy	55	calm	76	7.8	7.5	4.3	31.6
3/24/2015	4:30 AM	partly cloudy	56	calm	73	10.0	8.5	4.6	31.6
3/24/2015	6:30 AM	overcast, Sunrise 7:14	57	calm	72	9.2	8.0	4.5	30.8
				Average:		6.7	4.9	5.4	29.7
				Standard Deviation:		8.29	7.35	1.94	7.41

Appendix C: Experimental Plot Results Summary

Thermal Metadata				Location of Visible Features							
Date	**Time**	**Video Quality**	**Thermogram Quality**	**Stone Shallow**	**Stone Deep**	**Brick Shallow**	**Brick Deep**	**Clay Berm**	**Ditch**	**Burned Stone**	**Burned Brick**
2/8/2015	11:30 AM	OK til 6:00	Fair								
2/8/2015	2:30 PM	Good	Good								
2/8/2015	5:45 PM	Good	Good			Sand					
2/8/2015	8:30 PM	OK til 3:45	Fair, only sand			sand					
2/8/2015	11:30 PM	fair	Fair, gap in sand			sand					
2/9/2015	2:30 AM	Poor	n/a								
2/9/2015	5:30 AM	Poor	n/a								
2/9/2015	8:30 AM	Poor	n/a								
2/17/2015	2:30 PM	Poor	n/a								
2/17/2015	6:30 PM	Poor	n/a								
2/27/2015	12:00 PM	Good	Fair, only sand			sand			sand		
3/2/2015	12:00 PM	Fair	Fair, only sand	sand		sand		sand	sand	sand	
3/7/2015	3:00 PM	Good	Good			sand			sand		
3/7/2015	7:00 PM	Good	Good								
3/8/2015	9:00 PM	Good	unusable								
3/8/2015	11:00 PM	fair-feet	unusable								
3/9/2015	7:00 AM	Poor-fogged?	n/a								
3/11/2015	8:00 PM	Good	Fair			sand			clay?	sand?	

Thermal Metadata				Location of Visible Features							
Date	**Time**	**Video Quality**	**Thermogram Quality**	**Stone Shallow**	**Stone Deep**	**Brick Shallow**	**Brick Deep**	**Clay Berm**	**Ditch**	**Burned Stone**	**Burned Brick**
3/12/2015	5:30 AM	fair	unusable								
3/15/2015	11:15 AM	Poor - didn't record?	n/a								
3/15/2015	8:30 PM	Good	Good			sand			clay?	sand?	
3/15/2015	11:30 PM	Good	Good			sand			both		
3/16/2015	5:30 AM	Good	Good			sand					
3/22/2015	6:30 PM	Good	Good			sand					
3/22/2015	8:30 PM	Good	Good			sand			clay	both	
3/22/2015	11:00 PM	Good	Good			sand			clay		
3/23/2015	12:30 AM	Good	Good			sand			both		
3/23/2015	2:30 AM	Good	Good			sand			both		
3/23/2015	4:30 AM	Good	Good			sand			both		
3/23/2015	6:30 AM	Good	Good			sand			both		
3/23/2015	8:30 PM	Good	Good			sand			both		
3/23/2015	10:30 PM	Good	Good			sand			both		
3/24/2015	12:30 AM	Fair	Good								
3/24/2015	2:30 AM	Good	Good			sand			both		
3/24/2015	4:30 AM	Fair	Fair								
3/24/2015	6:30 AM	Fair	Fair			sand					

Appendix D: Experimental Plot Thermograms

February 8 11:30 am

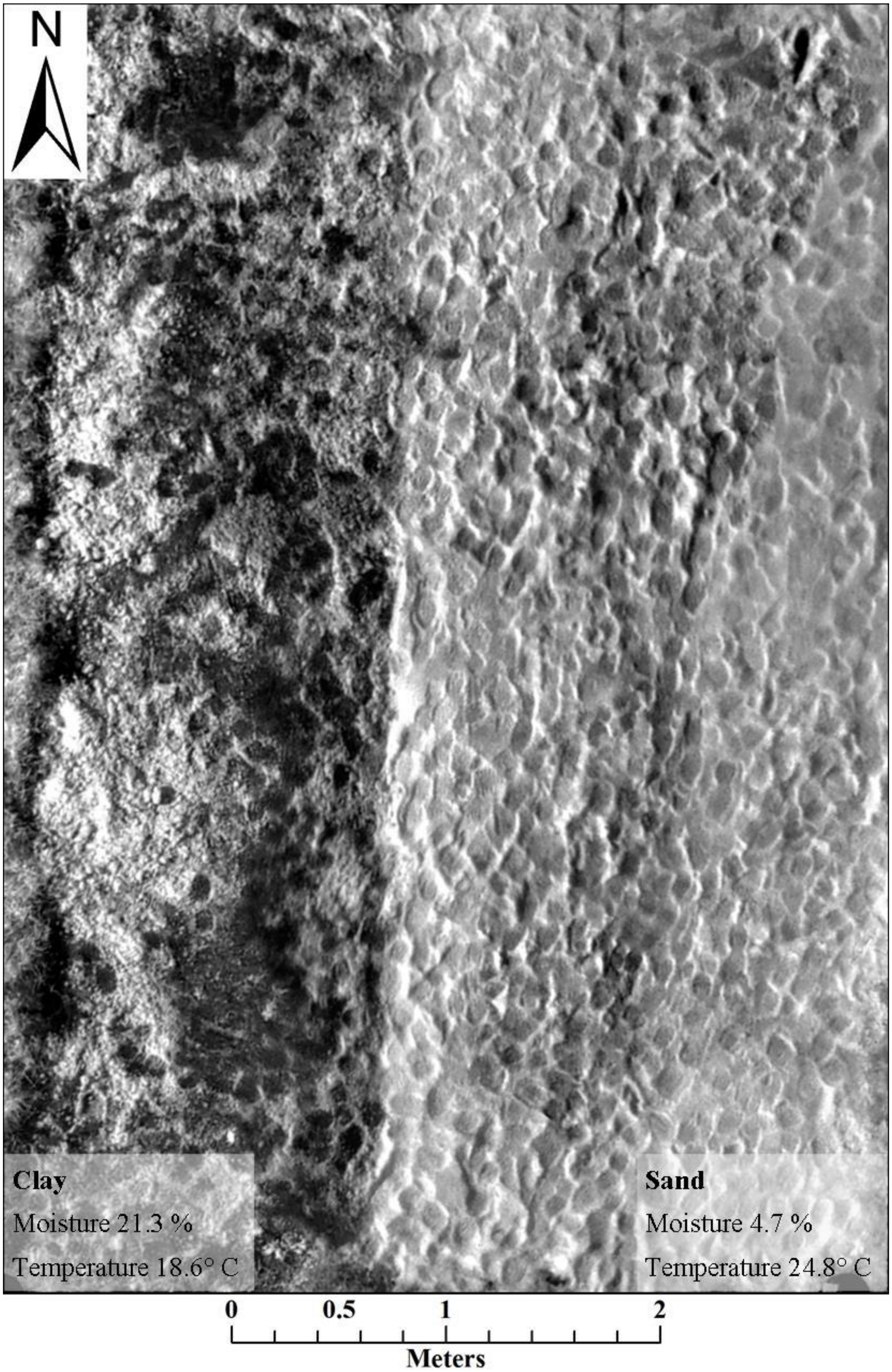

February 8 2:30 pm

February 8 6:00 pm

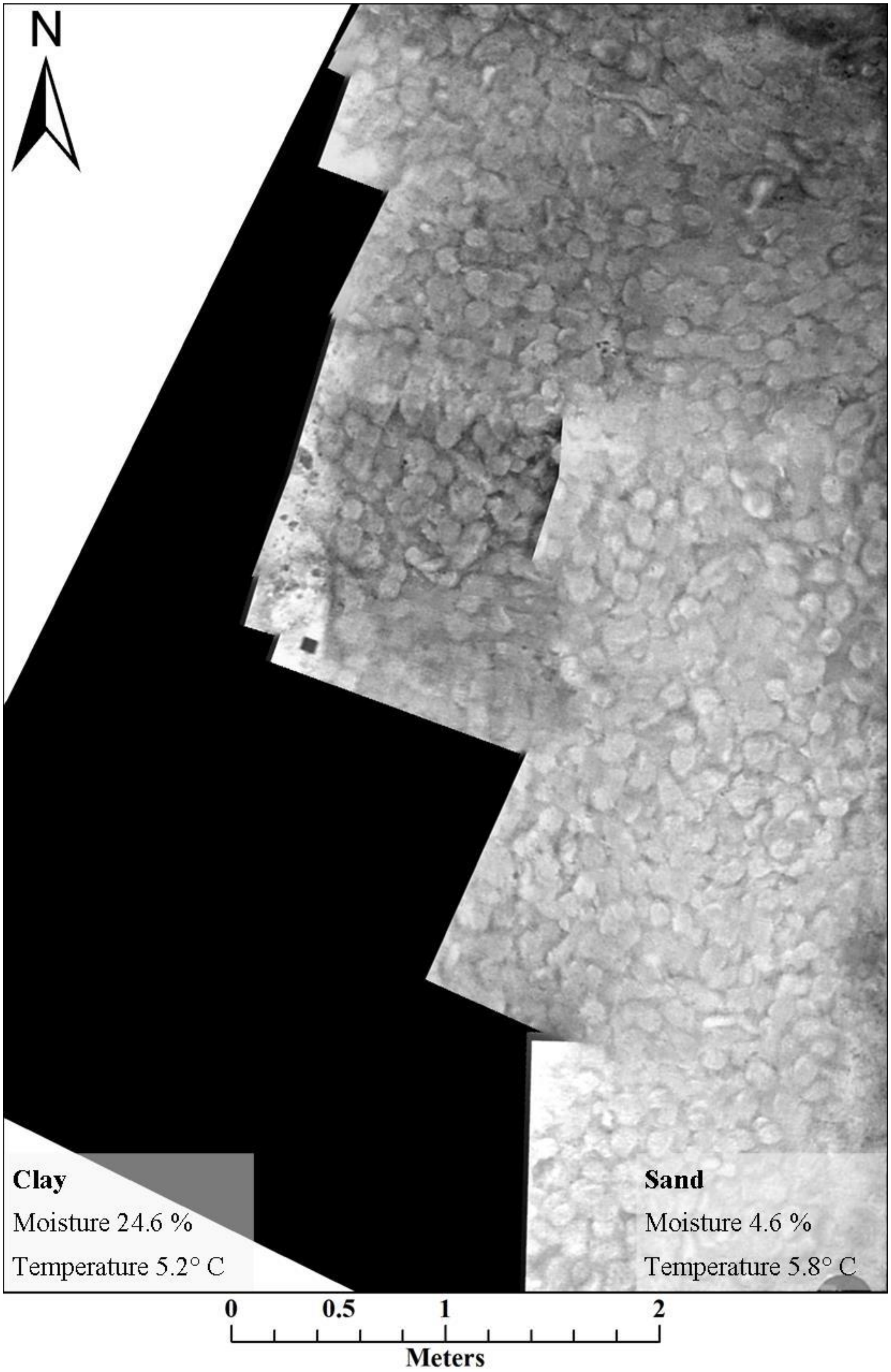

February 8 8:30 pm

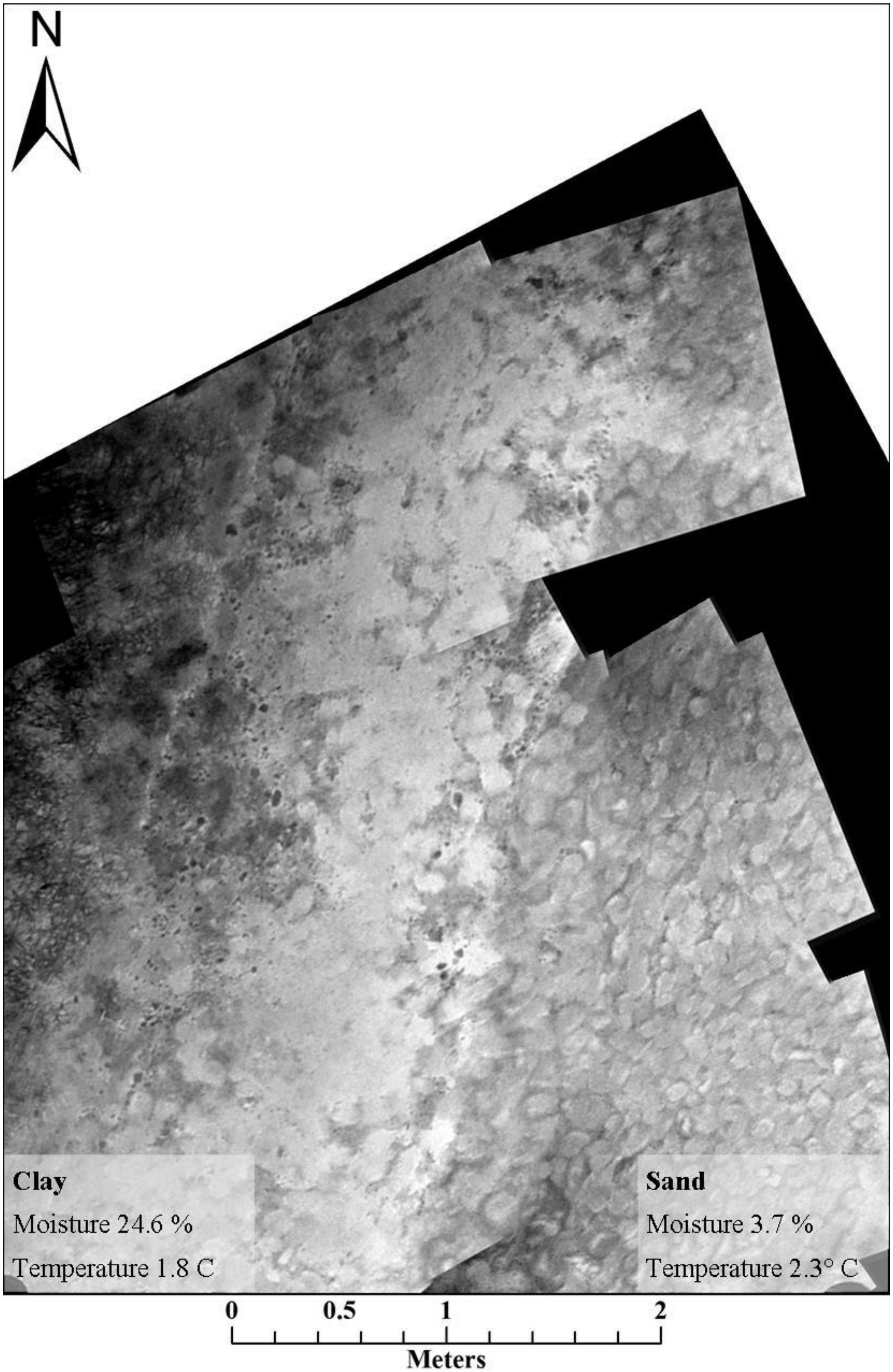

February 8 11:30 pm

February 27 12:00 pm

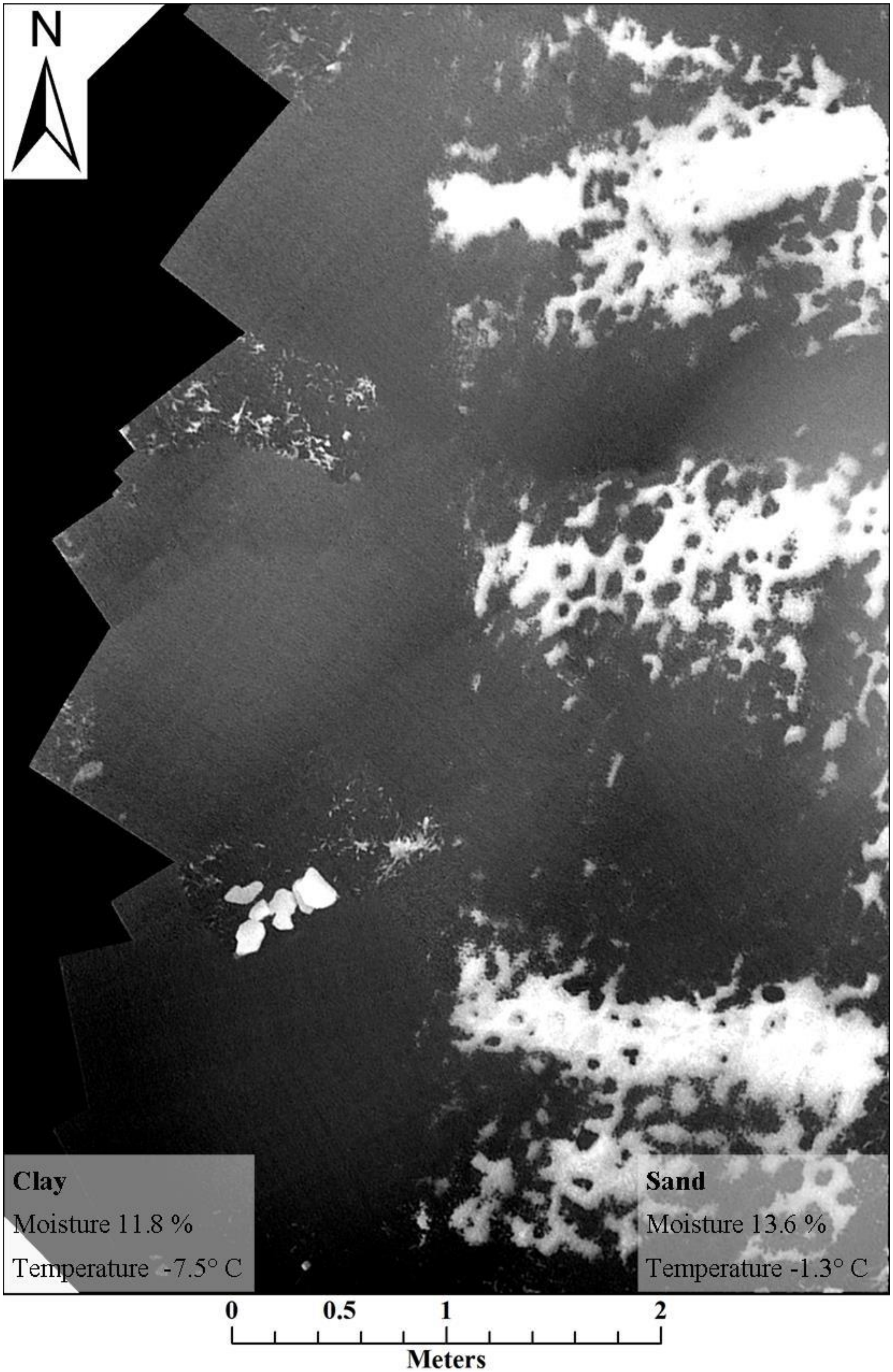

March 2 12:00 pm

March 7 3:00 pm

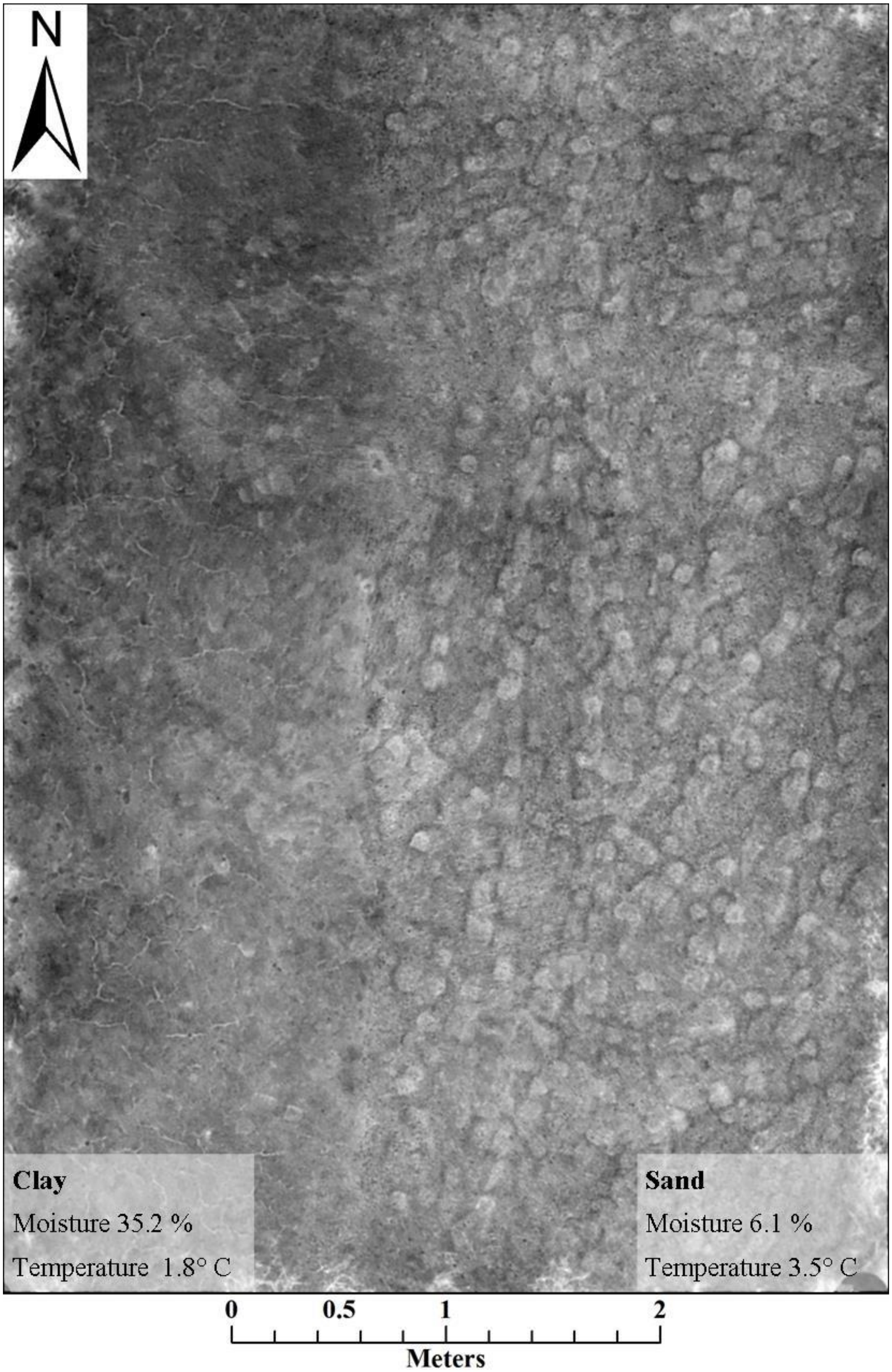

March 7 7:00 pm

March 11 8:00 pm

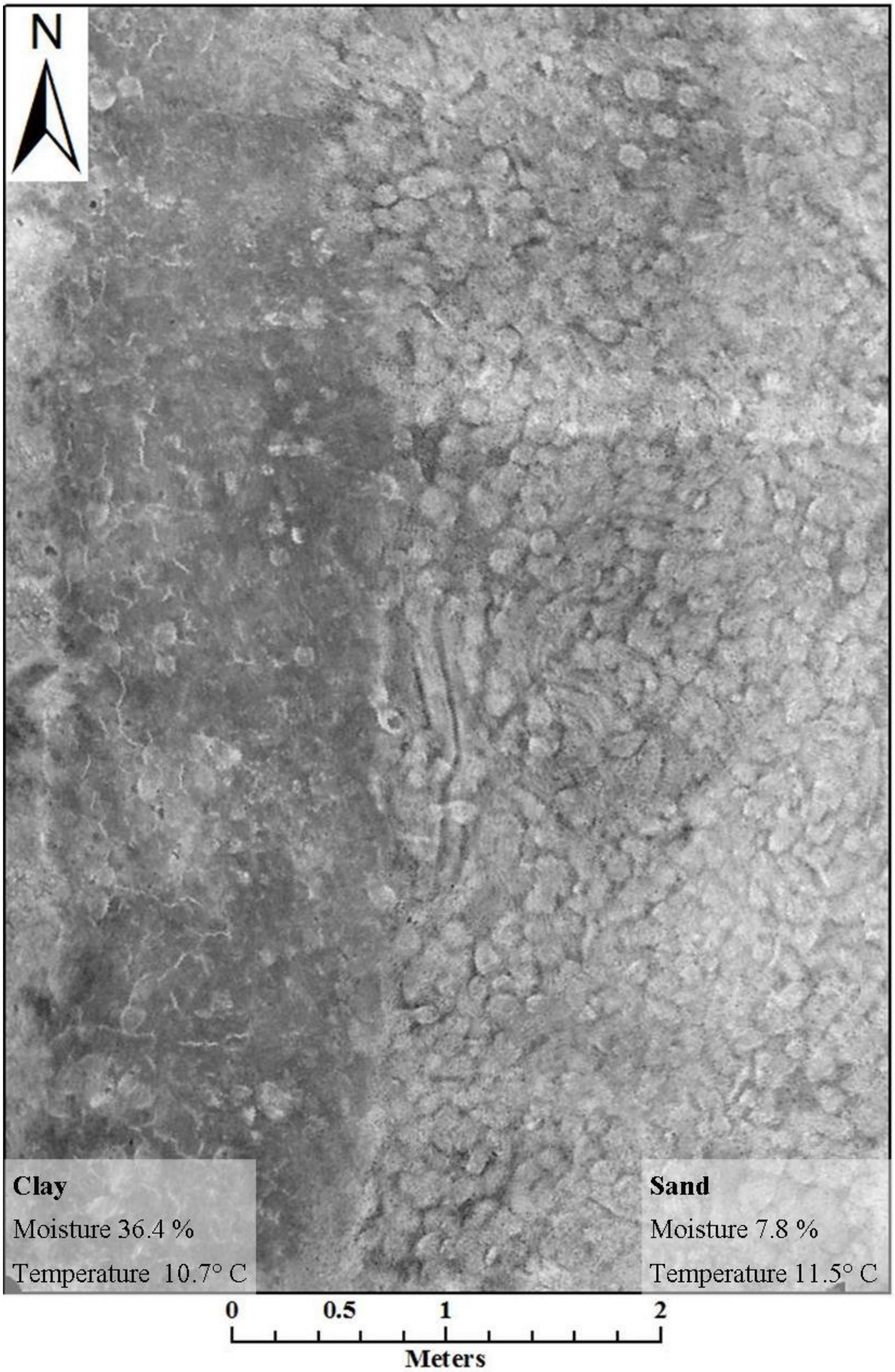

March 15 8:30 pm

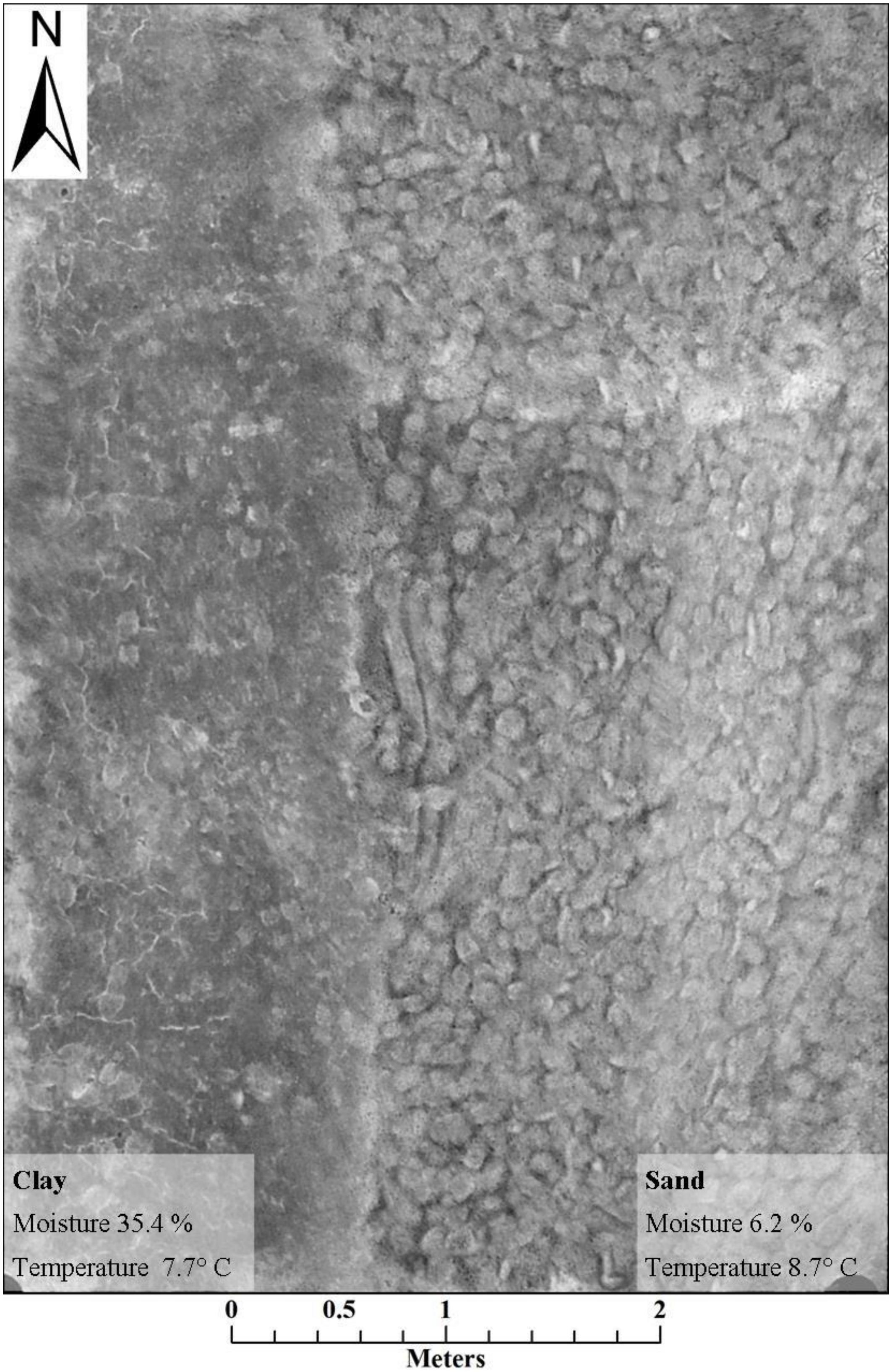

March 15 11:30 pm

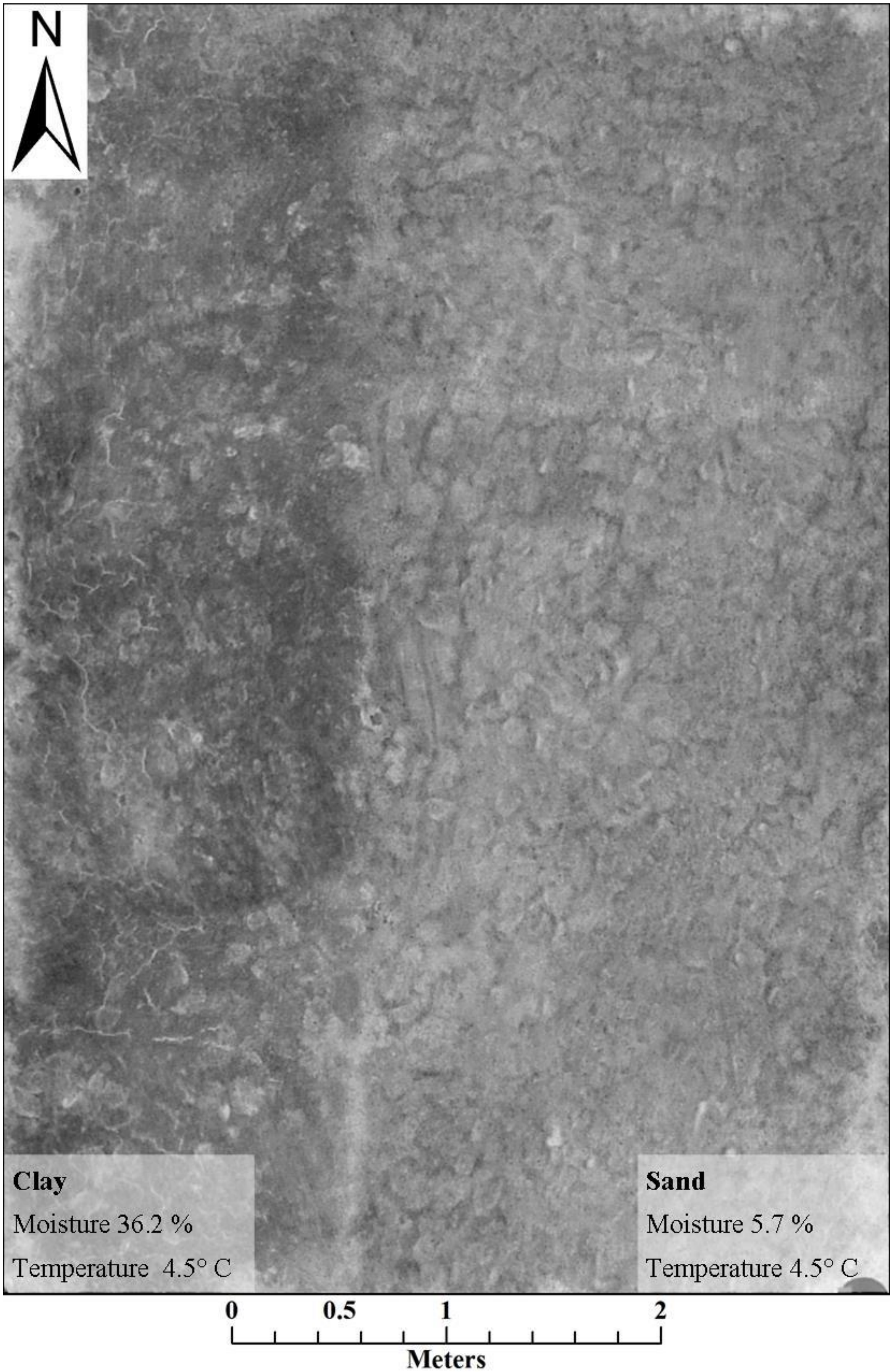

March 16 5:30 am

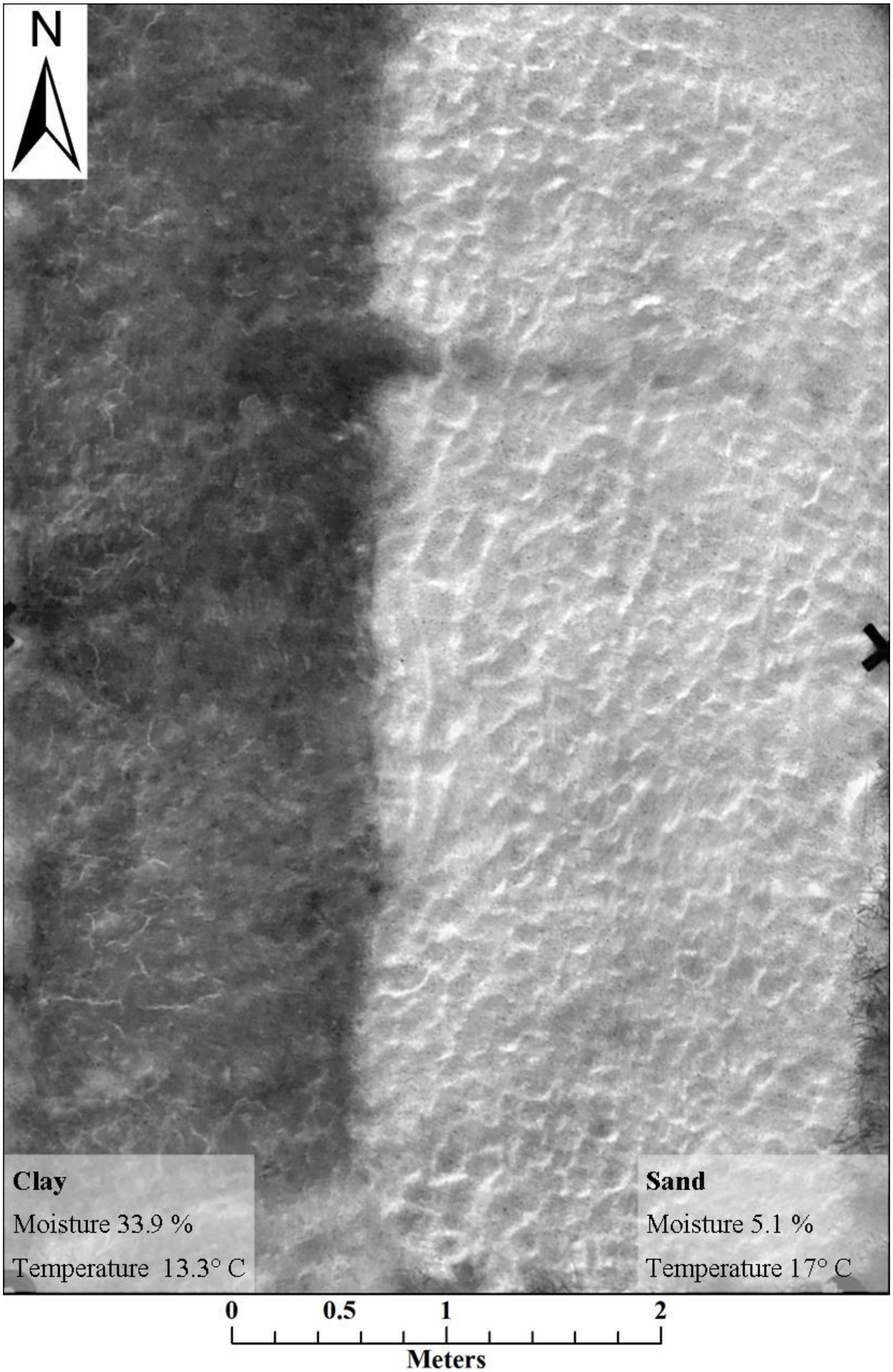

March 22 6:30 pm

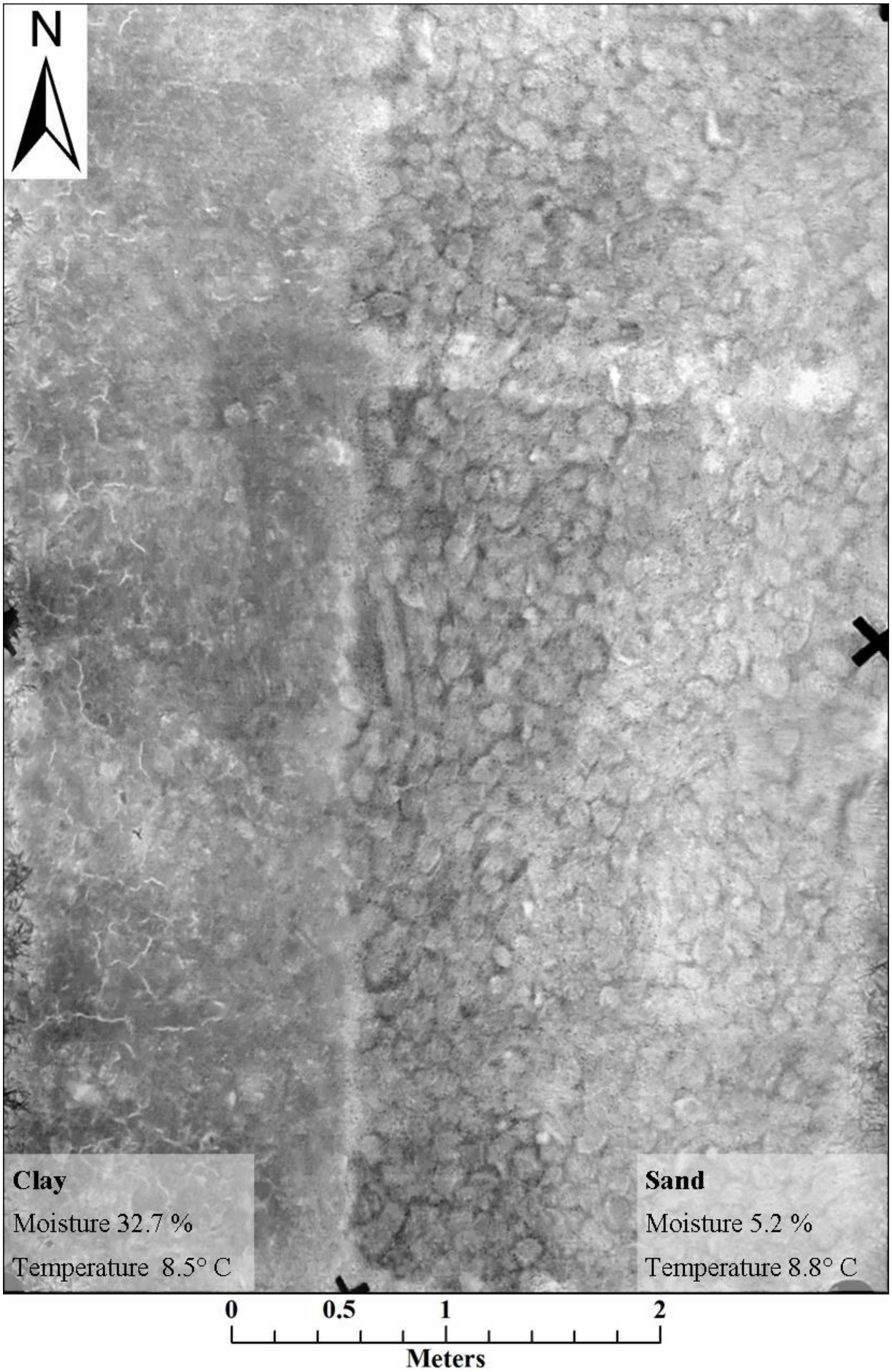

March 22 8:30 pm

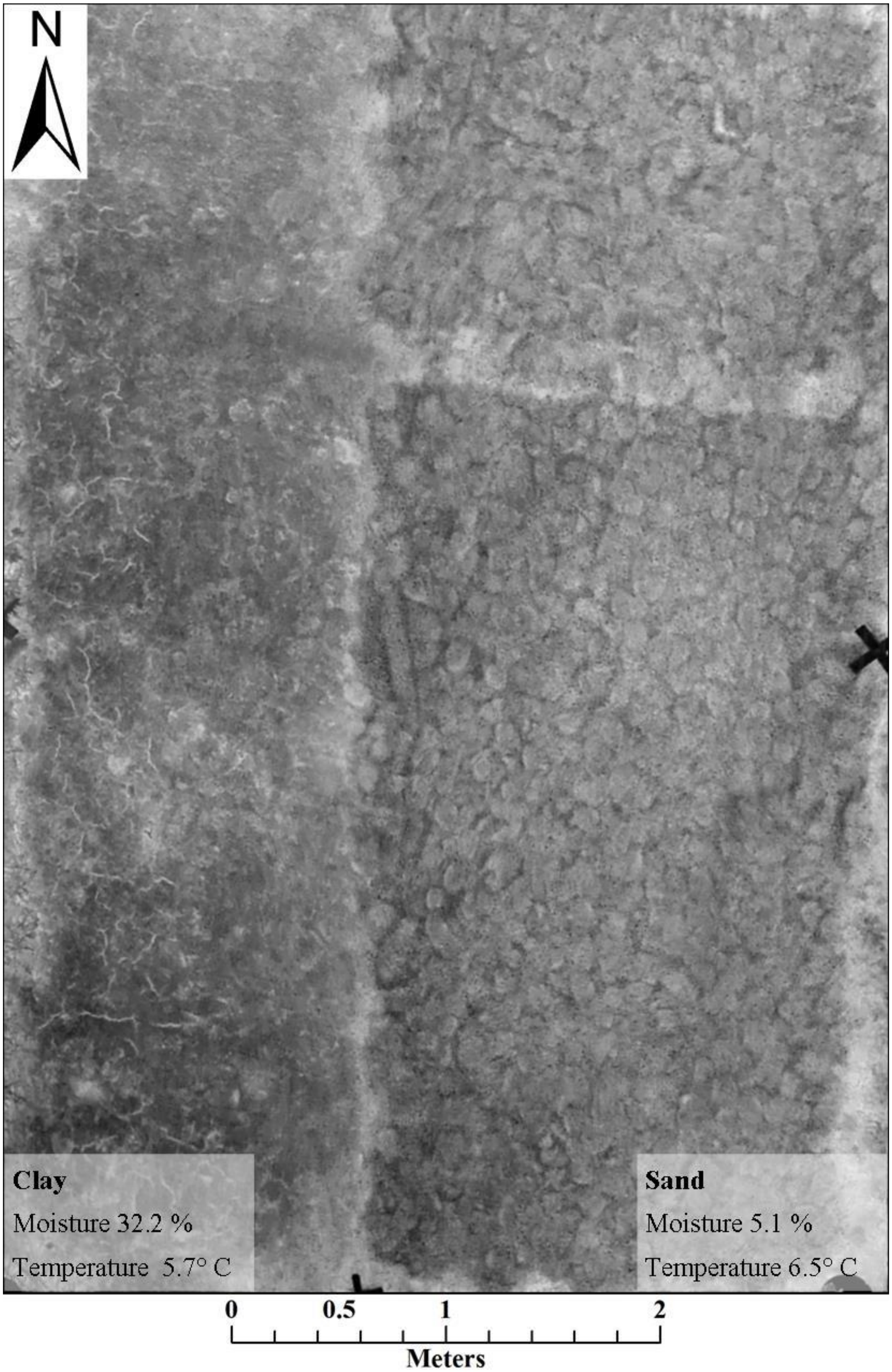

March 22 11:00 pm

March 23 12:30 am

March 23 2:30 am

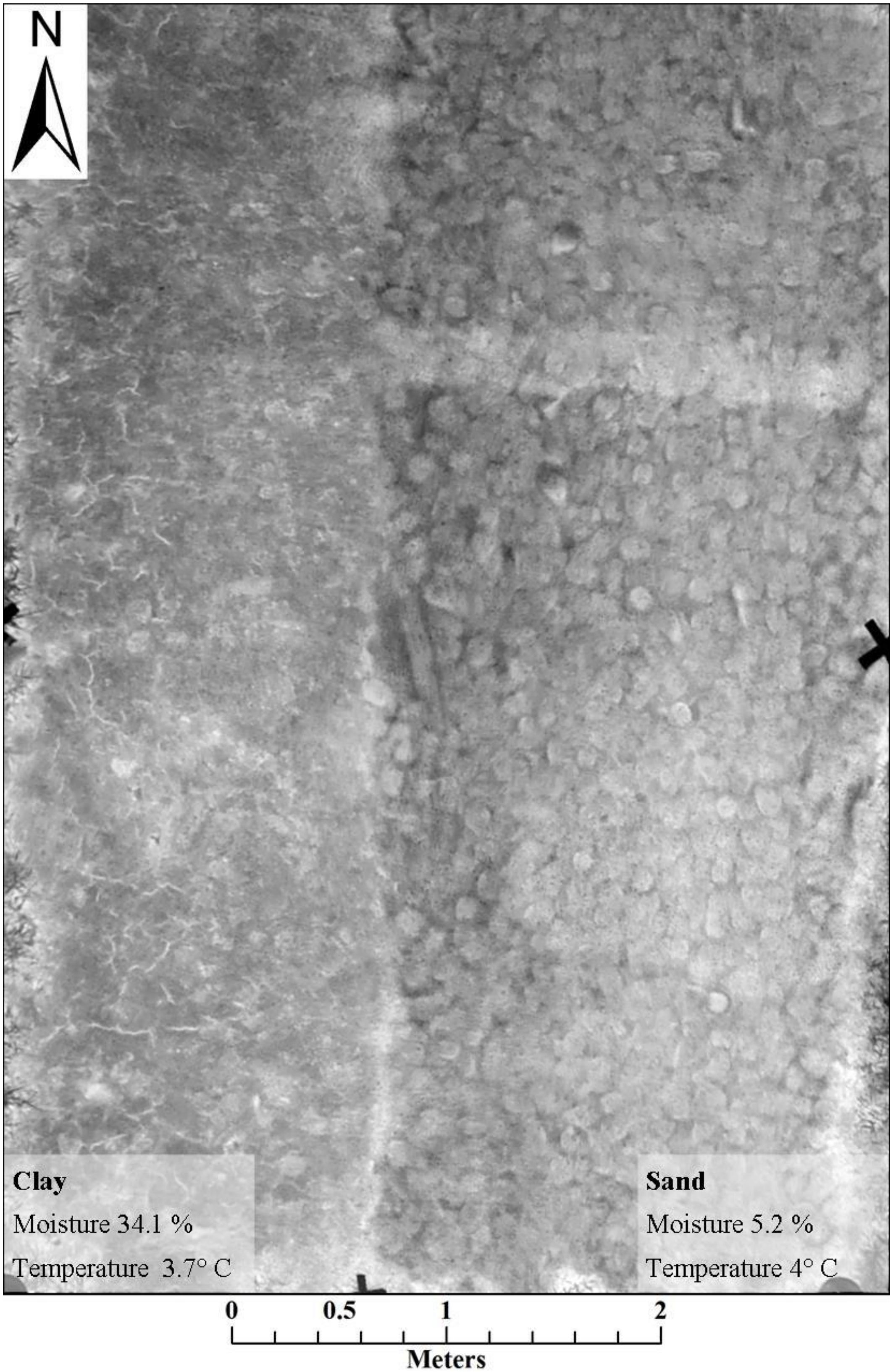

March 23 2:30 am

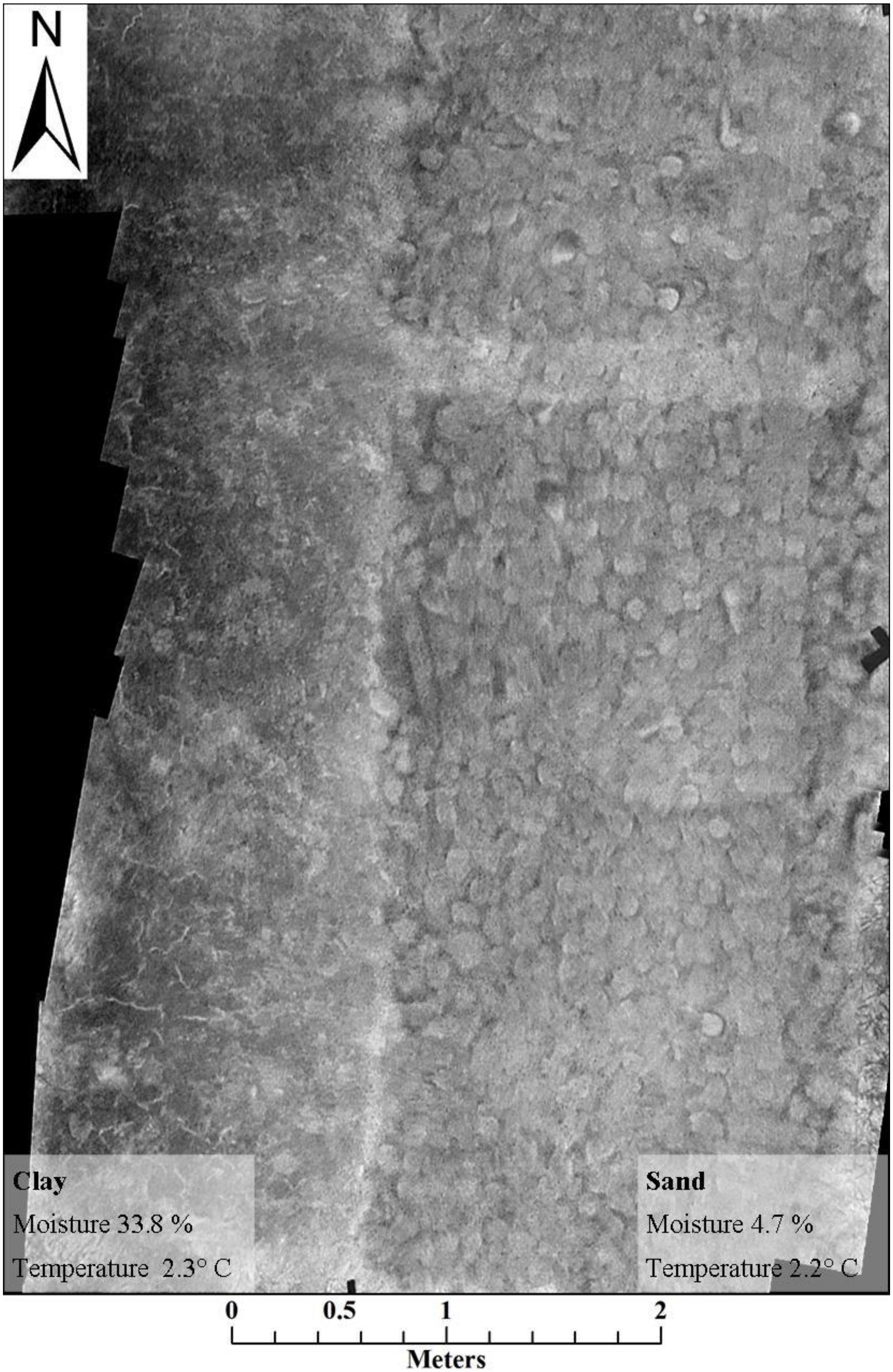

March 23 4:30 am

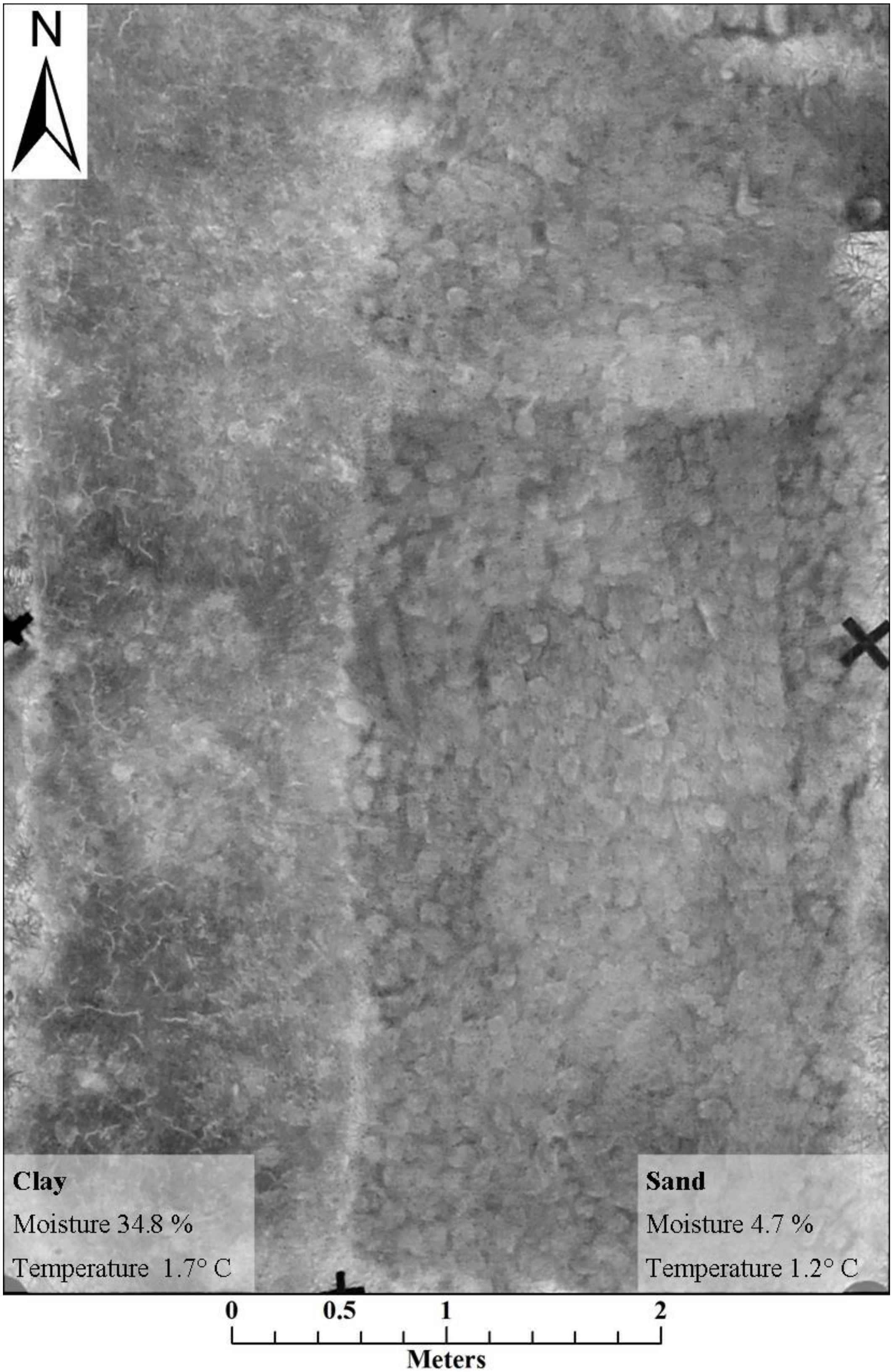

March 23 6:30 am

March 23 8:30 pm

March 23 10:30 pm

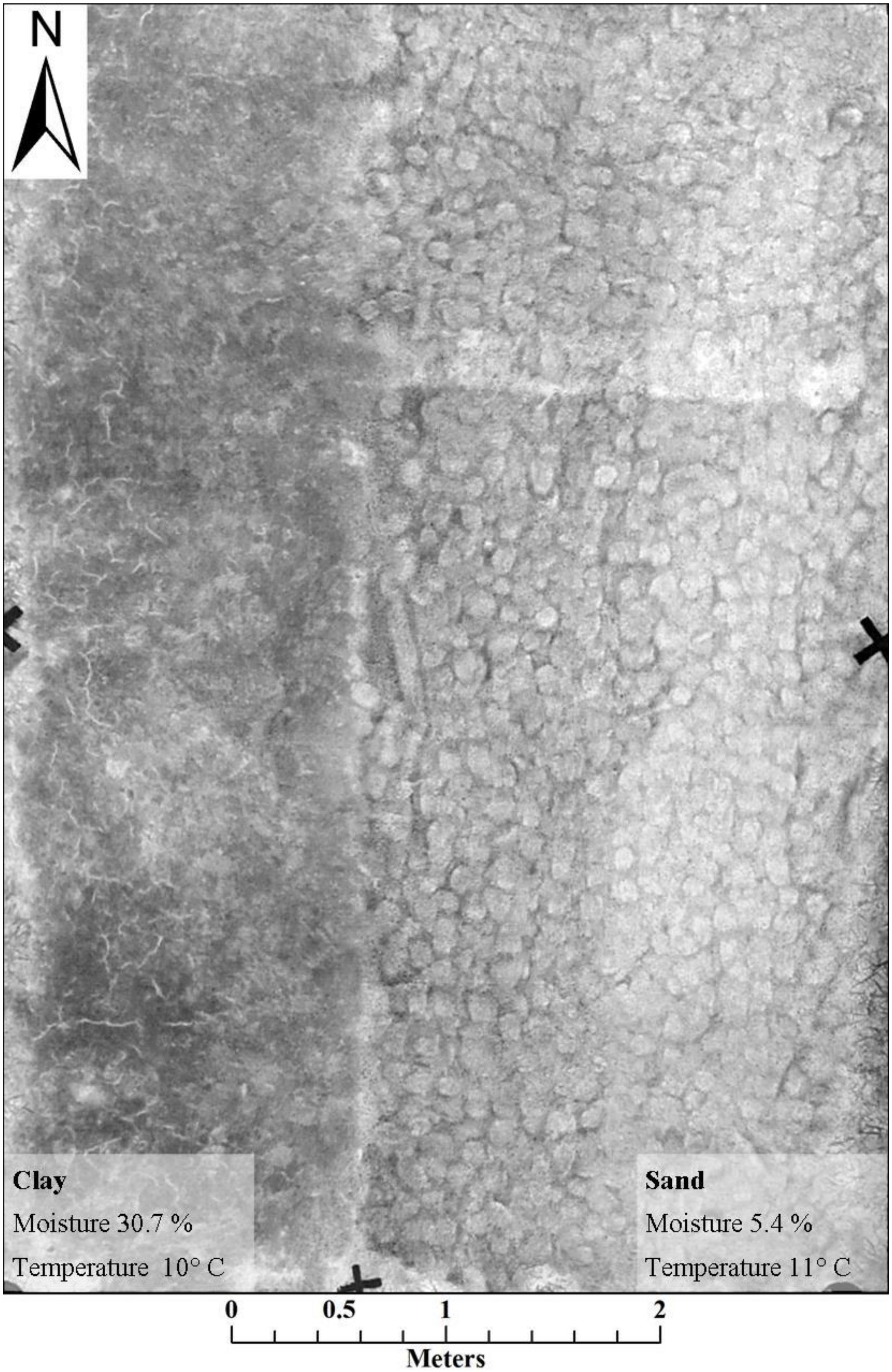

March 23 10:30 pm

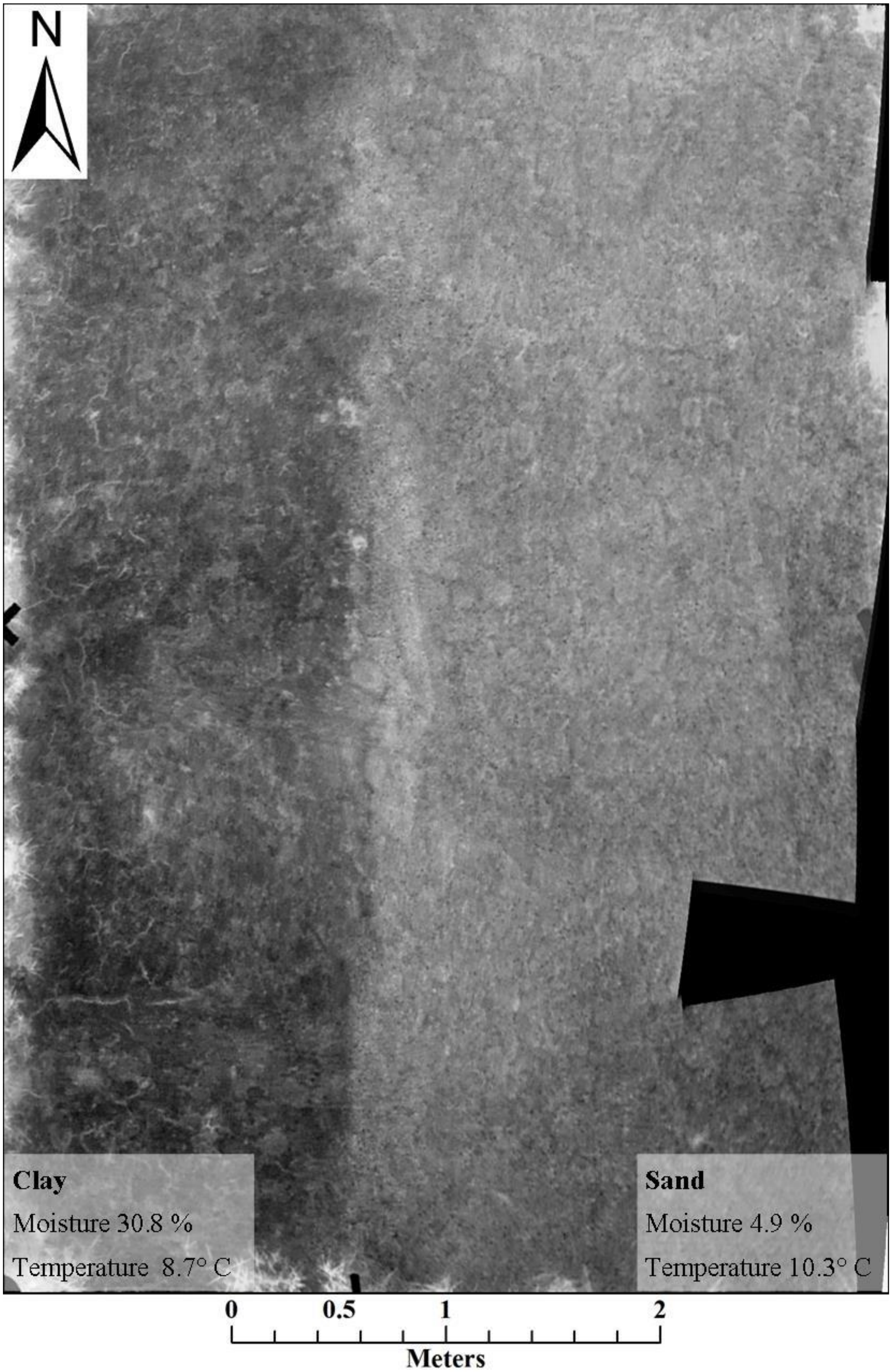

March 24 12:30 am

March 24 2:30 am

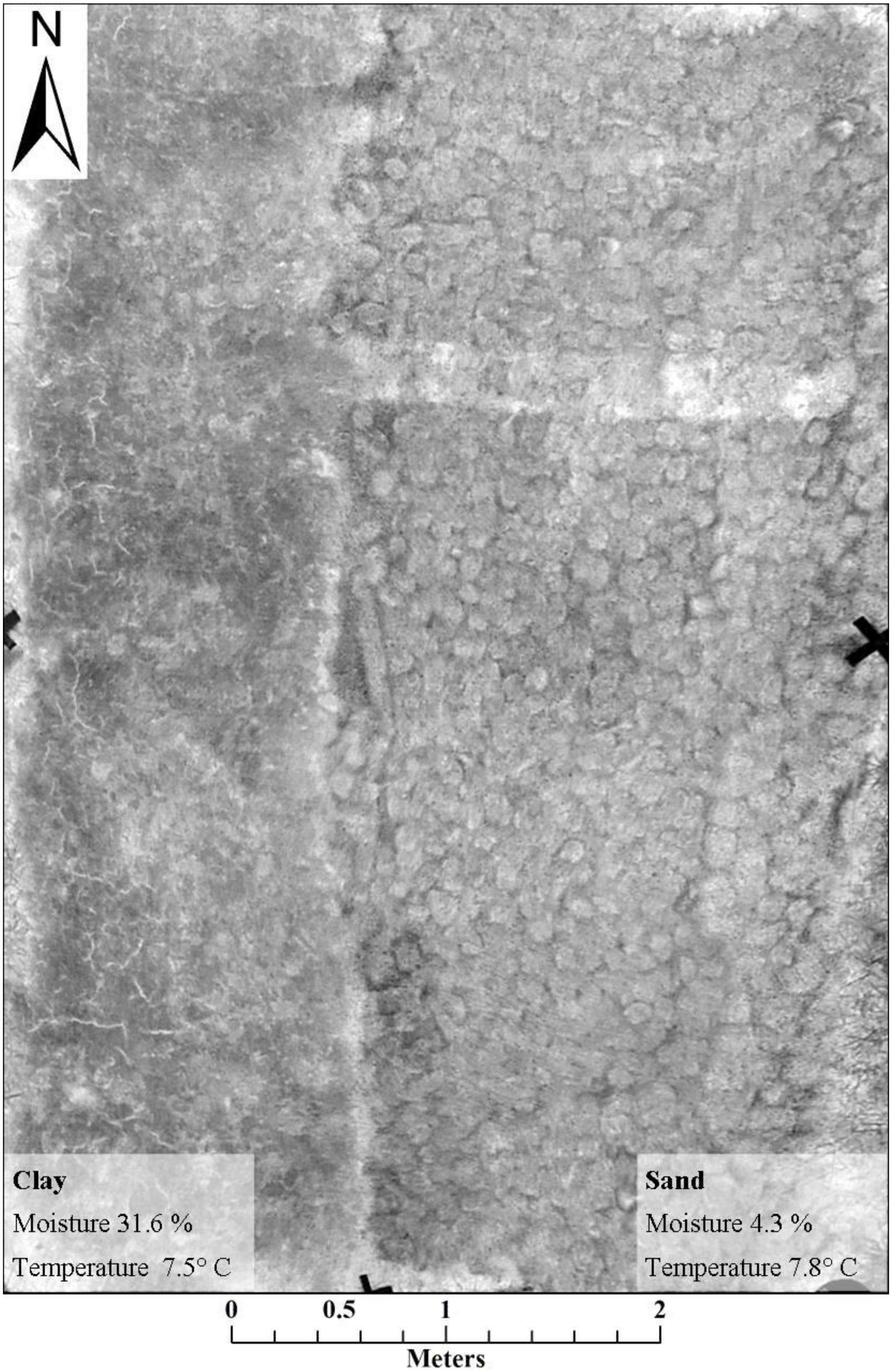

March 24 2:30 am

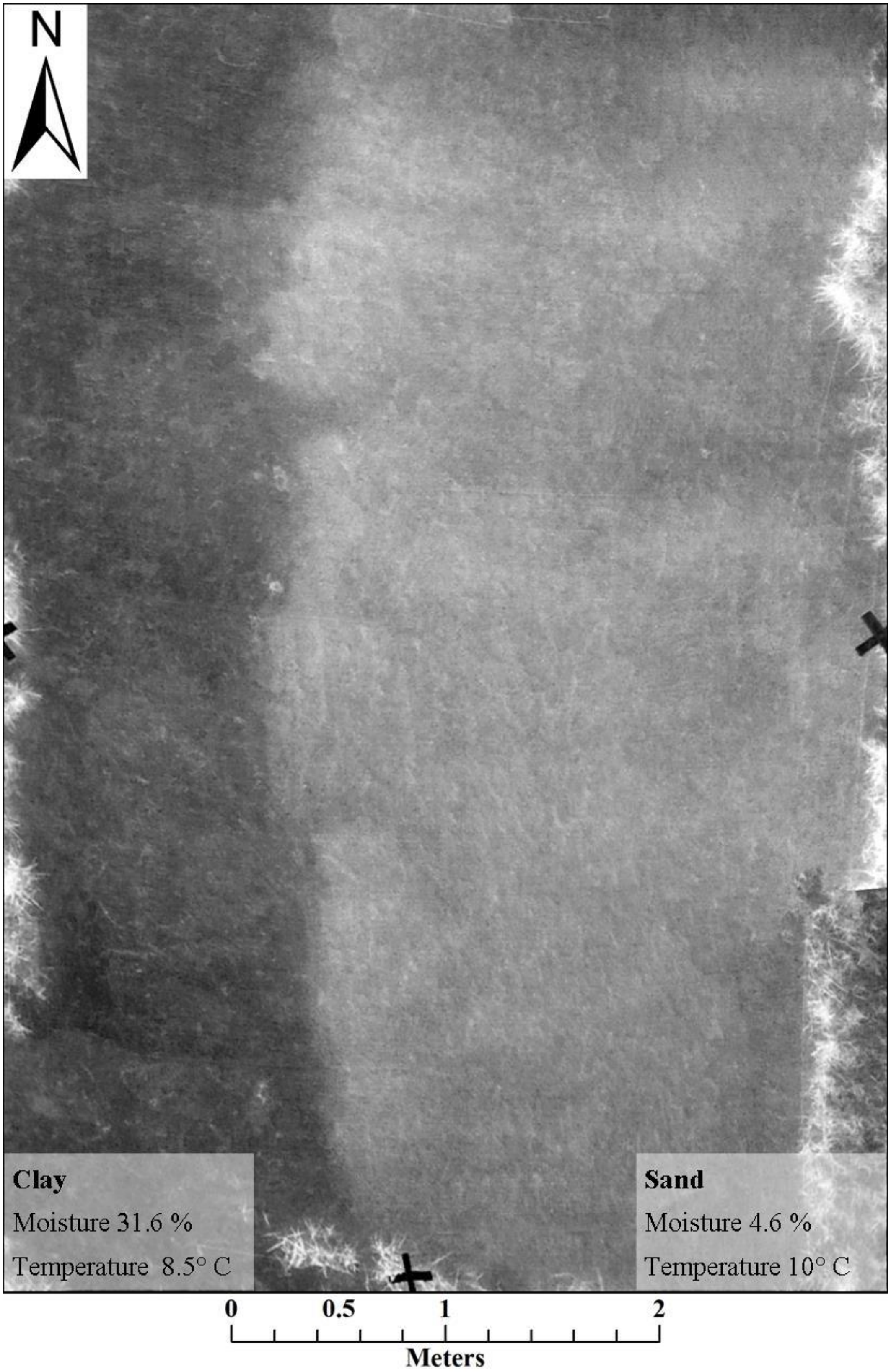

March 24 4:30 am

March 24 6:30 am

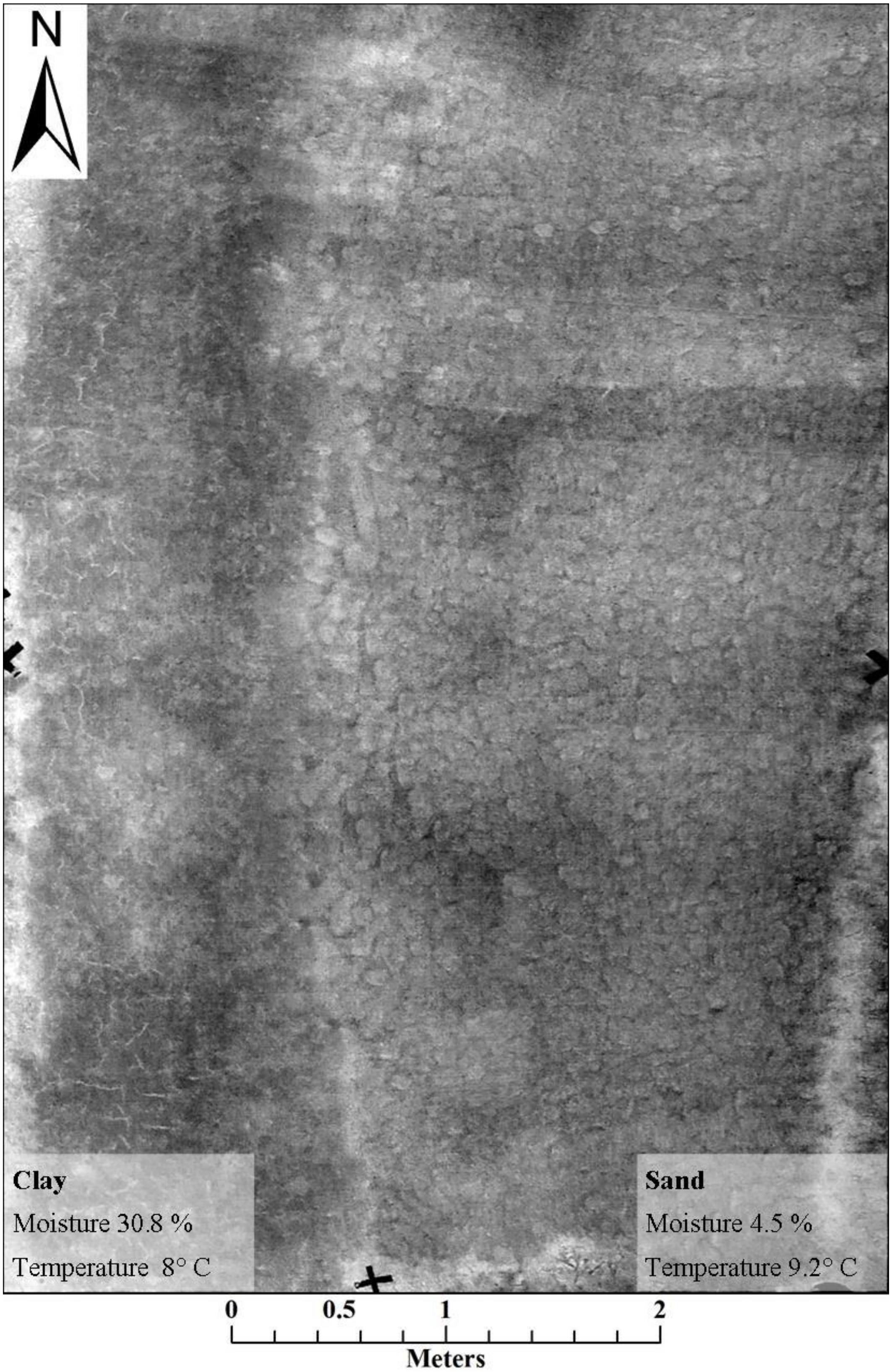

March 24 6:30 am